

Stress and strain amplification in non-Newtonian fluids filled with spherical and anisometric particles

DISSERTATION

for obtaining the academic degree

**DOKTORINGENIEUR
DOCTEUR EN SCIENCES POUR L'INGÉNIEUR**

submitted by

Dipl.-Ing. Jan Domurath

born 18 June 1985 in Rodewisch

at

Fakultät Maschinenwesen
Technische Universität Dresden

and

Institut de Recherche Dupuy de Lôme (IRDL)
Université de Bretagne-Sud

Date of defense: 18 December 2017

Committee members:

Gert Heinrich (*reviewer*)

Technische Universität Dresden and Leibniz-Institut für Polymerforschung Dresden e. V., Dresden, Germany

Gilles Ausias (*reviewer*)

Université de Bretagne-Sud, Lorient, France

Tim A. Osswald (*reviewer*)

University of Wisconsin-Madison, Madison, Wisconsin, USA

Marina Grenzer

Leibniz-Institut für Polymerforschung Dresden e. V., Dresden, Germany

Julien Férec

Université de Bretagne-Sud, Lorient, France

Niels Modler

Technische Universität Dresden, Dresden, Germany

Declaration of independent work

I declare that I have authored this thesis independently, that I have not used other than the declared sources / resources, and that I have explicitly marked all material which has been quoted either literally or by content from the used sources.

Dresden, 24 August 2017

Acknowledgments

I greatly wish to thank my supervisors, Marina Grenzer, Gert Heinrich, Gilles Aussias and Julien Férec for their encouragement, guidance, help and also freedom to pursue my own ideas during this work. I would also like to thank them for giving me the opportunity to prepare this work as cotutelle de thèse and thereby giving me the chance to live and work for some time in Lorient. A time that I greatly enjoyed.

I would also like to thank the other PhD students at IPF for making this time much more fun. Finally I would like to thank my family for their understanding, patience and support.

Abstract

A numerical study of dilute suspensions based on a non-Newtonian matrix fluid and rigid spheroidal particles is performed. A Carreau fluid describes the non-Newtonian matrix, as it captures the shear thinning behavior observed for many polymer melts.

After a literature review of suspensions containing rigid particles the special case of spherical particles is considered. Here, a uniaxial elongational flow of a Carreau fluid around a sphere is simulated and numerical homogenization is used to obtain the bulk viscosity of the dilute suspension for different applied rates of deformation and different thinning exponents. In the Newtonian regime the well-known Einstein result for the viscosity of a dilute suspension of rigid spherical particles is obtained. However in the transition region from Newtonian to non-Newtonian behavior, lower values of the intrinsic viscosity are obtained, which depend on both the applied rate of deformation and the thinning exponent. In the power law regime of the Carreau model, i.e. at high deformation rates, it is found that the intrinsic viscosity depends only on the thinning exponent. Utilizing the simulation results a modification of the Carreau model for dilute suspensions with a non-Newtonian matrix fluid is proposed.

In the last part of this thesis non-spherical particles are considered. If such particles, like rods or discs, are added to a liquid, the increase in the viscosity of the mixture is often described by the Lipscomb model. One important result of Lipscomb's model is the prediction of an increase in the viscosity of the suspension with increasing aspect ratio of the filler particles. Despite the fact that this model was originally proposed for a Newtonian matrix fluid it is also applied to polymer melts filled with non-spherical particles. Such an approach completely decouples the influence of the particle shape from the non-linear properties of the suspending fluid. Yet, since polymer melts often exhibit a strong non-Newtonian behavior, e.g. shear thinning, it is to be expected that such a superposition will give a wrong prediction of the suspension viscosity. To investigate the influence of the particle shape another numerical study is performed. In particular, different flows of a Carreau fluid around spheroidal particles with different orientations are simulated and numerical homogenization is used to obtain the intrinsic viscosity of the suspension as function of applied rate of deformation, thinning exponent and aspect ratio. From the results it is possible to extract the rheological coefficients of the Lipscomb model. In the Newtonian regime the simulation

results coincide with Lipscomb's predictions for the rheological coefficients. In the power law regime of the Carreau model, i.e. at high deformation rates, the rheological coefficients depend strongly on the thinning exponent. Furthermore, simulation results indicate that the rheological coefficients additionally depend on the particle orientation in the non-linear regime.

Résumé

Une étude numérique sur des suspensions diluées à base d'un fluide non newtonien et de particules sphéroïdales rigides est réalisée. Le comportement de la matrice non newtonienne est décrit par un fluide de type Carreau, car il capture le phénomène d'amincissement au cisaillement observé pour de nombreux polymères fondus.

Après une revue de la littérature sur les suspensions de particules rigides, le cas de particules sphériques est considéré. Ici, un écoulement en élongation uniaxiale d'un fluide de Carreau autour d'une sphère est simulée. Ensuite, l'homogénéisation numérique est utilisée pour déterminer la viscosité apparente de la suspension diluée pour différents taux de déformation et d'indices pseudoplastiques. Dans le domaine newtonien, le résultat d'Einstein donnant la viscosité d'une suspension diluée de particules sphériques et rigides est obtenu. Cependant, dans la zone de transition entre un comportement newtonien à parfaitement pseudoplastique, des valeurs plus faibles de la viscosité intrinsèque sont obtenues et dépendent à la fois du taux de déformation appliquée et de l'indice d'écoulement. Finalement, dans le régime en loi de puissance du modèle de Carreau, c'est-à-dire à des taux de déformation élevés, on constate que la viscosité intrinsèque dépend uniquement de l'indice pseudoplastique.

Dans la dernière partie de cette thèse, des particules non sphériques sont considérées. Si de telles particules, comme des bâtonnets ou des disques, sont ajoutées à un liquide, l'augmentation de la viscosité du mélange peut-être décrite par le modèle de Lipscomb. Un résultat important du modèle de Lipscomb est la prédiction d'une augmentation de la viscosité de la suspension avec l'accroissement du rapport de forme des particules. Malgré le fait que ce modèle a été initialement proposé pour un fluide newtonien, il est également applicable aux polymères fondus chargés de particules non sphériques. Une telle approche découple totalement l'influence de la forme des particules sur les propriétés non linéaires du fluide suspendant. Pourtant, étant donné que les polymères fondus présentent souvent un fort comportement non newtonien, par exemple rhéofluidifiant, on s'attend à ce qu'une telle superposition donne une mauvaise prédiction de la viscosité de la suspension. Ainsi, une autre étude numérique est effectuée pour investiguer l'influence de la forme des particules. En particulier, plusieurs écoulements d'un fluide de Carreau autour d'une particule sphéroïdale sont simulés pour différentes orientations. Une homogénéisation

numérique est ensuite utilisée pour obtenir la viscosité intrinsèque de la suspension en fonction du taux de déformation appliqué, de l'indice d'écoulement et du rapport de forme de la particule. A partir de ces résultats, il est possible d'exprimer les coefficients rhéologiques du modèle de Lipscomb. Dans le régime newtonien, les résultats de la simulation coïncident avec les prédictions de Lipscomb. Dans le domaine en loi de puissance du modèle de Carreau, c'est-à-dire à des taux de déformation élevés, les coefficients rhéologiques deviennent fortement dépendent de l'indice pseudoplastique. En outre, les résultats des simulations montrent que ces coefficients rhéologiques dépendent également de l'orientation des particules dans le régime non linéaire.

Zusammenfassung

Numerische Untersuchung zu verdünnten Suspensionen basierend auf einer nicht Newtonschen Matrixflüssigkeit und harten spheroidalen Partikeln wurde durchgeführt. Hierbei wurde ein Carreau Fluid verwendet, um die nicht Newtonschen Eigenschaften des Matrixfluids zu beschreiben. Das Carreau Model wurde gewählt, da es die häufig beobachtete Scherverdünnung von Polymerschmelzen gut beschreiben kann.

Nach einem Literaturüberblick zu Suspensionen mit harten Partikeln wird zunächst der Spezialfall von harten Kugeln betrachtet. Hierzu wird eine uniaxiale Dehnströmung eines Carreau Fluids um eine Kugel simuliert. Numerische Homogenisierung wird verwendet um die effektive Viskosität der Suspension für verschieden aufgebrachte Deformationsgeschwindigkeiten und Verdünnungsexponenten zu bestimmen. Im Newtonschen Bereich wird die bekannte Lösung Einsteins für die Viskosität einer verdünnten Suspension harter Kugeln erhalten. Im Übergangsbereich von Newtonschem zu nicht Newtonschem Verhalten werden kleinere Werte für die intrinsische Viskosität erhalten. Die intrinsische Viskosität hängt in diesem Bereich von der Deformationsgeschwindigkeit und dem Verdünnungsexponenten ab. Im power-law Bereich des Carreau Fluids, d.h. bei großen Deformationsgeschwindigkeiten, ist die intrinsische Viskosität einzig eine Funktion des Verdünnungsexponenten. Unter Nutzung der Simulationsergebnisse wird eine Modifikation des Carreau Modells vorgeschlagen.

Im letzten Teil dieser Arbeit werden nicht-sphärische Partikel betrachtet. Wenn solche Partikel, wie Stäbchen oder Scheiben, zu einer Flüssigkeit hinzugefügt werden wird die Änderung der Viskosität der Suspension häufig durch das Lipscomb Modell beschrieben. Eine wichtige Eigenschaft des Lipscomb Modells ist die Vorhersage eines Anstieges der Suspensionsviskosität mit steigendem Aspektverhältnis der Partikel. Obwohl das Modell ursprünglich für Newtonsche Flüssigkeiten vorgeschlagen wurde, wird es häufig auch bei, mit nicht-sphärischen Partikeln gefüllten, Polymerschmelzen angewendet. Solch ein Ansatz entkoppelt jedoch vollkommen den Einfluss der Partikelform von den nichtlinearen Eigenschaften der Polymerschmelze. Da Polymerschmelzen häufig stark nichtlineares Verhalten zeigen, z.B. Scherverdünnung, ist zu erwarten dass solch eine einfache Superposition zu einer falschen Vorhersage der Suspensionsviskosität führen wird. Um den Einfluss der Partikelform auf die nichtlinearen Eigenschaften zu untersuchen

werden wieder numerische Simulationen verwendet. Dabei werden verschiedene Strömungen eines Carreau Fluids um spheroidale Partikel mit unterschiedlichen Orientierung simuliert und numerische Homogenisierung wird verwendet um die intrinsische Viskosität als Funktion der aufgebrachten Deformationsgeschwindigkeit, des Verdünnungsexponenten und des Partikelspektverhältnisses zu bestimmen. Es ist möglich die rheologischen Parameter des Lipscomb Modells aus den Simulationsergebnissen zu bestimmen. Im Newtonschen Bereich stimmen die numerisch bestimmten Werte mit der Vorhersage Lipscomb's überein. Im power-law Bereich des Carreau Fluids, d.h. bei großen Deformationsgeschwindigkeiten, hängen die rheologischen Parameter stark vom Verdünnungsexponenten ab. Weiter kann man aus den Ergebnissen auf eine zusätzliche Abhängigkeit der rheologischen Parameter von der Partikelorientierung schließen.

Contents

Abstract	VII
Résumé	IX
Zusammenfassung	XI
1. Motivation	1
2. An overview of the rheology of suspensions	5
2.1. Rigid spherical particles	5
2.1.1. Newtonian matrix fluids	5
2.1.2. Non-Newtonian matrix fluids	9
2.1.3. Superposition of viscosity-stress curves	14
2.2. Rigid non-spherical particles	18
2.2.1. Newtonian matrix fluids	18
2.2.2. Non-Newtonian matrix fluids	25
2.3. Summary	27
2.A. Viscosity as function of stress	28
3. Computational fluid dynamics simulations of suspensions	31
3.1. Introduction	31
3.2. Computational domain and mesh generation	34
3.3. Fixed particle in elongational flows	35
3.3.1. Problem description	35
3.3.2. Boundary conditions for a fixed particle	38
3.4. Moving particle in a shear flow	39
3.4.1. Problem description	39
3.4.2. Boundary conditions for a moving particle	42
3.5. Computation of effective macroscopic properties	43
3.5.1. Introduction	43
3.5.2. Computing the intrinsic viscosity	44
3.6. Summary	47
4. Spherical particles	51
4.1. Introduction	51
4.2. Simulation results	53

Contents

4.3. Taylor expansion	55
4.4. Fitting intrinsic viscosity	58
4.5. Discussion of strain amplification	61
4.6. Extension to higher volume fractions	63
4.7. Summary	65
5. Spheroidal particles	67
5.1. Introduction	67
5.2. Simulation Results	72
5.3. Ad hoc model for the rheological coefficients	82
5.4. Re-evaluating spherical particles	86
5.5. Summary	88
6. Conclusions	89
A. Notation	91
Bibliography	95
List of Symbols	105
List of Figures	109
List of Tables	111

1. Motivation

More than 100 years ago Albert Einstein computed in his dissertation [1] the change in viscosity of a dilute suspension of rigid spherical particles, the result was later corrected in [2]. Since Einstein's calculations many authors extended his work to higher volume fractions of spherical particles [3–9] and to rigid non-spherical particles [10–14]. Einstein's equation itself has been computed by many authors in different ways [15–18] and still today it attracts the interest of mathematicians [19, 20].

One main assumption in the calculation of Einstein and the later works is that the fluid is Newtonian, that is its viscosity is constant. If one looks at common polymer melts, as used in the production of consumer goods, it turns out that these polymer melts are non-Newtonian in their behavior, their viscosity is not constant. For many polymer melts it is commonly observed that the shear viscosity decreases with increasing rate of deformation. Accounting for this nonlinearity in the properties of polymer melts is an interesting topic with direct application in the polymer industry, since polymer melts are often filled with particles to change their properties. The reasons for filling polymer melts with rigid particles are multifold. One of the most common reasons is the improvement of mechanical properties of the end product, for example its stiffness by adding rigid particles. Others are: flammability (clay) and electric conductivity (carbon black, carbon nanotubes). For example it is possible to sense strain by adding carbon nanotubes to polymers, as the conductivity changes with the deformation of the part [21, 22]. A change in conductivity under deformations can also be observed in rubbers filled with carbon black [23]. This enables for the production of “smart parts”: one could imagine a part that tells its user it is under a too high load. It is also possible add magnetic particles to a polymer matrix. Upon addition of magnetic particles to a rubber one can alter the stiffness of the composite by applying a magnetic field [24–26].

By adding particles to the polymer to change the properties of the end product one inevitably changes the properties of the polymer melt to be processed. This means in general an increase in the viscosity of the melt/mixture. The increase in viscosity results in a need to change the machine parameters for processing, e.g. higher pressure in injection molding. Thus if one aims to decrease the flammability, by adding clay to the polymer, one also has to think about how this

1. Motivation

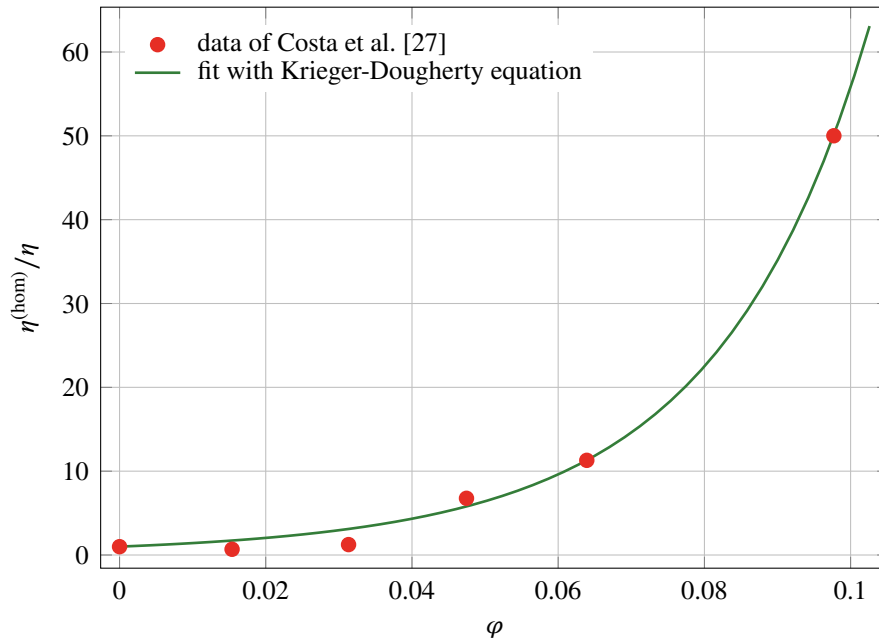


Figure 1.1.: Relative change in viscosity for a LDPE (low-density polyethylene) melt filled with nano clay versus volume fraction of nano clay, data taken from Costa et al. [27]. Solid line: fit with Krieger-Dougherty equation (2.14) with $[\eta] = 34.65$ and $\varphi_{\max} = 0.38$. ($\eta^{(\text{hom})}$ is the viscosity of the filled melt, η the viscosity of the unfilled polymer melt.)

will influence the processability of the polymer melt. For example, in Costa et al. [27] a nano clay has been added to a LDPE (low-density polyethylene) melt to alter its flammability. Figure 1.1 shows the relative change in the viscosity of the composite as a function of the volume fraction of clay. In the figure a drastic increase of the viscosity can be observed. For this reason it is helpful to be able to estimate the change in the viscosity by knowing the properties of the polymer and the amount and shape of the particles to be added.

Figure 1.2 shows the shear viscosity η for different polymers at temperatures commonly used in processing as a function of shear rate $\dot{\gamma}$. Also indicated in figure 1.2 are ranges of shear rates for different processing procedures. For injection molding the shear rate range is from 10^3 s^{-1} to 10^4 s^{-1} and one can clearly see that in this range all the polymers are in the non-linear regime of deformation¹. But also for the other manufacturing processes in figure 1.2 most polymers behave non-linear. Thus it is very important to know how the non-linear behavior of the polymer melt is influenced by the addition of filler particles. While the problem of Newtonian fluids filled with rigid particles has been extensively studied, there are still many open questions for non-Newtonian fluids filled with rigid particles, even in the dilute case. One can find experimental works [29–31]

¹In the linear regime the curve would be horizontal.

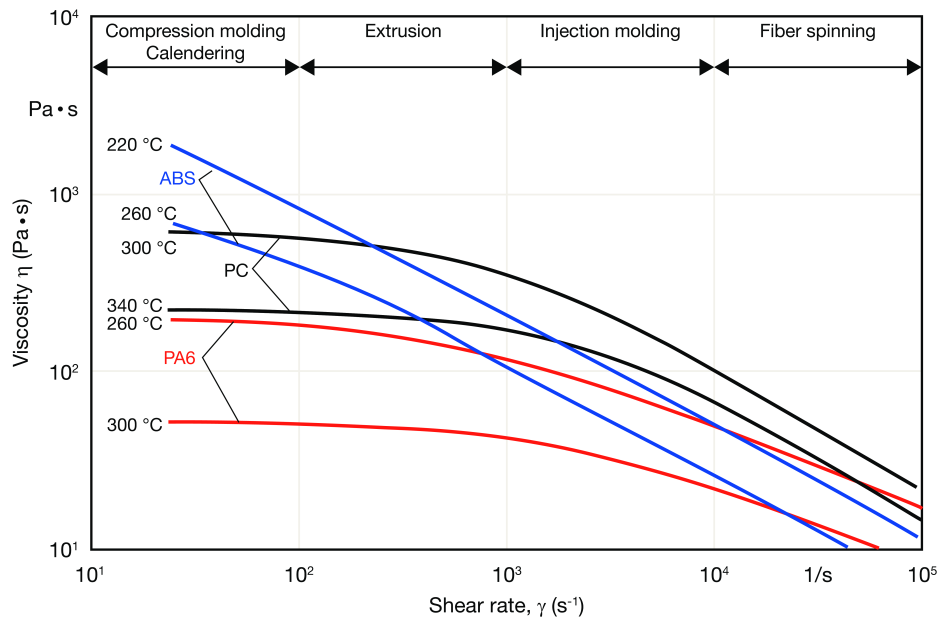


Figure 1.2.: Flow curves for different polymers at different temperatures. Also indicated are the shear rate ranges for common processing procedures. The polymer are: ABS (Acrylonitrile butadiene styrene), PC (Polycarbonate) and PA6 (Polyamide 6). (From Osswald and Rudolph [28], reprinted with permission from Carl Hanser Verlag GmbH & Co. KG)

on how the viscosity of a non-Newtonian fluid changes upon addition of filler particles and also theoretical works [32–37] can be found where attempts were made to predict the behavior of filled polymers. Due to the non-linear nature of the problem these theoretical works are based on assumptions which make the problem manageable by analytical methods.

Numerical works studying viscoelastic polymer-solid mixtures can also be found in the literature, but these are often devoted to the motion of particles in viscoelastic fluids rather than their bulk properties [38–41]. Only in a few papers [42–44] the authors also computed bulk properties, such as the storage modulus. Further, some review articles exist on the topic of filled polymers [45–48] where also non-linear behavior is discussed.

Nevertheless, in none of the aforementioned numerical works do the authors systematically investigate the influence of the matrix nonlinearity on the bulk properties. The aim of the present PhD studies is to investigate exactly this question. For that purpose computational fluid dynamics (CFD) simulations are done using a non-linear viscosity model for the polymer matrix and the bulk properties of the suspension are computed for a broad range of shear rates. With the simulation the linear, non-linear and crossover region between linear and non-linear behavior is investigated.

1. Motivation

The linear results are compared with the existing analytical solutions.

In Laven and Stein [33], Chateau et al. [34] and Tanner et al. [35] the influence of rigid spherical particles on the viscosity in the power law regime of polymer melts is investigated, that is at very high shear rates. One can see in Figure 1.2 that the polymers PC (Polycarbonate) and PA6 (Polyamide 6) are in the crossover regime from linear to power law behavior at shear rates that commonly occur in extrusion and injection molding. It is thus important to know how the crossover between linear and power law regimes is altered upon the addition of filler particles. One aim of this thesis is to improve those works and investigate how the addition of rigid spherical particles influences this crossover. As this problem is highly non-linear, numerical methods are used to compute the viscosity change in a filled polymer melt.

In the case of non spherical particles, such as clays and carbon nanotubes, analytical solutions are also only known for Newtonian matrix fluids. For spheroidal particles in a Newtonian fluid the bulk behavior can be described by the transversely isotropic fluid equation (TIF), which has three parameters that depend on the particle aspect ratio. It is commonly assumed that the parameters of the TIF equation do not change if the matrix fluid becomes non-Newtonian [49, 50]. This assumption seems to be brute force. It is already known that the TIF parameters change for spherical particles (a special case of the TIF equation) in a non-Newtonian fluid. It thus stands to reason that the parameters in the TIF equation will also change for non-spherical particles in a non-Newtonian fluid. This question is also investigated within this thesis. As the problem is again highly non-linear the problem will be solved by means of CFD simulations.

The thesis structure is as follows. Chapter 2 will give a review of results found in literature on suspensions of rigid particles and chapter 3 will explain the numerical methods used in the CFD simulations. In chapter 4 the influence of rigid spherical particles on the bulk properties of a filled polymer melt is investigated and a model is proposed to capture the effect of the presence of rigid spherical particles in a non-Newtonian fluid. Predictions of this model are compared with experimental data. Further in chapter 5 dilute suspension of anisometric particles is investigated and non-linear parameters for the transversely isotropic fluid equation [14] are computed. The thesis is closed by a short summary and outlook for future studies.

2. An overview of the rheology of suspensions

In everyday life one can find dispersions of solid particles in liquids everywhere. Blood, wheat beer and mortar are just some common examples.

Since suspensions can be found all around us, there is a lot of interest not only to understand their behavior from the microstructure, but also to be able to describe their macroscopic behavior by proper continuum models. This is of big importance for example for process simulations, like the simulation of the injection molding process of polymer parts.

In this chapter a review of results found in literature is given for spherical and non-spherical particles.

2.1. Rigid spherical particles

2.1.1. Newtonian matrix fluids

The increase in the viscosity of a homogeneous suspension of a small amount of rigid spherical particles in a Newtonian fluid was first computed by Einstein [1, 2] and is given by

$$\eta^{(\text{hom})} = \eta(1 + 2.5\varphi). \quad (2.1)$$

In the above relation $\eta^{(\text{hom})}$ and η are respectively the viscosity of the homogenous suspension and that of the suspending or matrix fluid and φ is the volume fraction of particles. Einstein's equation (2.1) is only valid for very small volume fractions of particles, that is $\varphi \lesssim 0.03$ [51]. It is customary to introduce additional relations between the viscosity of the suspension and that of the matrix fluid [52]. The first relation is the so called relative viscosity η_r , which is defined as

$$\eta_r = X = \frac{\eta^{(\text{hom})}}{\eta}. \quad (2.2)$$

2. An overview of the rheology of suspensions

The symbol X is also often used, especially in the rubber community [53] for the amplification of the shear modulus of filled rubbers, and is referred to as *hydrodynamic amplification factor*. This double usage is possible due to a mathematical analogy of the problems: filled linear elastic solid and filled Newtonian fluid [5, 54].

The specific viscosity is given as

$$\eta_{\text{sp}} = \frac{\eta^{(\text{hom})} - \eta}{\eta}. \quad (2.3)$$

The ratio of the specific viscosity to the volume fraction in the *dilute limit* is called the *intrinsic viscosity*:

$$[\eta] = \lim_{\varphi \rightarrow 0} \frac{\eta_{\text{sp}}}{\varphi}. \quad (2.4)$$

In the case of Einstein's equation (2.1) the intrinsic viscosity takes the value of 2.5. For non-spherical or non-rigid particles this value can differ significantly [52]. Hence we may write instead of (2.1)

$$\eta^{(\text{hom})} = \eta(1 + [\eta]\varphi). \quad (2.5)$$

In the computation that lead to the seminal result given in (2.1), Einstein considered the additional amount of work per unit time needed to deform a fluid that contains one rigid spherical particle compared to the same fluid without a particle. This consideration implies that there are no interactions between particles which is unavoidable for higher volume fractions. Batchelor and Green [5] accounted for two particle interactions and obtained for the viscosity of a suspension in an elongational flow

$$\eta^{(\text{hom})} = \eta(1 + 2.5\varphi + 7.6\varphi^2). \quad (2.6)$$

For a shear flow, where the particles are subjected to Brownian motion, Batchelor [6] obtained

$$\eta^{(\text{hom})} = \eta(1 + 2.5\varphi + 6.2\varphi^2), \quad (2.7)$$

where $\varphi \lesssim 0.1$ [51]. From equations (2.6) and (2.7) one can see that there is a difference in the quadratic term in the volume fraction. This difference can be attributed to the fact that in the calculations leading to (2.6) Brownian motion was neglected, but not for (2.7). In the presence of relatively strong Brownian motion the spatial distribution is uniform, while in the absence of Brownian forces some configurations are more common than others [6]. Another example on how the spatial configuration of particles influences the quadratic term is that of fixed particles. Such a case can be realized by embedding particles in an elastic matrix subjected to infinitesimal

2. An overview of the rheology of suspensions

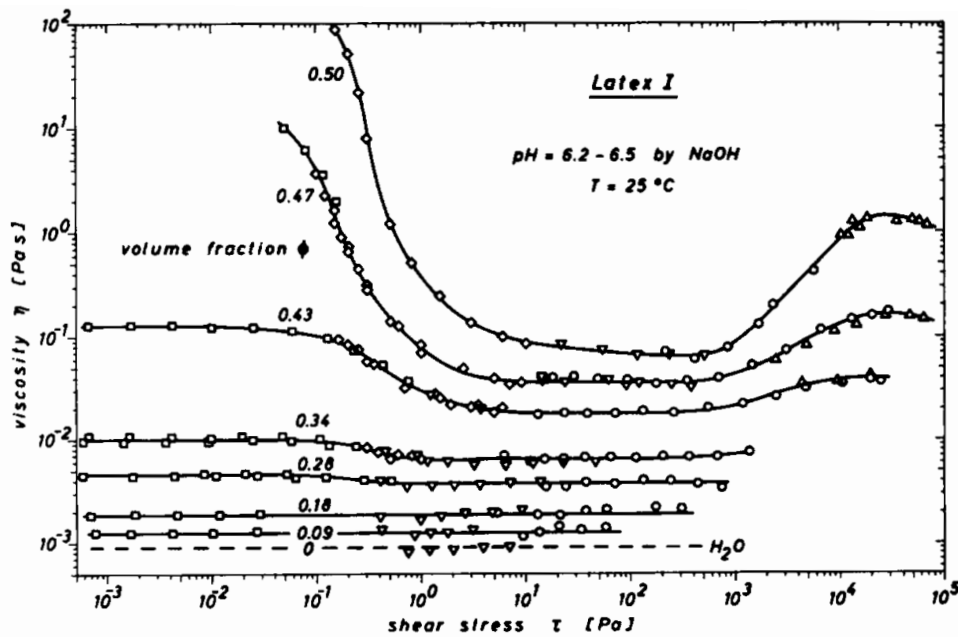


Figure 2.1.: Viscosity vs. shear stress for a suspension of polymer spheres with diameter $d = 250$ nm in water, from Laun [56]. Until a particle volume fraction of $\varphi = 0.28$ the suspension stays Newtonian. (Copyright Wiley-VCH Verlag GmbH & Co. KGaA. Reproduced with permission.)

strains. In this case the prefactor to the quadratic term is 5.0 [5, 55]. From (2.6) and (2.7) one can also deduce that Brownian motion does not change the dilute result of Einstein, as was shown in [6]. Happel and Brenner [17] found that there is almost no influence of the type of bulk flow on Einstein's result.

In the aforementioned relations the effective material behavior does not change: a Newtonian fluid stays a Newtonian fluid upon addition of particles. For high volume fractions of particles this is not generally true. Figure 2.1 shows measured viscosity-shear stress curves from Laun [56] for a suspension of polymer spheres with diameter $d = 250$ nm in water for different volume fractions of particles. The behavior of the suspension stays Newtonian until the volume fraction of $\varphi = 0.28$. For the volume fraction $\varphi = 0.43$ a pronounced shear thinning can be observed. At high shear rates and high particle concentrations an additional shear thickening is observed.

As shown in figure 2.1 at intermediate concentrations of filler particles one observes shear thinning behavior. This effect can be attributed to the increasing hydrodynamic forces acting on the particles [51]. The interplay between Brownian and hydrodynamic forces is generally captured in the so called *Peclet number* Pe . The Peclet number can be defined as ratio of the time τ_d a particle needs to diffuse by its own radius to the time τ_s , it takes for a particle to be dragged

2. An overview of the rheology of suspensions

by the flow about its radius,

$$\text{Pe} = \frac{\tau_d}{\tau_s}. \quad (2.8)$$

The diffusion coefficient D of a spherical particle in a Newtonian liquid is given in the dilute limit by the Stokes-Einstein equation

$$D = \frac{k_B T}{6\pi\eta r}, \quad (2.9)$$

where k_B is Boltzmann's constant, T is the absolute temperature and r is the particle radius. The viscosity of the suspending fluid is η . With the diffusion coefficient one can express the time needed for a particle to diffuse about its radius as

$$\tau_d \approx \frac{r^2}{D}. \quad (2.10)$$

The time by which a particle was dragged about its radius is given by

$$\tau_s = \frac{r}{U} = \frac{1}{\dot{\gamma}} \quad (2.11)$$

with U the fluid velocity and $\dot{\gamma}$ the shear rate. Inserting (2.10) and (2.11) into (2.8) one obtains the usual definition of the Peclet number [51, 57]

$$\text{Pe} = \frac{6\pi\eta r^3}{k_B T} \dot{\gamma}. \quad (2.12)$$

A descriptive interpretation of the Peclet number can be given by rearranging (2.8) to

$$\tau_d = \text{Pe} \tau_s. \quad (2.13)$$

The above relation can be interpreted as follows: by the time a particle has diffused once its radius it has traveled Pe times its radius due to the action of hydrodynamic forces. Hence, if $\text{Pe} \gg 1$ it is justified to neglect Brownian motion.

Coming back to the explanation, why shear thinning is observed at increased volume fractions in figure 2.1. At high shear stresses, implying high shear rates, the Peclet number is high and the randomizing effect of Brownian motion is, in part, suppressed by hydrodynamic forces. Thus, at high Peclet numbers the distribution of particles is not necessarily uniform anymore and some configurations are more common. This leads to a decrease of the suspension viscosity. The difference between (2.6) and (2.7) was also attributed to the effect of Brownian motion [6].

For the highest volume fractions in figure 2.1 the viscosity at low shear stresses is diverging.

2. An overview of the rheology of suspensions

The diverging viscosity is interpreted as an apparent yield stress [51]. The relations for the viscosity of a suspension shown so far are only valid up to volume fractions of about $\varphi \approx 0.1$. A popular relation to capture the increase in viscosity over the complete range of volume fractions is the *Krieger-Dougherty* equation [9]:

$$\eta^{(\text{hom})} = \eta \left(1 - \frac{\varphi}{\varphi_{\text{max}}} \right)^{-[\eta]\varphi_{\text{max}}}. \quad (2.14)$$

Here φ_{max} is the volume fraction at which the viscosity diverges. The Krieger-Dougherty equation is based on a mean-field argument, that every time a particle is added to the suspension the viscosity increases according to Einstein's equation, plus it assumes the empirical parameter φ_{max} . The argument for the introduction of the parameter φ_{max} is that after the addition of a particle the occupiable volume for new particles is decreased. A similar relation has been derived by Maron and Pierce [8]. In their relation the exponent in (2.14) is $[\eta]\varphi_{\text{max}} = 2$,

$$\eta^{(\text{hom})} = \eta \left(1 - \frac{\varphi}{\varphi_{\text{max}}} \right)^{-2}. \quad (2.15)$$

Typical values of φ_{max} for spherical particles are between ~ 0.5 and ~ 0.64 [57]. Other relations for the dependence of the viscosity have been derived, for example by Eilers [7], but it seems that the Krieger-Dougherty equation is the most popular [51, 52, 57]. In chapter 4 the approach of Krieger and Dougherty is used to extend results for dilute suspensions of rigid spheres to higher volume fractions.

2.1.2. Non-Newtonian matrix fluids

If the Newtonian matrix of the suspension is replaced by a non-Newtonian one it is almost impossible to find analytical solutions to the problem of how the effective properties change. The complication in predicting the effective properties of suspensions with non-Newtonian matrices is that it is generally not possible to solve analytically for the perturbed flow field around the particles. This flow field is needed to evaluate the effective properties by averaging the field over a representative volume.

Non-Newtonian behavior is a vague term and thus it should first be specified what is meant by non-Newtonian behavior in the following. The behavior of the matrix fluid is often described as a generalized Newtonian fluid [58]. Such a generalized Newtonian fluid is characterized by a viscosity that depends on the rate of strain. Generalized Newtonian fluids do not incorporate viscoelastic effects, most importantly normal stress differences [58]. Two common models to

2. An overview of the rheology of suspensions

describe the dependence of the viscosity on the shear rate $\dot{\gamma}$ are the *power law* and *Carreau* fluids [59]. The power law fluid is defined as

$$\eta = K\dot{\gamma}^n, \quad (2.16)$$

where K is called flow consistency index and has the units Pa s^{n+1} . The parameter n is the dimensionless flow index or (shear) thinning exponent. If $n = 0$ the behavior is Newtonian and if $n < 0$ it is shear thinning. The power law model has one problem: it predicts a viscosity which diverges as $\dot{\gamma}$ goes to zero. Polymers normally show a Newtonian plateau at low shear rates and become shear thinning above some critical shear rate. The Carreau model captures this experimentally observed effect and is defined as

$$\eta = \eta_0 (1 + (\lambda\dot{\gamma})^2)^{n/2}. \quad (2.17)$$

In the equation above η_0 is the zero shear viscosity in Pa s , i.e. the plateau value of the viscosity at low shear rates. The inverse of characteristic time λ corresponds to the onset of shear thinning. Interestingly the characteristic time in the Carreau model corresponds roughly to the Rouse time of an unentangled melt of short polymer chains [60]. For arbitrary flows in three dimensions the shear rate in equations (2.16) and (2.17) is replaced by the the scalar deformation rate defined as

$$\dot{\gamma} = \sqrt{2\mathbf{d} : \mathbf{d}}, \quad (2.18)$$

where \mathbf{d} is the rate of strain tensor. The colon in (2.18) denotes the double dot product, it is defined as $\mathbf{A} : \mathbf{B} = \text{tr}(\mathbf{A} \cdot \mathbf{B}) = A_{ij}B_{ji}$ where the latter expression uses Einstein's summation convention. The rate of strain tensor is defined as the symmetric part of the velocity gradient tensor

$$\mathbf{d} = \frac{1}{2} (\text{grad}(\mathbf{u}) + \text{grad}(\mathbf{u})^\top) \quad (2.19)$$

where $\text{grad}(\bullet)$ is the gradient operator, $(\bullet)^\top$ is the transpose and \mathbf{u} is the velocity field. In a simple shear flow with an applied shear rate $\dot{\gamma}_0$ the rate of strain tensor is

$$\mathbf{d} = \dot{\gamma}_0 \begin{pmatrix} 0 & \frac{1}{2} & 0 \\ \frac{1}{2} & 0 & 0 \\ 0 & 0 & 0 \end{pmatrix} \quad (2.20)$$

and the scalar deformation rate according to (2.18) is simply $\dot{\gamma}_0$.

2. An overview of the rheology of suspensions

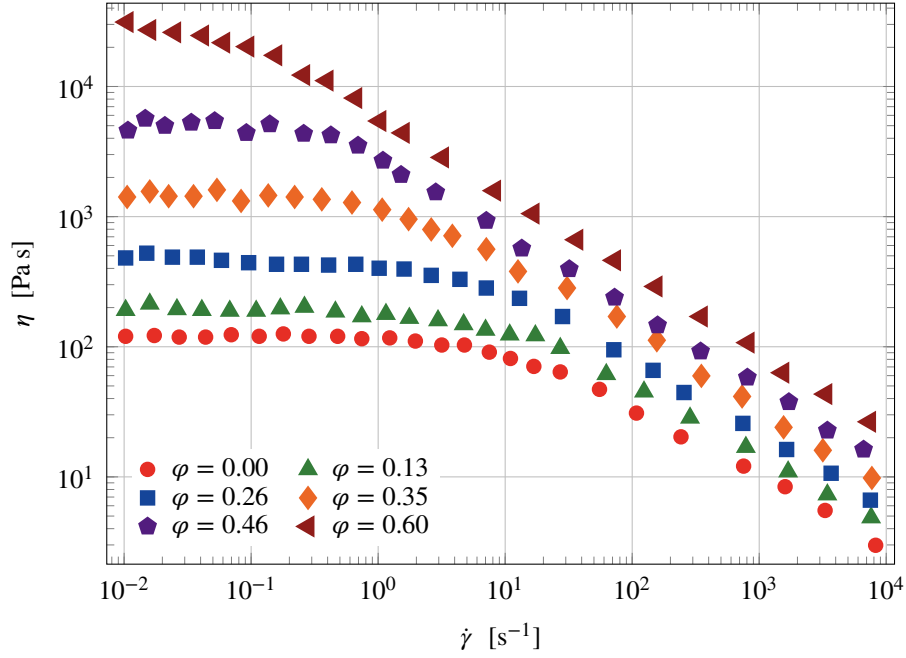


Figure 2.2.: Data of Poslinski et al. [31] for a thermoplastic melt at 150 °C filled with glass spheres with a radius of $r = 15 \mu\text{m}$ for different filler loadings φ .

Figure 2.2 shows the results of measurements done by Poslinski et al. [31] on a, not specified, thermoplastic melt¹ filled with 15 μm glass beads at various volume fractions. For the unfilled data in figure 2.2 the afore mentioned Newtonian plateau is nicely observed at low shear rates and a power law regime can be seen at high shear rates. With increasing content of filler particles the zero shear viscosity increases and the onset of shear thinning is shifted to smaller shear rates, a behavior commonly observed in filled polymers [29, 30, 48]. The basic argument for the shifting of the onset of shear thinning to lower values of the shear rate is that due to the presence of filler particles the local flow field is disturbed. Because of the disturbance the average rate of deformation inside the fluid phase is higher than the applied rate of deformation [52]. It is possible to compute the average increase of the rate of strain tensor inside of the matrix phase for arbitrary flows and particle shapes as [5, 61]

$$\langle \mathbf{d} \rangle_{\text{m}} = \frac{1}{1 - \varphi} \mathbf{d}_0 = a_{\text{d}} \mathbf{d}_0 \quad (2.21)$$

with \mathbf{d}_0 the applied rate of strain tensor on the entire outer boundary of the considered volume. The angle brackets in the above equation denote the spatial average, i.e. $\langle \bullet \rangle = \frac{1}{V} \int \bullet dV$. The

¹The paper states: “[...] a high molecular weight thermoplastic polymer obtained from the Standard Oil Engineered Materials Company.”

2. An overview of the rheology of suspensions

result given in (2.21) is independent of the constitutive relation used to describe the matrix fluid [61], hence it is valid for all kinds of fluids: Newtonian, generalized Newtonian, viscoelastic etc.

In Domurath et al. [61] the result of (2.21) is used as a strain amplification factor $a_d = 1/(1 - \varphi)$ to model the behavior of non-linear viscoelastic fluids filled with rigid spherical particles. The basic argument is that the strain rate in the constitutive relation should be amplified by a_d and the stress by the stress amplification factor a_s , as it was done by Einstein [1] when calculating the viscosity of a suspension of rigid spherical particles. Because of the introduction of amplification factors for the stress and the strain this approach is referred to as stress and strain amplification approach (SSAA). For the average microscopic stress inside the suspension with a Newtonian matrix fluid one obtains

$$\langle \boldsymbol{\sigma} \rangle_m = 2a_s \eta \langle \mathbf{d} \rangle_m = 2a_s \eta a_d \mathbf{d}_0. \quad (2.22)$$

The homogeneous macroscopic stress can be written as

$$\boldsymbol{\sigma}^{(\text{hom})} = 2\eta^{(\text{hom})} \mathbf{d}_0. \quad (2.23)$$

Comparing power densities, that is computing $P = \boldsymbol{\sigma} : \mathbf{d}$, using the two above equations for the microscopic (2.22) and macroscopic (2.23) stress, the viscosity of the suspension is then given by

$$\eta^{(\text{hom})} = a_s a_d^2 \eta. \quad (2.24)$$

For a generalized Newtonian fluid with a shear rate dependent viscosity $\eta(\dot{\gamma})$ the relation becomes

$$\eta^{(\text{hom})}(\dot{\gamma}_0) = a_s a_d^2 \eta(a_d \dot{\gamma}_0). \quad (2.25)$$

The stress amplification factor is computed as

$$a_s = \frac{X}{a_d^2} \quad (2.26)$$

to match the linear result. While this approach can qualitatively describe the observed behavior for filled polymer melts it underpredicts the strain amplification effect. That is, the onset of shear thinning is observed at lower shear rates than predicted by this approach [30, 31]. The stress amplification factor in the SSAA can be interpreted as a correction for the fluctuations in the rate of strain tensor. If the power density in the suspension is directly averaged, one obtains

$$\langle P \rangle = 2\eta \langle \mathbf{d} : \mathbf{d} \rangle \quad (2.27)$$

2. An overview of the rheology of suspensions

for a Newtonian fluid. In the case of the SSAA the average power density is computed as

$$\langle P \rangle^{(SSAA)} = 2\eta a_s \langle \mathbf{d} \rangle_m : \langle \mathbf{d} \rangle_m = 2\eta a_s a_d^2 \mathbf{d}_0 : \mathbf{d}_0. \quad (2.28)$$

Thus a_s corrects that $\langle \mathbf{d} : \mathbf{d} \rangle \neq \langle \mathbf{d} \rangle : \langle \mathbf{d} \rangle$. As in the transition from (2.27) to (2.28) an additional term about the rigid particles surface appears. This additional term is related to the stresslet, that is introduced in section 3.5.

That the choice of the strain amplification factor as used in the SSAA (2.21) does not work particularly well for the estimation of the overall properties of non-linear heterogeneous materials was also shown by Suquet [62]. Suquet proposed instead that the average strain rate in the matrix phase should be computed as the square root of the average of the squared strain rate. This can be written for a fluid as

$$\langle \mathbf{d} \rangle_m = \sqrt{\frac{\langle \mathbf{d} : \mathbf{d} \rangle_m}{\langle \mathbf{d}_0 : \mathbf{d}_0 \rangle}} \mathbf{d}_0. \quad (2.29)$$

By requiring that in the Newtonian limit the linear result should be recovered, the average strain rate in the matrix phase can be estimated by

$$\langle \mathbf{d} \rangle_m = \sqrt{\frac{X}{1 - \varphi}} \mathbf{d}_0. \quad (2.30)$$

This relation was also proposed by Schikowsky [63] for filled elastomers. The argument given by Schikowsky is basically that when the average power density inside the filled material is about X times higher than in the unfilled material one should use an amplified matrix strain such that $X \langle P \rangle$ holds. Assuming a linear relation between stress and rate of strain this gives

$$X \langle P \rangle = (1 - \varphi) \eta \sqrt{\frac{X}{1 - \varphi}} \mathbf{d}_0 : \sqrt{\frac{X}{1 - \varphi}} \mathbf{d}_0. \quad (2.31)$$

The factors of $(1 - \varphi)$ appear because the rate of strain is averaged over the matrix volume only. The proposed relation in (2.30) has been quite successfully used by Chateau et al. [34] to model the effective behavior of filled non-linear fluids with a yield stress. For the intrinsic viscosity (2.4) of a power law fluid (2.16) Chateau et al. obtained

$$[\eta]^{\text{Chateau}} = \frac{7(n + 1) + 3}{4} = \frac{7n}{4} + \frac{5}{2}. \quad (2.32)$$

2. An overview of the rheology of suspensions

Laven and Stein [33] obtained using (2.29) for the intrinsic viscosity of a power law fluid

$$[\eta]^{\text{Laven}} = \frac{n}{2} + \frac{n+2}{2} K_E^L \quad (2.33)$$

where K_E^L is referred to as Einstein coefficient in their paper. In general K_E^L will be a function of the thinning exponent n [33]. For a Newtonian fluid with $n = 0$ $K_E^L = 2.5$. Laven and Stein deduced from experimental data that $K_E^L \approx 2.5$ and independent of n . Inserting $K_E^L = 2.5$ into (2.33) gives the result of Chateau et al. (2.32). Both Chateau et al. [34] and Laven and Stein [33] showed that in the dilute limit the material behavior does not change, meaning that the thinning exponent n is constant. In chapter 4 the result of Chateau et al. will be compared with the numerical results obtained in the framework of the present PhD thesis.

Tanner et al. [35] used solutions for the effective properties of a power law material by Lee and Mear [32] and obtained

$$[\eta]^{\text{Tanner}} = 0.383 + 2.177(n + 1). \quad (2.34)$$

The result of Tanner et al. has a problem, that it does not fulfill the specific case of $n = -2$. That is for $n = -2$ Tanner's relation gives $[\eta]^{\text{Tanner}} = -1.794$, while the correct result is can be shown to be -1 . This will be explained in detail in chapter 4.

Until now only power law matrices have been discussed. As power law fluids do not describe the Newtonian region one cannot determine how the onset of shear thinning shifts. This shift is however an important characteristic of filled polymers. To investigate the shift of the shear thinning onset, numerical simulations are carried out in the present thesis and the results will be presented in chapter 4.

2.1.3. Superposition of viscosity-stress curves

With the literature results discussed above it is possible to question a claim made for polymers filled with rigid spherical particles by Barnes [48]. That is, it is possible to superimpose the flow curves for filled polymers by only a vertical shift if the data is plotted as viscosity vs. stress rather than viscosity vs. shear rate. This claim has been copied by Mewis and Wagner [57]. Highgate and Whorlow [29] found that in the system they investigated the proposed superposition did work, though they could not give a reason for this to be possible. Barnes [48] argues that the stress is uniform in a suspension, contrary to the shear rate. This argument is wrong, as can easily be shown. The stress in the fluid phase is

$$\sigma = 2\eta d \quad (2.35)$$

2. An overview of the rheology of suspensions

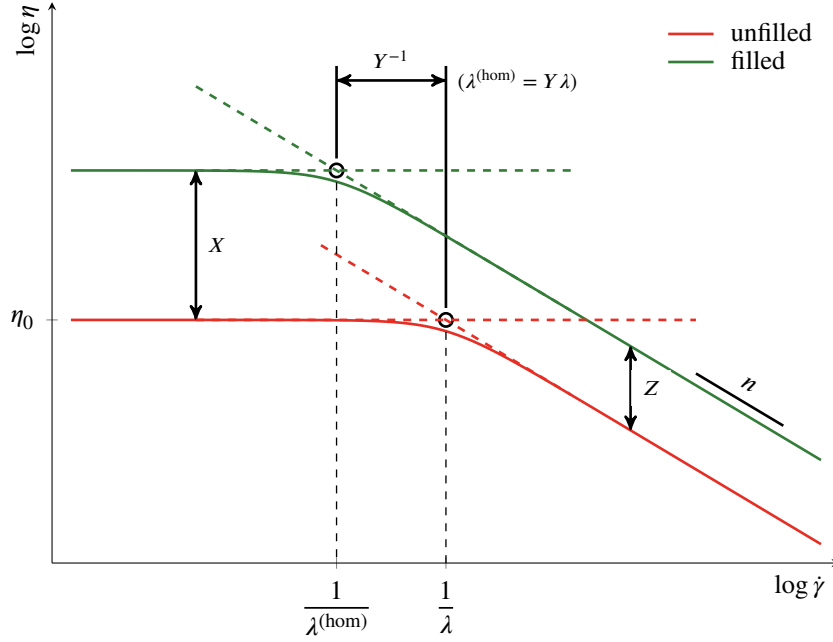


Figure 2.3.: Sketch of the shift factors for a generalized Newtonian fluid.

where for simplicity a Newtonian fluid is assumed. If the microscopic shear rate is non uniform so must be the stress, since both are related only by the scalar viscosity².

To show that from a theoretical point of view it is not possible to construct such master curves it is instructive to consider the flow curves sketched in figure 2.3. The unfilled system has a constant Newtonian plateau at shear rates smaller than λ^{-1} and a constant slope n otherwise. This flow curve can be approximated by the Carreau model (2.17). Introducing the shift factors X and Y for the filled system, see figure 2.3, into the Carreau model (2.17) gives

$$\eta = X\eta_0 \left(1 + (Y\lambda\dot{\gamma})^2\right)^{n/2}. \quad (2.36)$$

The three shift factors in figure 2.3 are related by

$$Z = XY^n. \quad (2.37)$$

The factor X corresponds to the hydrodynamic amplification factor introduced for Newtonian suspensions (2.2). The vertical shift in the power law region Z is equal to $1 + [\eta]\phi$ where $[\eta]$ is given by (2.32) or (2.34). The value of Y is related to the strain amplification factor.

²This implies that for the stress to be uniform for a non uniform rate of strain tensor, the viscosity must be ηd^{-1} (the inverse of the rate of strain tensor). In that case the stress is $\eta \mathbf{1}$, a constant hydrostatic state, thus the fluid is at rest.

2. An overview of the rheology of suspensions

Equation (2.36) can not generally be inverted to obtain an analytical relation for $\eta(\sigma)$ but it can be approximated by considering the asymptotic cases

$$\frac{Y\lambda\sigma}{X\eta_0} \ll 1 \quad \text{and} \quad \frac{Y\lambda\sigma}{X\eta_0} \gg 1 \quad (2.38)$$

the viscosity vs. stress relation corresponding to (2.36) becomes

$$\eta(\sigma) \approx X\eta_0 \left(1 + \left(\frac{Y\lambda\sigma}{X\eta_0} \right)^2 \right)^{\frac{n}{2(n+1)}}. \quad (2.39)$$

In the above relation the value of n must be restricted to $n > -1$. This restriction is not a problem since the values of n for common polymers are in the range $-1 < n \leq 0$ [28]. The derivation of (2.39) is given in appendix 2.A. From (2.39) it can be clearly seen that a construction of master curves by only a vertical shift is only possible if $X = Y$. Since Z is related to the intrinsic viscosity in the power law regime it is helpful to solve (2.37) for Z in case that $Y = X$, this gives

$$Z = X^{1+n}. \quad (2.40)$$

Inserting the solution for the hydrodynamic amplification factor X in the dilute limit (2.1) and the solution for Z given by Chateau et al. (2.32) in (2.40) one obtains

$$1 + \left(\frac{7n}{4} + \frac{5}{2} \right) \varphi = (1 + 2.5\varphi)^{1+n}. \quad (2.41)$$

For solutions of the above equation it is thus possible to superimpose the viscosity vs. stress curves by only a vertical shift. First, one can immediately see that equation (2.41) has two trivial solutions at $n = 0$ and $\varphi = 0$ but these are not of interest since the first one corresponds to a Newtonian fluid and the second one is just the pure matrix fluid. Otherwise (2.41) has no further analytical solutions. However, one can rewrite (2.41) as

$$g(\varphi, n) = (1 + 2.5\varphi)^{1+n} - \left(1 + \left(\frac{7n}{4} + \frac{5}{2} \right) \varphi \right) \quad (2.42)$$

and plot this function. This is done in figure 2.4. From the contour plot it can be seen that this function has no non trivial roots for $0 < \varphi < 1$ and $-1 < n < 0$.

Further it can be clearly seen from (2.39) for the superposition by only a vertical shift the slope of the viscosity curve should not change with increasing filler volume fraction, but such a change in the slope is commonly observed [57]. For example the slope in the data of Poslinski et al. [31]

2. An overview of the rheology of suspensions

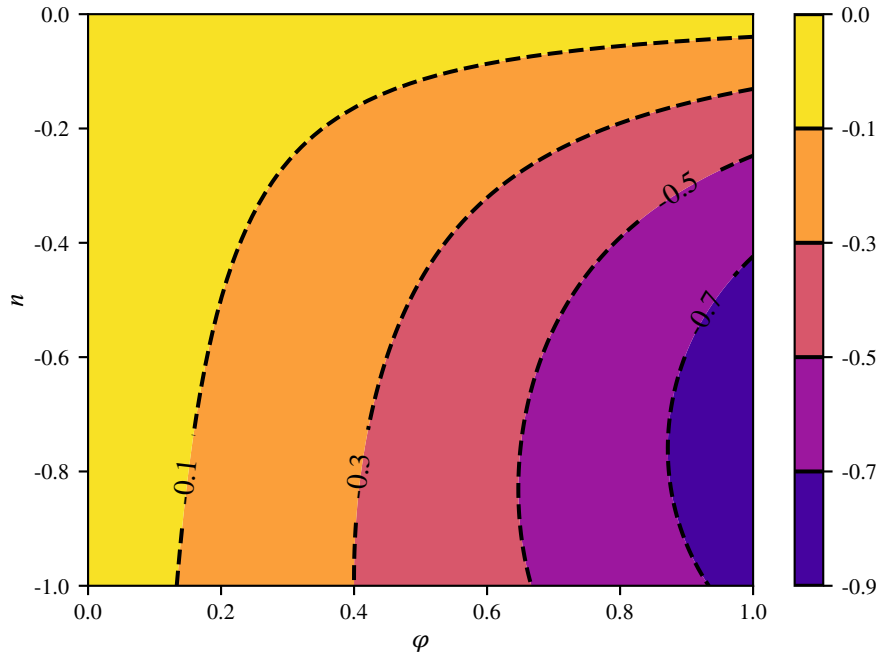


Figure 2.4.: Contour plot of the function $g(\varphi, n)$ given by (2.42). There are no non trivial roots for $0 < \varphi < 1$ and $-1 < n < 0$.

Table 2.1.: Shift factors extracted from the data of Poslinski et al. [31] by fitting to the Carreau model.

φ	0.00	0.13	0.26	0.35	0.46	(0.60)
X	1.00	1.57	3.78	12.07	43.26	(234.66)
Y	1.00	1.05	1.84	5.68	19.69	(97.72)

changes gradually from $n = -0.5$ to $n = -0.6$ between the unfilled system and the system with the highest filler loading.

Thus, while in some studies [29, 48, 57] it may look like the curves are superimposed, this is most likely just due to the presentation of the data. In figure 2.5 the shifted data of Poslinski et al. [31] is plotted according to Barnes, the data does not superimpose very well. It is also possible to extract the shift factors X and Y from the data of Poslinski et al. using the Carreau model. Table 2.1 shows the extracted shift factors. For this data set the value of X is always noticeably larger than Y . The data set for the volume fraction $\varphi = 0.6$ is set parentheses as the data does not show a Newtonian plateau.

2. An overview of the rheology of suspensions

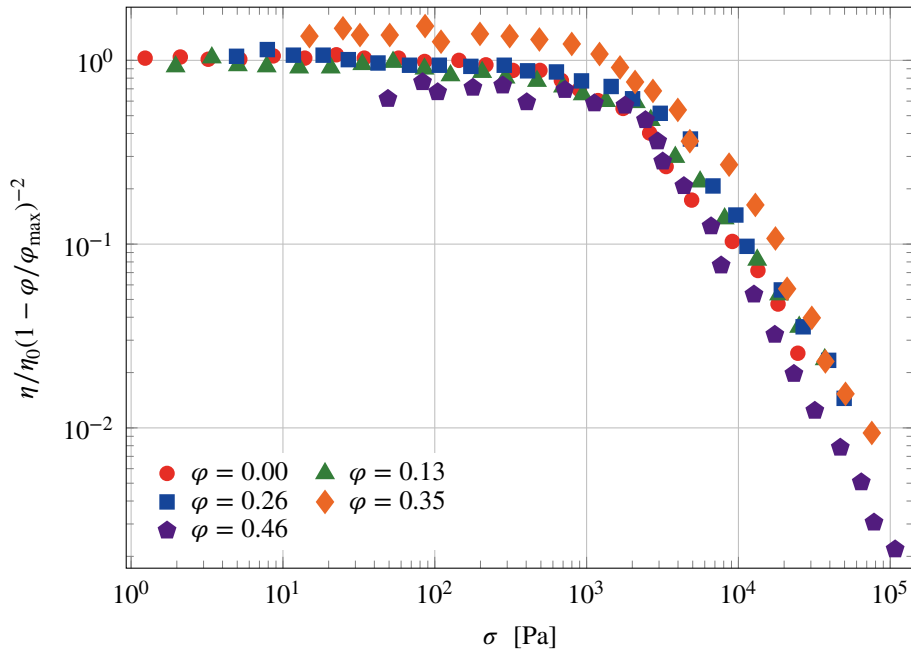


Figure 2.5.: Data of Poslinski et al. [31] shifted according to Barnes [48] using the Maron-Pierce equation (2.15), $\varphi_{\max} = 0.526$ and $\eta = 117$ Pa s. The data for $\varphi = 0.60$ is omitted because it is not possible to shift the data using the proposed Maron-Pierce equation.

2.2. Rigid non-spherical particles

Till now only suspensions of rigid spherical particles have been considered and it was shown that their behavior is quite complicated. In applications polymer melts are often filled with non-spherical particles, like rod-like fibers [22] or disk-like silicates [27]. This change in the shape of the particles complicates the description of the suspension tremendously, even in the Newtonian case. Therefore, when developing constitutive equations it is usually assumed that the particles have a rotational symmetry, which is the case for spheroids or rods with circular cross section.

2.2.1. Newtonian matrix fluids

Jeffery [10] was the first to investigate a spheroidal particle suspended in a Newtonian fluid in the absence of Brownian motion. He considered spheroidal particles as sketched in figure 2.6. The spheroid is mathematically described by

$$\frac{x^2}{a^2} + \frac{y^2 + z^2}{b^2} = 1 \quad (2.43)$$

2. An overview of the rheology of suspensions

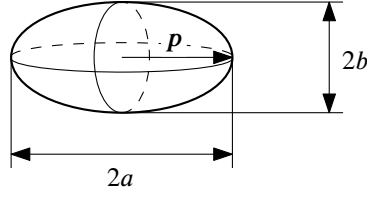


Figure 2.6.: Sketch of a spheroidal particle.

where a and b are the semi-axes of the spheroid. The orientation vector \mathbf{p} is parallel to the axis of revolution x and its length is equal to 1. The aspect ratio is defined as

$$r_a = \frac{a}{b}. \quad (2.44)$$

For an aspect ratio of $r_a = 1$ the spheroid becomes a sphere, for $r_a > 1$ the spheroid is *prolate* and for $r_a < 1$ the spheroid is *oblate*. For rods it is proposed to define an effective aspect ratio as $r_a^{(\text{eff})} \approx 0.7l/d$, where l is the length and d is the diameter [51].

Jeffery [10] has shown that the center of mass of a spheroid translates with the bulk flow of the fluid and its orientation vector \mathbf{p} rotates periodically. The time evolution of the orientation vector \mathbf{p} in the flowing suspension can be described by [51, 64]

$$\dot{\mathbf{p}} = \mathbf{p} \cdot \mathbf{w} + \left(\frac{r_a^2 - 1}{r_a^2 + 1} \right) (\mathbf{p} \cdot \mathbf{d} - \mathbf{p}\mathbf{p}\mathbf{p} : \mathbf{d}). \quad (2.45)$$

Here \mathbf{w} is the vorticity tensor defined as the non-symmetric part of the velocity gradient tensor

$$\mathbf{w} = \frac{1}{2} (\text{grad}(\mathbf{u}) - \text{grad}(\mathbf{u})^\top). \quad (2.46)$$

In a shear flow a spheroidal particle rotates periodically in time. This rotation is called the Jeffery orbit. Jeffery also computed the intrinsic viscosity for a dilute suspension of spheroidal particles but due to the rotation of the particles he only gave minimum and maximum values. The minimum value for the intrinsic viscosity is reported to be 2, while the maximum is infinity [10].

As in the case of spherical particles the presence of Brownian motion influences the behavior of the suspension. Without Brownian motion the particle can align along the flow direction. This alignment is for example observed in elongational flows or in shear flows, when the aspect ratio of the particle tends to either zero or infinity [51]. The influence of Brownian motion is captured

2. An overview of the rheology of suspensions

in the *rotational Peclet number* that is defined as

$$\text{Pe}_r \equiv \frac{\dot{\gamma}}{D_r}. \quad (2.47)$$

The value of the rotatory diffusivity D_r in the above equation can be found in literature [51]. For a spheroidal particle the rotatory diffusivity in the dilute limit is given by [51]

$$D_{r0} = \frac{3k_B T (\ln(2r_a) - 0.5)}{\pi\eta l^3} \quad (2.48)$$

where $l = 2 \max(a, b)$.

In the case of spherical particles the dilute limit ends slightly above 3 % volume fraction. For nonspherical particles the dilute limit is normally much smaller. Larson [51] gives an estimate for the crossover volume fraction from dilute to semidilute concentration regime for rods with aspect ratios of $r_a = l/d \gtrsim 50$ as

$$\varphi_{\text{dilute}} \approx 24 \left(\frac{d}{l} \right)^2. \quad (2.49)$$

Ericksen [65] developed a theory of transversely isotropic fluids that is properly invariant, it neither violates the laws of thermodynamics nor objectivity³. A transversely isotropic fluid is defined as a fluid which has one preferred direction. In the preferred direction the material behaves differently than perpendicular to it. Thus a transversely isotropic fluid shows a rotational symmetry about its preferred direction. Based on the results of Jeffery, Hand [11] was able to show that the stress in a dilute suspension of spheroidal particles can be described as a special case of Ericksen's theory. Giesekus [66] also used Jeffery's results to evaluate the viscosity of dilute suspension of spheroids. Using the results of Ericksen and Giesekus, Lipscomb et al. [14] proposed a model for dilute suspensions of spheroidal particles in the absence of Brownian motion. In Lipscomb's work the stress is given by the transversely isotropic fluid (TIF) equation

$$\boldsymbol{\tau} = -p\mathbf{1} + 2\eta\mathbf{d} + \underbrace{2\eta\varphi (A\mathbf{a}_4 : \mathbf{d} + B(\mathbf{d} \cdot \mathbf{a}_2 + \mathbf{a}_2 \cdot \mathbf{d}) + C\mathbf{d})}_{\text{particle contribution}}. \quad (2.50)$$

Here p is the pressure and A , B and C are rheological coefficients. The tensors \mathbf{a}_2 and \mathbf{a}_4 are orientation tensors: \mathbf{a}_2 is a second order tensor and \mathbf{a}_4 is of fourth order. For example the orientation

³That is, it is independent of the observer.

2. An overview of the rheology of suspensions

tensors are given for fixed particles that all have the same orientation as

$$\mathbf{a}_2 = \mathbf{p}\mathbf{p} \quad (2.51a)$$

$$\mathbf{a}_4 = \mathbf{p}\mathbf{p}\mathbf{p}\mathbf{p}, \quad (2.51b)$$

thus the preferred direction in the fluid is along \mathbf{p} . Using (2.45) for the time evolution of \mathbf{p} , it is possible to compute the time evolution of the stress. In case of differently oriented particles it is necessary to average over the orientation distribution function of the particles. The tensor \mathbf{a}_4 is generally unknown in such a case and must be approximated using \mathbf{a}_2 . This averaging complicates the calculations of these tensors significantly and will not be discussed here, since for the following discussion it is sufficient to consider a single fixed particle. In the presence of Brownian motion an additional term is added to (2.50) that depends on the rotatory diffusivity D_r of the particle. This term can be found in Hinch and Leal [13, 67]. More on the averaging and on proper closure approximations for $\mathbf{a}_4 = \mathcal{f}(\mathbf{a}_2)$ can be found in Lipscomb et al. [14] or for a newer work see Binetruy et al. [68].

Lipscomb et al. gives the following expressions for the rheological coefficients A , B and C

$$A = \frac{(r_a^2 - 1)^2 (4\Theta r_a^2 + 5\Theta + 2r_a^2 - 11)}{r_a^2 (3\Theta + 2r_a^2 - 5) (2\Theta r_a^2 + \Theta - 3)} - \frac{4 (r_a^2 - 1)^2}{(r_a^2 + 1) (r_a^2 - 3\Theta r_a^2 + 2)} \quad (2.52a)$$

$$B = -\frac{4 (r_a^2 - 1)^2}{r_a^2 (3\Theta + 2r_a^2 - 5)} + \frac{2 (r_a^2 - 1)^2}{(r_a^2 + 1) (r_a^2 - 3\Theta r_a^2 + 2)} \quad (2.52b)$$

$$C = \frac{4 (r_a^2 - 1)^2}{r_a^2 (3\Theta + 2r_a^2 - 5)} \quad (2.52c)$$

where

$$\Theta = \begin{cases} \frac{1}{2r_a \sqrt{r_a^2 - 1}} \ln \left(\frac{r_a + \sqrt{r_a^2 - 1}}{r_a - \sqrt{r_a^2 - 1}} \right) & \text{if } r_a > 1 \\ \frac{1}{r_a \sqrt{1 - r_a^2}} \arctan \left(\frac{\sqrt{1 - r_a^2}}{r_a} \right) & \text{if } r_a < 1. \end{cases} \quad (2.53)$$

2. An overview of the rheology of suspensions

Other relations for the factors A , B and C have been derived for example by Hinch and Leal [13].

For rods with length l , diameter d and aspect ratio $r_a = l/d$ Batchelor [69, 70] derived using slender-body theory that

$$A = \frac{r_a^2}{3 \ln(2r_a)} f(\epsilon) \quad (2.54)$$

where the function f is given by

$$f(\epsilon) = \frac{1 + 0.64\epsilon}{1 - 1.5\epsilon} + 1.659\epsilon^2 + \mathcal{O}(\epsilon^3) \quad (2.55)$$

with

$$\epsilon = \ln(2r_a)^{-1}. \quad (2.56)$$

The parameters $B = C = 0$ for rods, according to slender-body theory [69, 70]. For a sphere $A = B = 0$ and $C = 2.5$, that is Einstein's result is recovered.

In the cases where $r_a \gg 1$ and $r_a \ll 1$ the rheological coefficients given by Lipscomb et al. simplify significantly. Table 2.2 presents the simplified rheological coefficients and additionally those of Hinch and Leal [13]. In the habilitation thesis of Ausias [71] an extended overview of more results for the rheological coefficients A , B and C is given. Also Kim and Karrila [64] and Férec [72] discuss some results for the rheological coefficients. In figures 2.7 to 2.9 the result of Lipscomb et al. for the rheological coefficients given by equations (2.52) is plotted, as well the asymptotic solution of Hinch and Leal [13] and the approximation of Lipscomb et al. as given in table 2.2. Further certain special cases for the values of the rheological coefficients are marked in the figures. It can be seen that the asymptotic solution of Hinch and Leal coincides with the solution given by Lipscomb et al. in (2.52).

From table 2.2 it can be seen that there are differences in the predictions for the rheological coefficients in the TIF equation. The author of this PhD thesis is not aware of any work that tried to compute these factors using numerical simulations. The only known work to the author is by Lee and Mear [32] where the particle orientation is such that \mathbf{p} is aligned with the load direction. In chapter 5 numerical simulations are performed, for the first time, to determine the rheological coefficients A , B and C for both Newtonian and non-Newtonian matrices.

2. An overview of the rheology of suspensions

Table 2.2.: Rheological coefficients A , B and C for the TIF equation (2.50) for the cases when $r_a \gg 1$ and $r_a \ll 1$ from Lipscomb et al. [14] and Hinch and Leal [13].

		A	B	C
$r_a \gg 1$	Hinch and Leal	$\frac{r_a^2}{2(\ln(2r_a) - 1.5)}$	$\frac{6\ln(2r_a) - 11}{r_a^2}$	2
	Lipscomb et al.	$\frac{r_a^2}{2\ln(r_a)}$	0	2
$r_a \ll 1$	Hinch and Leal	$\frac{10}{3\pi r_a} + \frac{208}{9\pi^2} - 2$	$-\frac{8}{3\pi r_a} + 1 - \frac{128}{9\pi^2}$	$\frac{8}{3\pi r_a}$
	Lipscomb et al.	$\frac{10}{3\pi r_a}$	$-\frac{8}{3\pi r_a}$	$\frac{8}{3\pi r_a}$

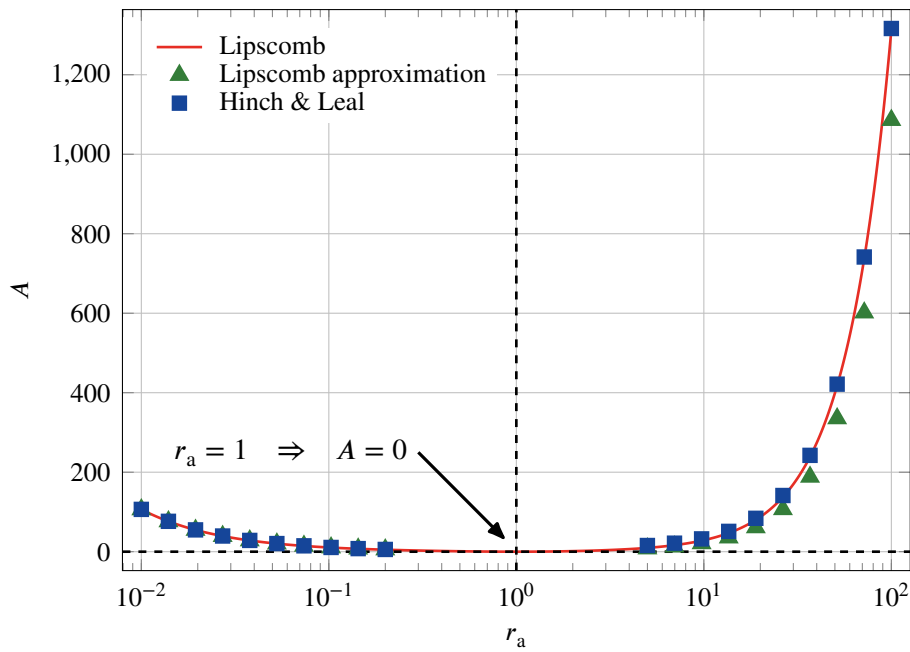


Figure 2.7.: Comparison of the rheological coefficient A given by Lipscomb's solution (2.52) and the relations presented in table 2.2. The approximation of Lipscomb et al. is not good for large aspect ratios.

2. An overview of the rheology of suspensions

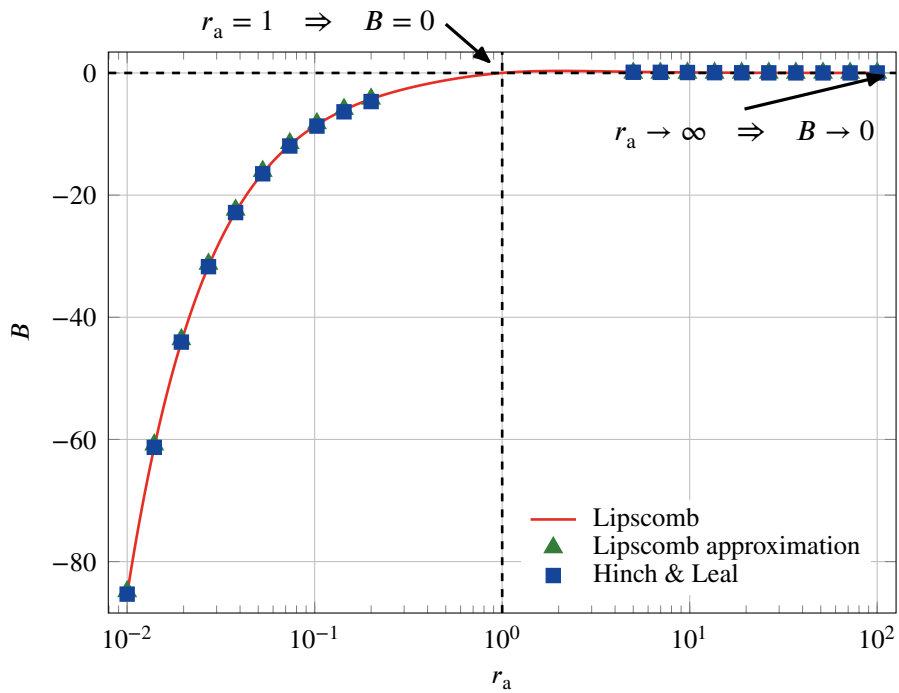


Figure 2.8.: Comparison of the rheological coefficient B given Lipscomb's solution (2.52) and the relations presented in table 2.2.

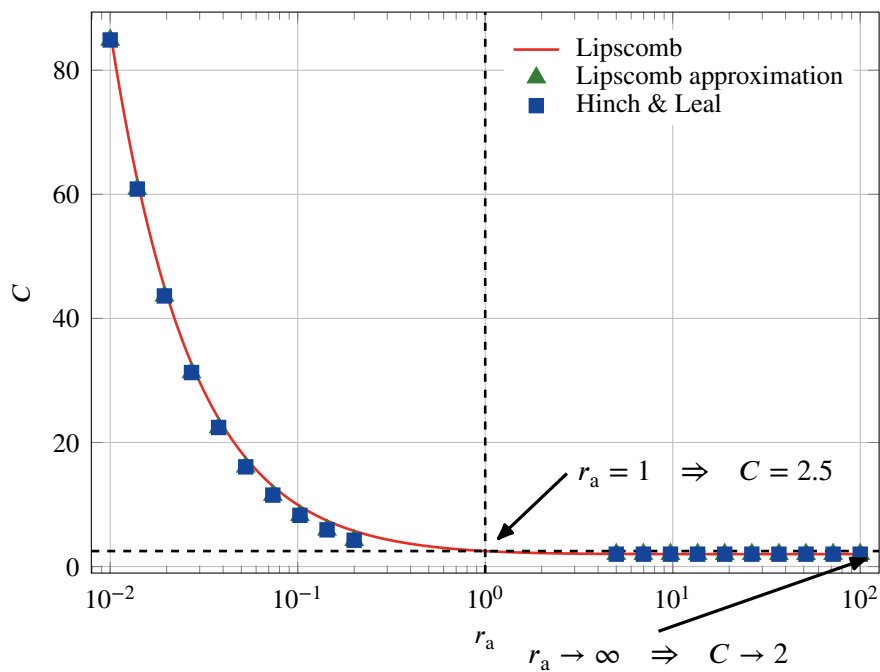


Figure 2.9.: Comparison of the rheological coefficient C given by Lipscomb's solution (2.52) and the relations presented in table 2.2.

2. An overview of the rheology of suspensions

2.2.2. Non-Newtonian matrix fluids

For non-Newtonian fluids filled with spheroidal particles not so many theoretical works can be found, besides the work of Lee and Mear [32] that was already mentioned multiple times.

For example one finds a proposal of Thomasset et al. [73] to replace the Newtonian viscosity in the TIF equation with a Carreau law (2.17) and to use Lipscomb's coefficients. Another approach in a similar style can be found in Wang et al. [49] and Kagarise et al. [50]. In these two works the authors also assume the validity of the TIF equation for a non Newtonian fluid with Lipscomb's coefficients computed for a Newtonian fluid and replace the Newtonian viscosity by a shear-thinning viscosity described by the Giesekus model. Considering the discussion in section 2.1.2, these approaches seem to be a little bit brute force. To understand this, let us consider the TIF equation (2.50) for spherical particles

$$\boldsymbol{\tau} = -p\mathbf{1} + 2\eta\mathbf{d} + 2\eta\varphi C\mathbf{d} \quad (2.57)$$

which predicts the viscosity of the suspension

$$\eta = \eta(1 + C\varphi). \quad (2.58)$$

Comparing the above equation with Einstein's result (2.5) gives $C = [\eta]$. For non-Newtonian matrix fluids it was shown in section 2.1.2 that the intrinsic viscosity $[\eta]$ in a power law fluid depends on the flow index n . This raises the question: *Why should the coefficient C be independent of the flow index n for non-spherical particles, while it depends on n for spheres?* Whether the rheological coefficients A , B and C are really independent of n will be investigated in chapter 5.

Two interesting works are those of Souloumiac and Vincent [37] and Gibson and Toll [36]. While these two works consider rod-like particles, where only the rheological coefficient A is non-zero in the TIF equation, the basic results are very interesting. Both works study a power law fluid that contains rigid rods. Souloumiac and Vincent [37] used a cell based model and in Gibson and Toll [36] a micro-mechanical approach is used. In both calculations the particle contribution to the stress tensor for a fixed rod-like particle in a power law fluid can be written as

$$\boldsymbol{\sigma} = 2\varphi A^* |\mathbf{p} \cdot \mathbf{d} \cdot \mathbf{p}|^n \mathbf{a}_4 : \mathbf{d} \quad (2.59)$$

where \mathbf{a}_4 is given by (2.51b). The parameter A^* depends on the flow index n and on the geometry of the particle. This fortifies the assumption that the rheological coefficients in the TIF equation depend on the flow index for power law fluids. Such an equation has been used in Férec et al. [74] to model elongational behavior of fiber filled polymers.

2. An overview of the rheology of suspensions

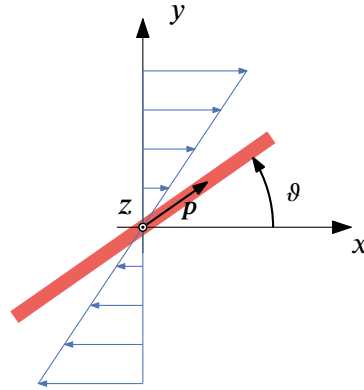


Figure 2.10.: Sketch of a rod in a simple shear flow.

One should nevertheless be careful using the factor $|\mathbf{p} \cdot \mathbf{d} \cdot \mathbf{p}|^n$ as it diverges for many cases. For example consider the case of a rod placed in a simple shear flow as sketched in figure 2.10. The orientation vector for this configuration is defined as

$$\mathbf{p} = \begin{pmatrix} \cos(\vartheta) \\ \sin(\vartheta) \\ 0 \end{pmatrix}, \quad (2.60)$$

where the angle take values $\vartheta \in [0, \pi]$. The rate of strain tensor in simple shear is given by (2.20). Inserting the relations for \mathbf{p} and \mathbf{d} results in

$$|\mathbf{p} \cdot \mathbf{d} \cdot \mathbf{p}|^n = |\dot{\gamma}_0 \sin(\vartheta) \cos(\vartheta)|^n. \quad (2.61)$$

For shear-thinning fluids with $n < 0$ this expression diverges as ϑ approaches 0, $\pi/2$ or π . Note that this is not a problem in the relation for the stress (2.59) as it can be rewritten as

$$\boldsymbol{\sigma} = 2\varphi A^* |\mathbf{p} \cdot \mathbf{d} \cdot \mathbf{p}|^n (\mathbf{p} \cdot \mathbf{d} \cdot \mathbf{p}) \mathbf{p} \mathbf{p} = 2\varphi A^* \text{sgn}(\mathbf{p} \cdot \mathbf{d} \cdot \mathbf{p}) |\mathbf{p} \cdot \mathbf{d} \cdot \mathbf{p}|^{n+1} \mathbf{p} \mathbf{p} \quad (2.62)$$

where $\text{sgn}(\bullet)$ is the signum function. Thus, for $n > -1$ the stress will not diverge.

Since there is no such a relation as (2.59) for spheroids, in chapter 5 the numerical solution will be compared with the TIF equation to determine the coefficients A , B and C . As follows from (2.59) there is a chance that in the power law regime the coefficients will not only depend on n but also on \mathbf{p} and \mathbf{d} . If this is the case, it would complicate the problem immensely.

2.3. Summary

- The viscosity of a suspension composed of a Newtonian matrix fluid and rigid particles can be described in the dilute limit as

$$\eta^{(\text{hom})} = (1 + [\eta]\varphi)\eta$$

with the intrinsic viscosity $[\eta] = 2.5$ for spheres.

- If the matrix fluid of a dilute suspension is given by a power law model the intrinsic viscosity depends on the thinning exponent n .
- It can be shown that a superposition of viscosity - stress curves for polymer melts filled with rigid spherical particles by only a vertical shift is unlikely.
- If the particles are rigid spheroids and the matrix fluid is Newtonian, the behavior of the suspension can be described by the transversely isotropic fluid (TIF) equation with the rheological coefficients given by Lipscomb et al.
- In case of a non Newtonian matrix fluid the rheological coefficients in the TIF equation might depend on the particle orientation.

2. An overview of the rheology of suspensions

2.A. Viscosity as function of stress

To obtain the viscosity as a function of the stress such that $\eta = \eta(\sigma)$ one can invert the relation for the stress:

$$\sigma = \eta(\dot{\gamma})\dot{\gamma} \quad (2.63)$$

to obtain the shear rate as a function of the stress $\dot{\gamma} = \dot{\gamma}(\sigma)$ and insert this relation into $\eta(\dot{\gamma})$.

The shear stress in the modified Carreau model given by (2.36) is

$$\sigma = X\eta_0 \left(1 + (Y\lambda\dot{\gamma})^2\right)^{n/2} \dot{\gamma}. \quad (2.64)$$

The above relation cannot generally be analytically inverted for $n \leq 0$. The inversion is nevertheless possible by considering only the asymptotic cases: the Newtonian limit where $Y\lambda\dot{\gamma} \ll 1$ and the power law regime with $Y\lambda\dot{\gamma} \gg 1$.

In the Newtonian case the expression for $\eta(\sigma)$ can be directly written down as in this case (2.64) is simply constant and thus

$$\eta = X\eta_0. \quad (2.65)$$

In the power law regime (2.64) reduces to

$$\sigma = X\eta_0(Y\lambda)^n \dot{\gamma}^{n+1}, \quad (2.66)$$

where it is assumed, without loss of generality, that $\dot{\gamma} \geq 0$. The inversion of the above relation results in

$$\dot{\gamma} = \left(\frac{\sigma}{X\eta_0(Y\lambda)^n}\right)^{1/(n+1)}. \quad (2.67)$$

This expression is undefined for $n = -1$. The shear rate $\dot{\gamma}$ diverges as the stress σ approaches zero for $n < -1$ and the shear rate approaches zero as the stress goes to infinity. Thus for $n \leq -1$ (2.67) gives unphysical results. This is because (2.64) is not a strictly monotonically increasing functions for $n \leq -1$, $\sigma(\dot{\gamma})$ is not one-to-one.

Inserting (2.67) into (2.36) under the assumption that $Y\lambda\dot{\gamma} \gg 1$ gives

$$\eta(\sigma) = X\eta_0 \left(\frac{Y\lambda\sigma}{X\eta_0}\right)^{\frac{n}{n+1}}. \quad (2.68)$$

With equations (2.65) and (2.68) it is possible to construct a function for the dependence of the viscosity on the stress. At small stresses the viscosity should have the constant value of $X\eta_0$ and at high stresses it should follow the power law given by (2.68). In analogy with the Carreau

2. An overview of the rheology of suspensions

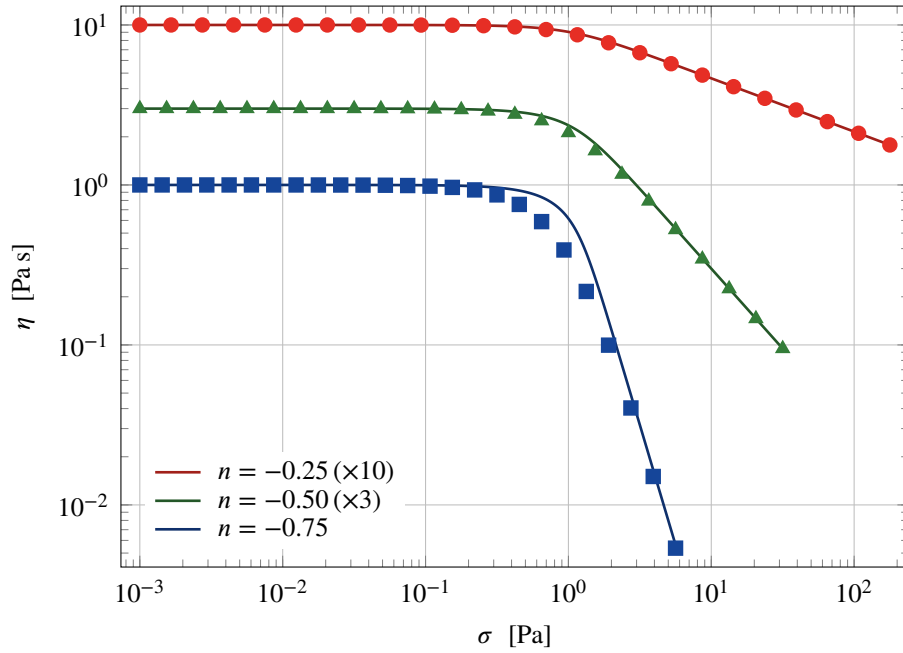


Figure 2.11.: Viscosity as a function of stress. Comparison of the approximation (2.69) with the numerically computed exact values for various n . The curves are shifted by a factor, indicated in parenthesis, for better comparability. All other parameters are set to unity.

model one may write

$$\eta(\sigma) \approx X\eta_0 \left(1 + \left(\frac{Y\lambda\sigma}{X\eta_0} \right)^2 \right)^{\frac{n}{2(n+1)}}. \quad (2.69)$$

This equation clearly fulfills (2.65) when $(Y\lambda\sigma)/(X\eta_0) \ll 1$ and (2.68) when $(Y\lambda\sigma)/(X\eta_0) \gg 1$. The crossover from the constant plateau to the power law is fairly well captured until n about -0.5 . For smaller values of n the crossover described by (2.69) is too smooth as the actual crossover becomes almost a kink. Figure 2.11 shows a comparison of the approximation given by (2.69) with the actual viscosity vs. stress function for different values of n . It is also possible to improve the approximation of the crossover by introducing a free parameter m into (2.69) such that

$$\eta(\sigma) \approx X\eta_0 \left(1 + \left(\frac{Y\lambda\sigma}{X\eta_0} \right)^m \right)^{\frac{n}{m(n+1)}}. \quad (2.70)$$

With increasing values of m the crossover described by (2.70) becomes more and more like a kink.

3. Computational fluid dynamics simulations of suspensions

3.1. Introduction

In the following chapters computational fluid dynamics simulations using the finite element method (FEM) are performed to compute bulk properties of suspensions of rigid particles. For the simulations a representative volume element (RVE) that is subjected to a macroscopic velocity at its outer boundaries is considered. The RVE is a cube with a spheroidal hole at its center as sketched in figure 3.1. For convenience it is assumed that the centers of mass of the cube and of the particle coincide at $\mathbf{X}_{\text{RVE}} = \mathbf{X}_p = (0, 0, 0)^T$. The particle orientation is described by the orientation vector \mathbf{p} . In general the spheroidal particle at the center of the RVE will translate and rotate in the flow. For certain applied boundary conditions for the velocity the spheroidal particle will only rotate or neither rotate nor translate. Under these conditions the RVE can be reduced due to symmetry of the problem.

If the particle is oriented along one of the coordinate axes and the macroscopically applied velocity corresponds to an elongational flow, the particle will not rotate nor translate if it is placed in the stagnation point of the elongational flow. Such a case was considered by Einstein in his calculation of the viscosity of a dilute suspension [1]. In general an elongational flow can be expressed by a rate of strain tensor of the form

$$\mathbf{d} = \begin{pmatrix} \dot{\epsilon}_1 & 0 & 0 \\ 0 & \dot{\epsilon}_2 & 0 \\ 0 & 0 & -(\dot{\epsilon}_1 + \dot{\epsilon}_2) \end{pmatrix} \quad (3.1)$$

where $\dot{\epsilon}_1$ and $\dot{\epsilon}_2$ are prescribed strain rates. The vorticity tensor \mathbf{w} is zero for an elongational flow. As the fluid is assumed to be incompressible the rate of strain tensor is traceless. The velocity at

3. Computational fluid dynamics simulations of suspensions

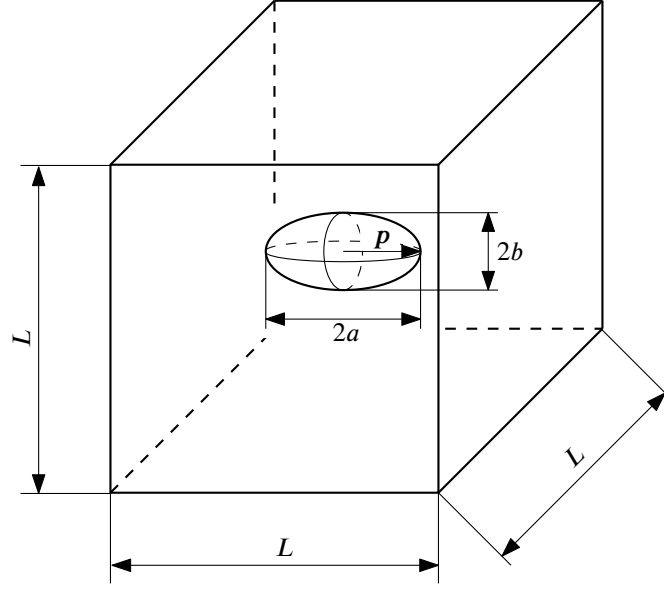


Figure 3.1.: Sketch of the computational domain.

some point \mathbf{x} can be expressed using \mathbf{d} as

$$\mathbf{u} = \mathbf{d} \cdot \mathbf{x}. \quad (3.2)$$

In case of a uniaxial elongational flow $\dot{\epsilon}_1 = \dot{\epsilon}$ and $\dot{\epsilon}_2 = -0.5\dot{\epsilon}$. For a planar flow $\dot{\epsilon}_1 = \dot{\epsilon}$ and $\dot{\epsilon}_2 = -\dot{\epsilon}$. As it is assumed here that the centers of mass of the RVE cube and of the particle are placed at $(0, 0, 0)^\top$, the particle is in fact placed in the stagnation point.

If in a uniaxial or planar flow the particle orientation vector \mathbf{p} coincides with one of the coordinate axes it is possible to exploit the symmetry of the problem and only consider one eighth of the RVE. In such a case the particle is in a stable or metastable position: the orientation vector \mathbf{p} will not evolve in time. For Newtonian matrix fluids one can use equation (2.45) to determine the time evolution of the orientation vector \mathbf{p} . Equation (2.45) simplifies to

$$\dot{\mathbf{p}} = \left(\frac{r_a^2 - 1}{r_a^2 + 1} \right) (\mathbf{p} \cdot \mathbf{d} - \mathbf{p}\mathbf{p}\mathbf{p} : \mathbf{d}) \quad (3.3)$$

since the vorticity tensor is zero for the flow considered. Inserting (3.1) into (3.3) and choosing \mathbf{p} aligned with coordinate axes as $\mathbf{p} = (1, 0, 0)^\top$ or $\mathbf{p} = (0, 1, 0)^\top$ or $\mathbf{p} = (0, 0, 1)^\top$ gives for all

3. Computational fluid dynamics simulations of suspensions

considered orientations the same result as

$$\dot{\mathbf{p}} = \begin{pmatrix} \frac{r_a^2 - 1}{r_a^2 + 1} \\ 0 \\ 0 \end{pmatrix} \quad (3.4)$$

thus the particle orientation does not change. This calculation is formally only correct for a Newtonian matrix fluid, as (3.3) was derived for this kind of fluids, nevertheless it is also true for a generalized Newtonian fluid due to the symmetry of the problem. The particle neither rotates nor translates because the forces exerted by the fluid on the particle must be symmetric since the particle is symmetrically positioned in a symmetric flow field and thus the total forces cancel. Hence the particle remains at rest. This symmetry is exploited in the calculations to follow. Further as the particle stays at rest the simulation procedure can be considerably simplified as described in section 3.3.

Another case where symmetry can be exploited to reduce the computational effort is a simple shear flow given by the rate of strain and vorticity tensors as

$$\mathbf{d} = \frac{1}{2} \begin{pmatrix} 0 & \dot{\gamma} & 0 \\ \dot{\gamma} & 0 & 0 \\ 0 & 0 & 0 \end{pmatrix} \quad \text{and} \quad \mathbf{w} = \frac{1}{2} \begin{pmatrix} 0 & \dot{\gamma} & 0 \\ -\dot{\gamma} & 0 & 0 \\ 0 & 0 & 0 \end{pmatrix} \quad (3.5)$$

where $\dot{\gamma}$ is the prescribed shear rate. If the orientation vector of the particle \mathbf{p} lies in the $x-y$ -plane it is possible to exploit the symmetry of the problem and solve only on one half of the RVE. The velocity at some point \mathbf{x} is expressed by

$$\mathbf{u} = (\mathbf{d} + \mathbf{w}) \cdot \mathbf{x}. \quad (3.6)$$

Using equation (2.45) and assuming the particle is oriented along the x -axis, one obtains for the evolution of the particle orientation in this configuration

$$\dot{\mathbf{p}} = \frac{\dot{\gamma}}{2} \left(\left(\frac{r_a^2 - 1}{r_a^2 + 1} \right) - 1 \right) \begin{pmatrix} 0 \\ 1 \\ 0 \end{pmatrix}. \quad (3.7)$$

Thus, strongly elongated particles will not change their orientation as $(r_a^2 - 1)/(r_a^2 + 1) \rightarrow 1$ as $r_a \rightarrow \infty$. Similar to the elongational flow the particle will not translate in a simple shear flow as the forces exerted on it by the fluid are in equilibrium if the particle center of mass is placed

3. Computational fluid dynamics simulations of suspensions

at $\mathbf{X}_p = (0, x_2, x_3)^\top$. However, the particle can rotate in a simple shear flow. This makes the computation in a shear flow more complicated compared to that in an elongational flow, as one also has to solve for the particle rotation. The simulation procedure for a rotating particle in a simple shear flow is described in section 3.4.

3.2. Computational domain and mesh generation

The domain on which the simulations are performed is a cube of length L with a spheroidal hole at its center, as sketched in figure 3.1. The spheroidal hole is described by its semi-axes a and b (2.43) and its orientation is given by \mathbf{p} . The center of mass of the cube and the particle are, for convenience, located at $\mathbf{X}_{\text{RVE}} = \mathbf{X}_p = (0, 0, 0)^\top$. The orientation vector \mathbf{p} is parallel to the axis of revolution and is of unit length.

For the forthcoming computations it is convenient to prescribe the volume V_p and aspect ratio r_a of the spheroidal particle instead of its semi-axes. For a prescribed volume and aspect ratio the semi-axes are then defined by

$$a = \left(\frac{3r_a^2 V_p}{4\pi} \right)^{1/3} \quad (3.8a)$$

$$b = \frac{a}{r_a}. \quad (3.8b)$$

To capture the geometry of the particle and to solve the flow problem accurately, the mesh is graded towards the particle surface. That is the elements near the particle are smaller than far away from the particle. For particles that differ considerably from a sphere the element sizes on the particle surface are scaled by the curvature of the particle surface. The Gaussian curvature of a spheroid aligned with the x -axis is given by

$$K = \frac{a^6}{[a^4 + (b^2 - a^2)x^2]^2} \quad (3.9)$$

where $x \in [-a, a]$. The actual meshes are generated by *Gmsh* [75] using its Frontal algorithms for the 2d and 3d meshing. The grading is done using linear interpolation of the element sizes. Figure 3.2 shows an example mesh for an oblate spheroidal particle, here only one half of the RVE is meshed as symmetry of the problem is exploited. Note that the volume of the rigid particle is not explicitly meshed, it is represented as a hole.

3. Computational fluid dynamics simulations of suspensions

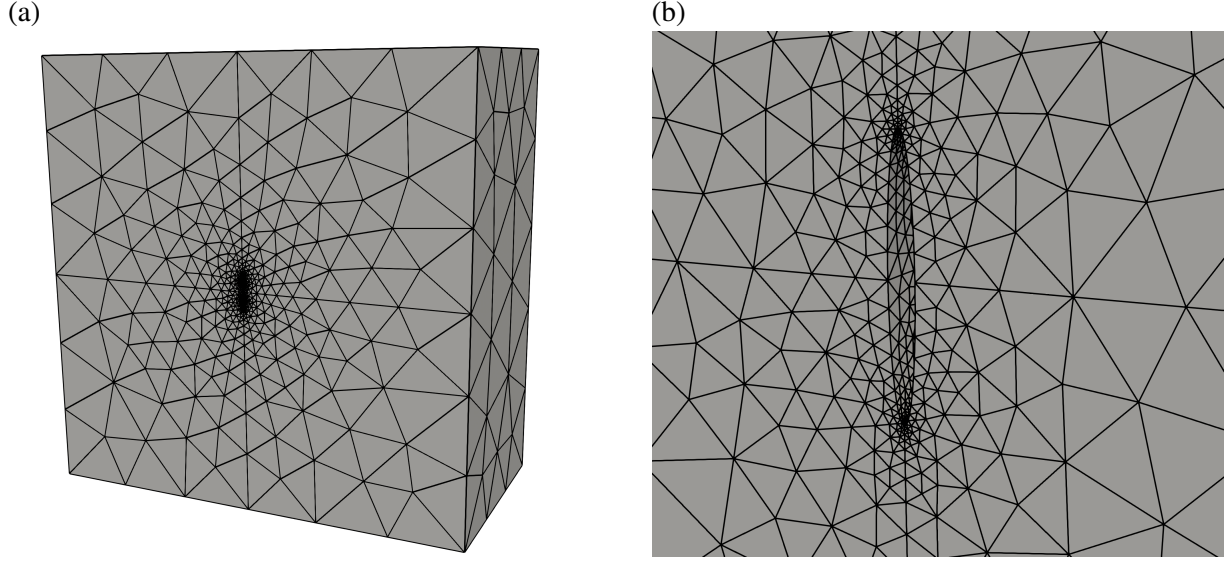


Figure 3.2.: Example mesh for an oblate spheroid with an aspect ratio of 1/10, 1/2 of the domain is meshed. (a) full mesh, (b) closeup of the region near the particle.

3.3. Fixed particle in elongational flows

3.3.1. Problem description

When we consider the particle to be in a position where it does not rotate nor translate, the problem is only described by the flow of the fluid matrix around a fixed particle.

The flow of a possibly non-linear incompressible fluid is described by the Cauchy momentum equation and the continuity equation:

$$\rho \left(\frac{\partial \mathbf{u}}{\partial t} + \mathbf{u} \cdot \text{grad}(\mathbf{u}) \right) = \text{div}(\boldsymbol{\sigma}) - \text{grad}(p) \quad (3.10a)$$

$$\text{div}(\mathbf{u}) = 0. \quad (3.10b)$$

Here (3.10a) is the balance of momentum and (3.10b) is the continuity equation for an incompressible fluid. In the above equations p is the pressure, \mathbf{u} is the fluid velocity, ρ its density and $\boldsymbol{\sigma}$ is the stress tensor that may depend nonlinearly on the velocity¹,

$$\boldsymbol{\sigma} = \eta(\mathbf{u}) \mathbf{d}. \quad (3.11)$$

¹In the following the dependence on the primary variables, the ones that are solved for in the numerical method, is indicated since this makes the following equations much clearer. In the numerical scheme used, this is the velocity \mathbf{u} and the pressure p .

3. Computational fluid dynamics simulations of suspensions

The left hand side of (3.10a) accounts for fluid inertia (transport of momentum) and the right hand side for internal friction (viscous forces). If a Newtonian fluid with constant viscosity η is assumed, (3.10) reduces to the incompressible Navier-Stokes equations. It is often customary to rewrite (3.10) in a dimensionless form using the Reynolds number Re

$$\text{Re} \left(\frac{\partial \mathbf{u}'}{\partial t'} + \mathbf{u}' \cdot \text{grad}(\mathbf{u}') \right) = \text{div}(\boldsymbol{\sigma}') - \text{grad}(p') \quad (3.12a)$$

$$\text{div}(\mathbf{u}') = 0. \quad (3.12b)$$

where the variables with a prime are the dimensionless counterparts, e.g. $\mathbf{u}' = \mathbf{u}/U$ and $t' = tU/L_c$ with U a characteristic fluid velocity and L_c a characteristic length of the problem. From (3.12a) it can be seen that if $\text{Re} \ll 1$ the right hand side of (3.12a) dominates and one can neglect the inertia term on the left hand side. A flow like this, where the viscous term dominates, is called a Stokes or creeping flow and (3.12) reduces to the so called Stokes equations. Such an introduction of dimensionless parameters, like it is commonly done in the Newtonian case, is generally a very complicated task for non-Newtonian fluids and there is no guarantee that one can find such a scaling [76, 77]. In literature one can find expressions for the Reynolds number in a pipe flow of generalized Newtonian fluids [78–80]. Nevertheless, even for relatively simple constitutive equations like the Carreau model (2.17) the expressions for the Reynolds number become bewilderingly complicated [80]. Therefore, only the Newtonian and power law regime of the Carreau model (2.17) are considered in the computation of the Reynolds number. The Reynolds number for the flow of a power law fluid (2.16) around a sphere is given by [81–83]

$$\text{Re}_{\text{PL}} = \frac{\rho U^{1-n} d^{n+1}}{K}. \quad (3.13)$$

In the definition of Re_{PL} the parameter K is the consistency index and can be determined for a Carreau fluid (2.17) when $\lambda\dot{\gamma} \gg 1$ as $K = \eta_0 \lambda^n$. Further, d is the particle diameter and U the characteristic velocity. The velocity U can be determined in a shear flow with shear rate $\dot{\gamma}_0$ as $\dot{\gamma}_0 = 2U/d$ [81]. Using this relation and the expression for K given above, (3.13) can be rewritten as

$$\text{Re}_{\text{PL}} = \frac{2^{n-1} \rho d^2}{\eta_0 \lambda^n} \dot{\gamma}^{1-n}. \quad (3.14)$$

For a Newtonian fluid with $n = 0$ the above definition corresponds to the one given by Lin et al. [84].

It can be shown that the Reynolds number for filled polymers is often small and, hence, one can neglect inertia of the fluid. For that let us consider typical values of the parameters in (3.14). The

3. Computational fluid dynamics simulations of suspensions

characteristic length scale, that is the particle diameter, is of the order $d \sim 10^{-6}$ m, the density of the fluid is of the order $\rho \sim 10^3$ kg m $^{-3}$. The polymer is characterized by its zero shear viscosity of the order $\eta_0 \sim 10^{(1\dots3)}$ Pa s or even higher and its characteristic time $\lambda \sim 10^{(-3\dots-2)}$ s, compare with figure 1.2. The flow index n takes commonly values between 0 and -1 . Using these factors for the material and geometry parameters one obtains that the shear rate has to be smaller than

$$\dot{\gamma} \lesssim 10^{\frac{\eta'_0 + \lambda' n + 9}{1-n}} \text{ s}^{-1} \quad (3.15)$$

where $\eta'_0 = 1 \dots 3$ and $\lambda' = -3 \dots -2$ are the respective powers to η_0 and λ and $n = -1 \dots 0$. This gives in the worst case, $\eta'_0 = 1$, $\lambda' = -2$, $n = -1$, a value for the shear rate of $\dot{\gamma}_0 \sim 10^6$ s $^{-1}$ to fulfill the creeping motion equations. Considering common shear rates in processing procedures and experiments, up to $\dot{\gamma} \sim 10^5$ s $^{-1}$ (compare with figures 1.2 and 2.2), it is reasonable to assume that the viscous forces dominate and the left hand side of (3.10a) can be set to zero. Thus, the fluid behavior can be described by the non-linear Stokes equations

$$\text{div}(\boldsymbol{\sigma}(\mathbf{u})) - \text{grad}(p) = 0 \quad (3.16a)$$

$$\text{div}(\mathbf{u}) = 0. \quad (3.16b)$$

The dependence of the viscosity on the velocity is given in the present PhD thesis by the Carreau model (2.17). The non-linear system of equations (3.16) is solved using a standard Galerkin method in a velocity-pressure formulation [85, 86]. For that (3.16) is multiplied by the test functions $\tilde{\mathbf{u}}$ and \tilde{p} and integrated by parts over the domain Ω with the boundary $\partial\Omega$. This gives the weak form of the problem as

find $(\mathbf{u}, p) \in \mathcal{M}$ such that:

$$\int_{\Omega} \boldsymbol{\sigma}(\mathbf{u}) : \mathbf{d}(\tilde{\mathbf{u}}) - p \text{div}(\tilde{\mathbf{u}}) \, d\Omega - \int_{\partial\Omega} \tilde{\mathbf{u}} \cdot [\boldsymbol{\sigma}(\mathbf{u}) - p\mathbf{1}] \cdot \mathbf{n} \, d\Gamma = 0 \quad \forall \tilde{\mathbf{u}} \in \mathcal{U} \quad (3.17a)$$

$$- \int_{\Omega} \tilde{p} \text{div}(\mathbf{u}) \, d\Omega = 0 \quad \forall \tilde{p} \in \mathcal{P} \quad (3.17b)$$

with $(\tilde{\mathbf{u}}, \tilde{p}) \in \mathcal{M}$ and $\mathcal{M} = \mathcal{U} \times \mathcal{P}$. The function spaces are given by $\mathcal{U} \in [H^1(\Omega)]^{d_s}$ and $\mathcal{P} \in L^2(\Omega)$, with d_s the spatial dimension. $H^1(\Omega)$ is the Hilbert space and $L^2(\Omega)$ is the space of square integrable functions [85, 86]. For a numerically stable discretization a suitable choice of basis functions for the finite elements is needed. A commonly used choice, that is also used here, is the so called Taylor-Hood element [87]. The Taylor-Hood element is recommended by Boffi et al. [87] for three dimensional problems. In the Taylor-Hood element the basis functions are

3. Computational fluid dynamics simulations of suspensions

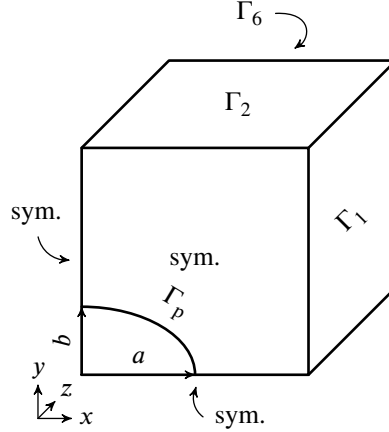


Figure 3.3.: Sketch of the boundaries for 1/8 of the RVE.

gives as follows: for the velocity piecewise continuous quadratic Lagrange polynomials and for the pressure piecewise continuous linear Lagrange polynomials (P2P1). Equation (3.17) is implemented using the finite element library *FEniCS/Dolfin* [88–91]. The non-linear system of equations resulting from the discretization of (3.17) is solved using a Newton–Raphson scheme. In each Newton iteration the direct sparse solver *MUMPS* [92, 93] is used through the *PETSc* library [94–96].

Since only the gradient of the pressure enters in (3.16) it is generally only determined up to a constant. To fix the pressure level a common approach is to force the average pressure in the volume to be zero [86]

$$\frac{1}{|\Omega|} \int_{\Omega} p \, d\Omega = 0. \quad (3.18)$$

Here $|\Omega|$ is the volume of the domain in three spatial dimensions, $|\Omega| = \int_{\Omega} 1 \, d\Omega$.

3.3.2. Boundary conditions for a fixed particle

Figure 3.3 shows a sketch of the RVE when symmetry is exploited. The domain is then given as $\Omega = [0, \frac{L}{2}]^3$. On the boundaries in the symmetry planes the velocity normal to the plane is zero. A no-slip condition is applied on the particle surface Γ_p , that is $\mathbf{u} = \mathbf{0}$ on Γ_p . A traction free condition is applied at the boundary Γ_2 : $(\boldsymbol{\sigma} - p\mathbf{1}) \cdot \mathbf{n} = \mathbf{0}$ on Γ_2 . The conditions on the boundaries Γ_1 and Γ_6 are discussed in the respective chapters where the simulation results are presented.

3.4. Moving particle in a shear flow

3.4.1. Problem description

In case of a moving particle the mathematical description of the problem becomes more involved. Hu et al. [97] showed that it is superior to use a strong coupling of the governing equations by setting up a weak momentum balance for the whole suspension instead of an iterative coupling. In the iterative coupling one would first solve the fluid problem assuming that the particles are fixed and compute with the solution of the flow field the forces and torques exerted by the fluid onto the particle. Knowing the forces and torques one would update the particle translational and angular velocities and solve again the fluid problem assuming that the particles move with the previously computed velocities. This procedure is then repeated over and over, until convergence is reached. While the iterative coupling is essentially easier to implement, since one can use a standard solver for the flow problem, its biggest problem is that the particles will always start an oscillatory movement with the amplitude increasing to infinity [97]. Thus, the iterative coupling is unstable and is not a feasible method to simulate a moving particle.

Figure 3.4 shows a sketch of the fluid domain with one immersed particle. In the following only one particle is considered since this is sufficient for the purpose of this work. The particle in figure 3.4 is described by its mass m_p , moment of inertia tensor \mathbf{I}_p and the position of its center of mass \mathbf{X}_p . The boundary of the particle is denoted by $\partial\Omega_p$ and is assumed to be fully immersed in the fluid. The matrix fluid is described by its density ρ and its viscosity $\eta(\mathbf{u})$ which is again assumed to obey the Carreau law (2.17). The fluid can be described by the previously introduced Cauchy momentum equation for an incompressible fluid (3.10). The motion of the fluid is coupled to the motion of the particle by requiring that the force and torque exerted by the fluid on the particle must be equal to the force and torque exerted by the particle on the fluid. For a rigid particle the translatory motion is given by Newton's second law

$$m_p \frac{d\mathbf{v}_p}{dt} = - \int_{\partial\Omega_p} (\boldsymbol{\sigma} - p\mathbf{1}) \cdot \mathbf{n} \, d\Gamma \quad (3.19)$$

where the integral on the right hand side is to be taken over the surface of the particle. In (3.19) \mathbf{v}_p is the translatory velocity of the particle, $\boldsymbol{\sigma}$ and p are the stress and pressure in the fluid. The unit normal vector \mathbf{n} is pointing into the fluid, see figure 3.4.

3. Computational fluid dynamics simulations of suspensions

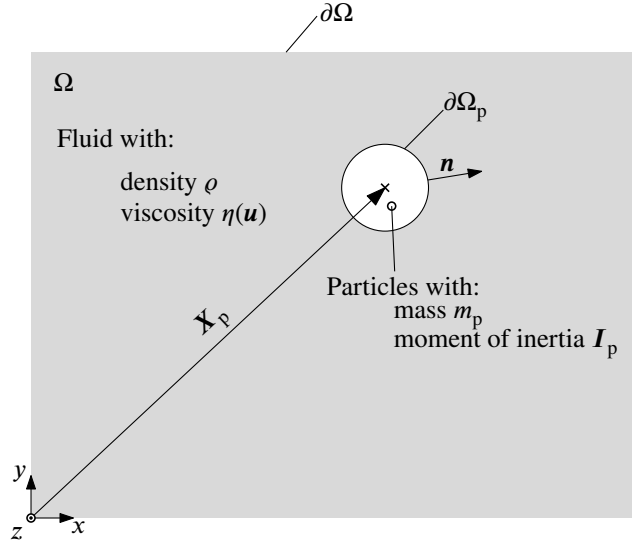


Figure 3.4.: Sketch of a fluid domain with one immersed particle.

Further, the rotational motion is governed by Euler's equation

$$\frac{d}{dt} (I_p \boldsymbol{\omega}_p) = - \int_{\partial\Omega_p} (\mathbf{x} - \mathbf{X}_p) \times ((\boldsymbol{\sigma} - p\mathbf{1}) \cdot \mathbf{n}) d\Gamma \quad (3.20)$$

here $\boldsymbol{\omega}_p$ is the angular velocity of the particle and \mathbf{x} is the spatial coordinate. The integral on the right hand side of (3.20) is again to be taken over the surface of the particle. Finally a no-slip condition between the fluid and the particle is assumed

$$\mathbf{u} - (\mathbf{v}_p + \boldsymbol{\omega}_p \times (\mathbf{x} - \mathbf{X}_p)) = 0 \quad \text{on } \partial\Omega_p. \quad (3.21)$$

The particle position can be computed by

$$\frac{d\mathbf{X}_p}{dt} = \mathbf{v}_p \quad \text{with} \quad \mathbf{X}_p|_{t=0} = \mathbf{X}_{p,0} \quad (3.22)$$

and its rotation angle $\boldsymbol{\theta}_p$ by

$$\frac{d\boldsymbol{\theta}_p}{dt} = \boldsymbol{\omega}_p \quad \text{with} \quad \boldsymbol{\theta}_p|_{t=0} = \boldsymbol{\theta}_{p,0} \quad (3.23)$$

where $\mathbf{X}_{p,0}$ and $\boldsymbol{\theta}_{p,0}$ are the initial position and orientation of the particle.

Equations (3.10) and (3.19) to (3.23) fully describe the suspension. To solve the equations using the finite element method it is necessary to convert them into a weak form. The weak form

3. Computational fluid dynamics simulations of suspensions

of the Cauchy momentum equation for an incompressible fluid (3.10) is obtained by multiplying with the test functions for the velocity $\tilde{\mathbf{u}}$ and pressure \tilde{p} and integrating by parts. This yields

$$\int_{\Omega} \rho \left(\frac{\partial \mathbf{u}}{\partial t} + \mathbf{u} \cdot \text{grad}(\mathbf{u}) \right) \cdot \tilde{\mathbf{u}} \, d\Omega + \int_{\Omega} \left[\boldsymbol{\sigma}(\mathbf{u}) : \mathbf{d}(\tilde{\mathbf{u}}) - p \, \text{div}(\tilde{\mathbf{u}}) - \tilde{p} \, \text{div}(\mathbf{u}) \right] \, d\Omega - \int_{\partial\Omega} \tilde{\mathbf{u}} \cdot (\boldsymbol{\sigma}(\mathbf{u}) - p\mathbf{1}) \cdot \mathbf{n} \, d\Gamma - \int_{\partial\Omega_p} \tilde{\mathbf{u}} \cdot (\boldsymbol{\sigma}(\mathbf{u}) - p\mathbf{1}) \cdot \mathbf{n} \, d\Gamma = 0. \quad (3.24)$$

The two last terms in the above equation are the boundary terms over the outer boundary of the fluid $\partial\Omega$ and the particle boundary $\partial\Omega_p$. The integral over the particle surface gives the force and torque exerted by the fluid on the particle. This integral can be rewritten using equations (3.19) and (3.20) as [97]

$$- \int_{\partial\Omega_p} \tilde{\mathbf{u}} \cdot (\boldsymbol{\sigma}(\mathbf{u}) - p\mathbf{1}) \cdot \mathbf{n} \, d\Gamma = - \int_{\partial\Omega_p} \left[\tilde{\mathbf{v}}_p + \tilde{\boldsymbol{\omega}}_p \times (\mathbf{x} - \mathbf{X}_p) \right] \cdot ((\boldsymbol{\sigma}(\mathbf{u}) - p\mathbf{1}) \cdot \mathbf{n}) \, d\Gamma \quad (3.25a)$$

$$= \tilde{\mathbf{v}}_p \cdot m_p \frac{d\mathbf{v}_p}{dt} + \tilde{\boldsymbol{\omega}}_p \cdot \frac{d}{dt} (\mathbf{I}_p \boldsymbol{\omega}_p) \quad (3.25b)$$

where $\tilde{\mathbf{v}}_p$ and $\tilde{\boldsymbol{\omega}}_p$ are the test functions for the particle translatory and angular velocities respectively. The introduction of (3.25) requires that the test functions and the solutions on the particle surface are equal [97]. This equality of the test functions and solutions is achieved by enforcing the no-slip condition (3.21) using a Lagrange multiplier λ_p on the particle surface [42]

$$\int_{\partial\Omega_p} \left[(\tilde{\mathbf{u}} - (\tilde{\mathbf{v}}_p + \tilde{\boldsymbol{\omega}}_p \times (\mathbf{x} - \mathbf{X}_p))) \cdot \lambda_p \right] + \left[\tilde{\lambda}_p \cdot (\mathbf{u} - (\mathbf{v}_p + \boldsymbol{\omega}_p \times (\mathbf{x} - \mathbf{X}_p))) \right] \, d\Gamma = 0 \quad (3.26)$$

with $\tilde{\lambda}_p$ being the test function for the Lagrange multiplier. Equations (3.24), (3.25b) and (3.26) give the complete weak momentum balance of the suspension. A nice property of this formulation is that one obtains the fluid velocity and pressure as well as the particle velocities in one solution step, thus there is no need for an iterative procedure.

As already shown in the previous section, it is generally reasonable to assume that the inertia of the fluid can be neglected in filled polymer melts. If one additionally assumes that the particles are force free [98], that is the net force and torque acting on the particle is zero, the weak form for the suspension simplifies significantly. The weak form for a suspension of force free rigid particles reads

3. Computational fluid dynamics simulations of suspensions

find $(\mathbf{u}, p, \mathbf{v}_p, \boldsymbol{\omega}_p, \lambda_p) \in \mathcal{N}$ such that:

$$\int_{\Omega} \boldsymbol{\sigma}(\mathbf{u}) : \mathbf{d}(\tilde{\mathbf{u}}) - p \operatorname{div}(\tilde{\mathbf{u}}) \, d\Omega - \int_{\partial\Omega} \tilde{\mathbf{u}} \cdot [\boldsymbol{\sigma}(\mathbf{u}) - p\mathbf{1}] \cdot \mathbf{n} \, d\Gamma = 0 \quad (3.27a)$$

$$- \int_{\Omega} \tilde{p} \operatorname{div}(\mathbf{u}) \, d\Omega = 0 \quad (3.27b)$$

$$\int_{\partial\Omega_p} \tilde{\lambda}_p \cdot (\mathbf{u} - (\mathbf{v}_p + \boldsymbol{\omega}_p \times (\mathbf{x} - \mathbf{X}_p))) \, d\Gamma = 0 \quad (3.27c)$$

$$\int_{\partial\Omega_p} (\tilde{\mathbf{u}} - (\tilde{\mathbf{v}}_p + \tilde{\boldsymbol{\omega}}_p \times (\mathbf{x} - \mathbf{X}_p))) \cdot \lambda_p \, d\Gamma = 0 \quad (3.27d)$$

for all $(\tilde{\mathbf{u}}, \tilde{p}, \tilde{\mathbf{v}}_p, \tilde{\boldsymbol{\omega}}_p, \tilde{\lambda}_p) \in \mathcal{N}$ and $\mathcal{N} = \mathcal{U} \times \mathcal{P} \times \mathcal{V} \times \mathcal{W} \times \mathcal{L}$. The first two equations above are the already introduced weak form of the non-linear Stokes equations (3.17). The function spaces are given by $\mathcal{U} \in [H^1(\Omega)]^{d_s}$ and $\mathcal{P} \in L^2(\Omega)$ with d_s being the spatial dimension, as in the previous section. The function spaces for the particle velocities are given by $\mathcal{V} \in \mathcal{R}^{d_s}$ and $\mathcal{W} \in \mathcal{R}^{d_s}$, here \mathcal{R} is the space of real numbers. The space for the Lagrange multiplier is only defined on the particle surface as $\mathcal{L} \in [L^2(\partial\Omega_p)]^{d_s}$. For the discretization of the velocity and pressure the Taylor-Hood element is again used. The Lagrange multiplier λ_p is discretized using continuous piecewise linear Lagrange polynomials. The particle velocities are introduced as real degrees of freedom. Equation (3.27) is again implemented using the finite element library *FEniCS/Dolfin* [88–91]. The non-linear system of equations arising from discretizing of (3.27) is solved using a Newton–Raphson scheme where in each iteration the direct sparse solver *MUMPS* [92, 93] is used through the *PETSc* library [94–96].

If the constitutive relation for the stress tensor is time independent, as it is for a generalized Newtonian fluid, equations (3.27) are independent of the time t . This means that in a force free suspension the stress only depends on the current position and orientation of the particle. In other words, the history of how the particle moved through the fluid in time has no influence on the solution. This property of (3.27) allows to solve for a specific particle position and orientation immediately. Thus it is not necessary to move the particle according to (3.22) and (3.23), it is sufficient to place the particle at the position of interest with the corresponding particle orientation and solve (3.27).

3.4.2. Boundary conditions for a moving particle

Figure 3.5 shows a sketch of the domain when symmetry is exploited, as discussed in the introduction of this chapter. The domain is then given as $\Omega = [-\frac{L}{2}, \frac{L}{2}; -\frac{L}{2}, \frac{L}{2}; 0, \frac{L}{2}]$. On the

3. Computational fluid dynamics simulations of suspensions

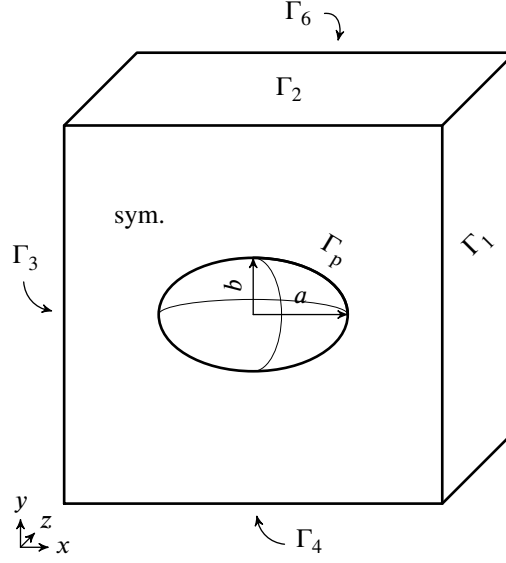


Figure 3.5.: Sketch of the boundaries for 1/2 of the RVE.

boundary in the symmetry plane the velocity normal to the plane is zero. On the particle surface Γ_p a no-slip condition is weakly enforced by (3.27c) and (3.27d). At the boundaries $\Gamma_1, \Gamma_2, \Gamma_3, \Gamma_4$ and Γ_6 the velocity according to (3.6) is applied with \mathbf{d} and \mathbf{w} given by (3.5).

3.5. Computation of effective macroscopic properties

3.5.1. Introduction

To obtain the effective properties of the suspension it is necessary to compute the average power density or the average stress tensor. The average power density is given by

$$\langle P \rangle = \langle \boldsymbol{\sigma} : \mathbf{d} \rangle = \frac{1}{|\Omega|} \int_{\Omega} \boldsymbol{\sigma} : \mathbf{d} \, d\Omega \quad (3.28)$$

where $\boldsymbol{\sigma}$ is the local stress tensor and \mathbf{d} is the local rate of strain tensor. The pressure does not contribute to the power density for an incompressible fluid, since

$$p\mathbf{1} : \mathbf{d} = p \operatorname{tr}(\mathbf{d}) = 0. \quad (3.29)$$

The average stress tensor can be computed as shown by Batchelor [98]

$$\langle \boldsymbol{\sigma} \rangle = \boldsymbol{\sigma}_0 + \boldsymbol{\sigma}_p \quad (3.30)$$

3. Computational fluid dynamics simulations of suspensions

where $\boldsymbol{\sigma}_0$ is the matrix stress without the presence of any particle and $\boldsymbol{\sigma}_p$ is the contribution of the particle to the stress tensor, which can be computed as

$$\boldsymbol{\sigma}_p = \frac{1}{|\Omega|} \int_{\Gamma_p} (\boldsymbol{\sigma} - p\mathbf{1}) \cdot \mathbf{n} \mathbf{x} \, d\Gamma. \quad (3.31)$$

Γ_p is the surface of the particle with the outward normal \mathbf{n} at position \mathbf{x} . The particle contribution to the stress $\boldsymbol{\sigma}_p$ is also referred to as *stresslet* [98]. The average power density $\langle P \rangle$ from (3.28) can also be expressed using the average stress tensor by employing the Hill-Mandel lemma [99–103]

$$\langle P \rangle = \langle \boldsymbol{\sigma} : \mathbf{d} \rangle = \langle \boldsymbol{\sigma} \rangle : \langle \mathbf{d} \rangle. \quad (3.32)$$

If the velocity \mathbf{u}_0 is prescribed on the complete outer boundary $\partial\Omega$ of the RVE, the average rate of strain tensor is equal to the applied rate of strain tensor as

$$\langle \mathbf{d} \rangle = \frac{1}{|\Omega|} \int_{\Omega} \frac{1}{2} (\text{grad}(\mathbf{u}) + \text{grad}(\mathbf{u})^\top) \, d\Omega \quad (3.33a)$$

$$= \frac{1}{2|\Omega|} \int_{\partial\Omega} \mathbf{n} \mathbf{u}_0 + \mathbf{u}_0 \mathbf{n} \, d\Gamma \quad (3.33b)$$

$$= \mathbf{d}_0. \quad (3.33c)$$

Here the Gauss theorem has been used to transform the volume integral into a surface integral.

3.5.2. Computing the intrinsic viscosity

The intrinsic viscosity can be computed using (3.28). For this a homogeneous equivalent fluid with viscosity $\eta^{(\text{hom})}$ that is subjected to the same macroscopic rate-of-strain tensor \mathbf{d}_0 on its boundary is introduced. Thus, for the homogeneous equivalent material the average power density is given by

$$\langle P \rangle^{(\text{hom})} = \frac{1}{|\Omega|} \int_{\Omega} 2\eta^{(\text{hom})} \mathbf{d}_0 : \mathbf{d}_0 \, d\Omega = 2\eta^{(\text{hom})} \langle \mathbf{d}_0 : \mathbf{d}_0 \rangle \quad (3.34)$$

where the right hand side results from the assumption that the macroscopic viscosity is not spatially varying.

To determine the value of $\eta^{(\text{hom})}$, the power density in the filled system and the homogeneous equivalent material are compared:

$$\langle P \rangle^{(\text{hom})} = \langle P \rangle. \quad (3.35)$$

This comparison is schematically sketched in figure 3.6. The particles are smeared out in the

3. Computational fluid dynamics simulations of suspensions

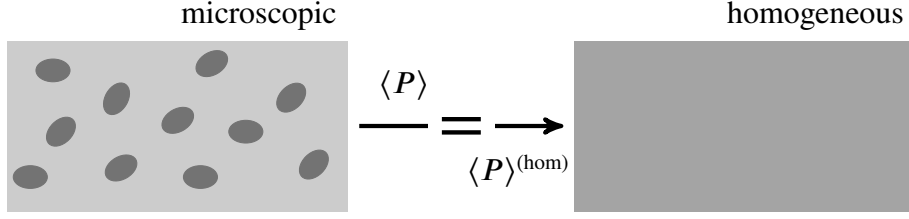


Figure 3.6.: Schematic sketch of the comparison on power density in the suspension.

homogeneous equivalent fluid. Using the equality of power density and (3.34) the viscosity of the homogeneous equivalent material can be expressed as

$$\eta^{(\text{hom})} = \frac{\langle P \rangle}{2\langle \mathbf{d}_0 : \mathbf{d}_0 \rangle}. \quad (3.36)$$

The intrinsic viscosity introduced in section 2.1 can be computed from (2.4) and (3.36) as

$$[\eta] = \frac{\eta^{(\text{hom})} - \eta}{\eta\varphi} \quad (3.37)$$

where η is the matrix viscosity at the same applied rate of strain tensor \mathbf{d}_0 . Since formally the intrinsic viscosity is only defined in the limit, when the volume fraction of particles goes to zero, it is necessary to check that the intrinsic viscosity computed numerically using (3.37) is independent of φ .

Equation (3.34) can be further simplified by assuming that \mathbf{d}_0 is applied on the complete outer boundary of the box, in this case

$$\langle P \rangle^{(\text{hom})} = 2\eta^{(\text{hom})} \mathbf{d}_0 : \mathbf{d}_0. \quad (3.38)$$

It turns out that this relation is also true for many symmetric flows around particles, where \mathbf{d}_0 is only applied on parts of the boundary. If (3.38) is fulfilled can be easily checked in numerical simulations by computing the average rate-of-strain tensor $\langle \mathbf{d} \rangle$. For (3.38) to be fulfilled the relation

$$\langle \mathbf{d} \rangle = \mathbf{d}_0 \quad (3.39)$$

must hold, see (3.33).

Numerical experiments have been carried out to check whether the volume average or the stresslet is numerically more feasible. For this Einstein's equation (2.1) was computed using Newtonian fluids. It turned out that computing the intrinsic viscosity using the volume average

3. Computational fluid dynamics simulations of suspensions

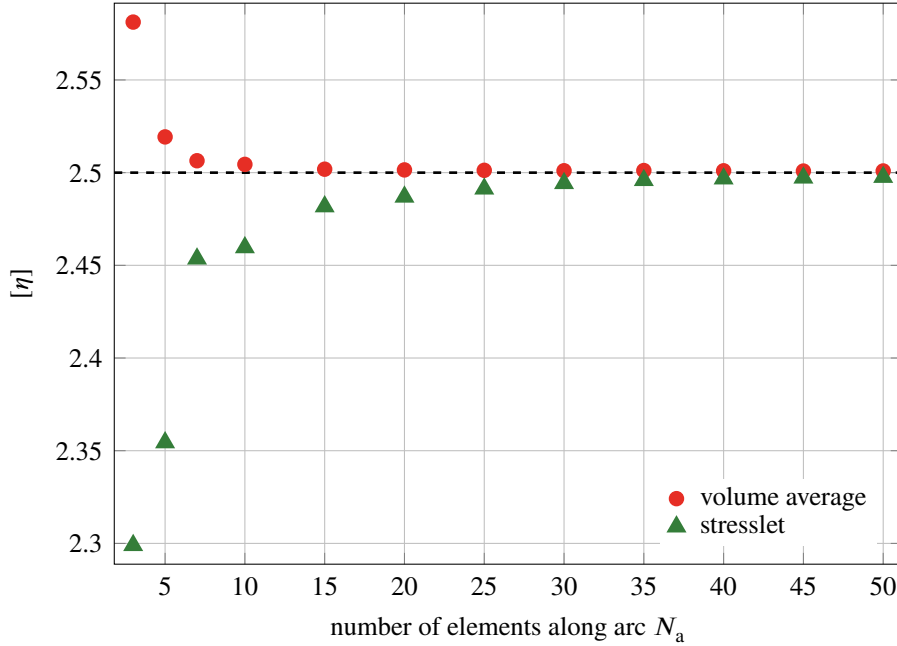


Figure 3.7.: Comparison of the intrinsic viscosity $[\eta]$ for a Newtonian fluid using the volume average (3.28) and the stresslet (3.31). The dashed line indicates the analytical solution.

(3.28) required a coarser mesh at the particle surface than using the surface integral (3.31) to achieve the same accuracy. For this the average power density has been computed directly using (3.28) and using the Hill-Madel lemma (3.32). For the simulations a sphere was placed in the stagnation point of a uniaxial elongational flow and the velocity and pressure fields have been resolved using the method described in section 3.3. At the boundaries Γ_1 and Γ_6 defined in section 3.3.2 the velocity has been prescribed according to (3.2). The rate of strain tensor is given by (3.1) with $\dot{\epsilon}_1 = 1 \text{ s}^{-1}$ and $\dot{\epsilon}_2 = -0.5 \text{ s}^{-1}$. The intrinsic viscosity has been computed using (3.36) where $\langle P \rangle$ has been computed either using the 1st approach with the direct volume averaging (3.28) or using the 2nd approach with the stresslet (3.31). The meshes have been generated in such a way that the number of elements along an outer edge of the RVE has been set to 5 and the number of elements along the arc of the spherical particles has been varied. The number of elements along the arc is referred to as N_a . The results for the intrinsic viscosity are shown in figure 3.7, where the dashed line indicates the analytical result for the intrinsic viscosity, $[\eta] = 2.5$. It can be seen that the volume average converges faster to the analytical solution. Therefore the volume average will be used in the following to compute the intrinsic viscosity in order to reduce numerical effort. Figure 3.9 shows exemplarily some of the meshes close to the inclusion used in the above tests.

3. Computational fluid dynamics simulations of suspensions

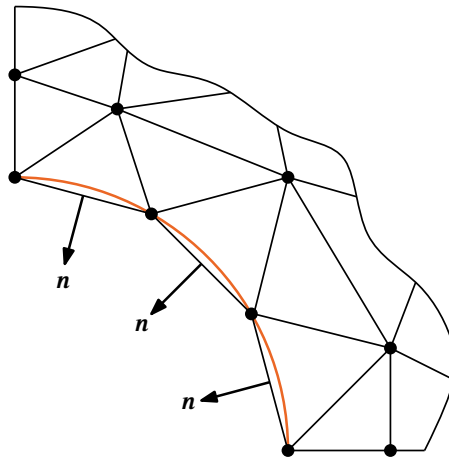


Figure 3.8.: 2d mesh around a quarter circle, the actual circle is drawn in orange. The normal vector “jump” as the mesh consists of straight lines. In the nodes, indicated by the points, the normal vector is not well defined.

The slower convergence of the stresslet can be explained by the fact that in the computation of the stresslet the numerical scheme uses normal vectors which “jump”. Let us consider, for simplicity, the two dimensional case as depicted in figure 3.8. In the figure the part of a two dimensional mesh, composed of triangles around a quarter of a circle, is sketched. The actual circle is drawn in orange. The dots in figure 3.8 are the so called nodes of the mesh. Along the boundary of the circle the normal vectors are drawn and it can be seen that the orientation of these vectors changes “jump”-like from one element to another. In the nodes at the boundary the normal is not well defined, normally the normal at a node is computed by averaging the normals of all the adjacent elements. As the mesh becomes finer the normals are approximated better and better and the stresslet converges to the analytical solution. In three dimensions the problem is essentially the same as in 2d but the boundary is described by flat triangles instead of straight lines.

3.6. Summary

- In this thesis two finite element codes have been implemented utilizing the *FEniCS/Dolfin* libraries. In one code the particle is considered to be fixed, in the other code the particle can freely rotate and translate.
- A finite element scheme is described to solve for a moving particle in a flow field by means of a global weak momentum balance for the suspension.

3. Computational fluid dynamics simulations of suspensions

- In case that the fluid inertia can be neglected and the particles are considered to be force free the stress in the suspension is independent of the flow history. The current stress in the suspension is only described by the current position/orientation of the particles.
- For certain particle orientations and flows symmetries can be exploited to reduce the numerical effort.
- In elongational flows it is possible to place the particle in such a way that it can be considered fixed.
- The average power density in the system can be computed by two means. The first is to directly average the power density. The second method first computes the average stress tensor and uses the Hill-Mandel lemma to compute the average power density.
- In numerical experiments it turned out that the direct average could be done using a coarser mesh. This reduces the numerical effort and hence this method is chosen to compute the intrinsic viscosity in the following chapters.

3. Computational fluid dynamics simulations of suspensions

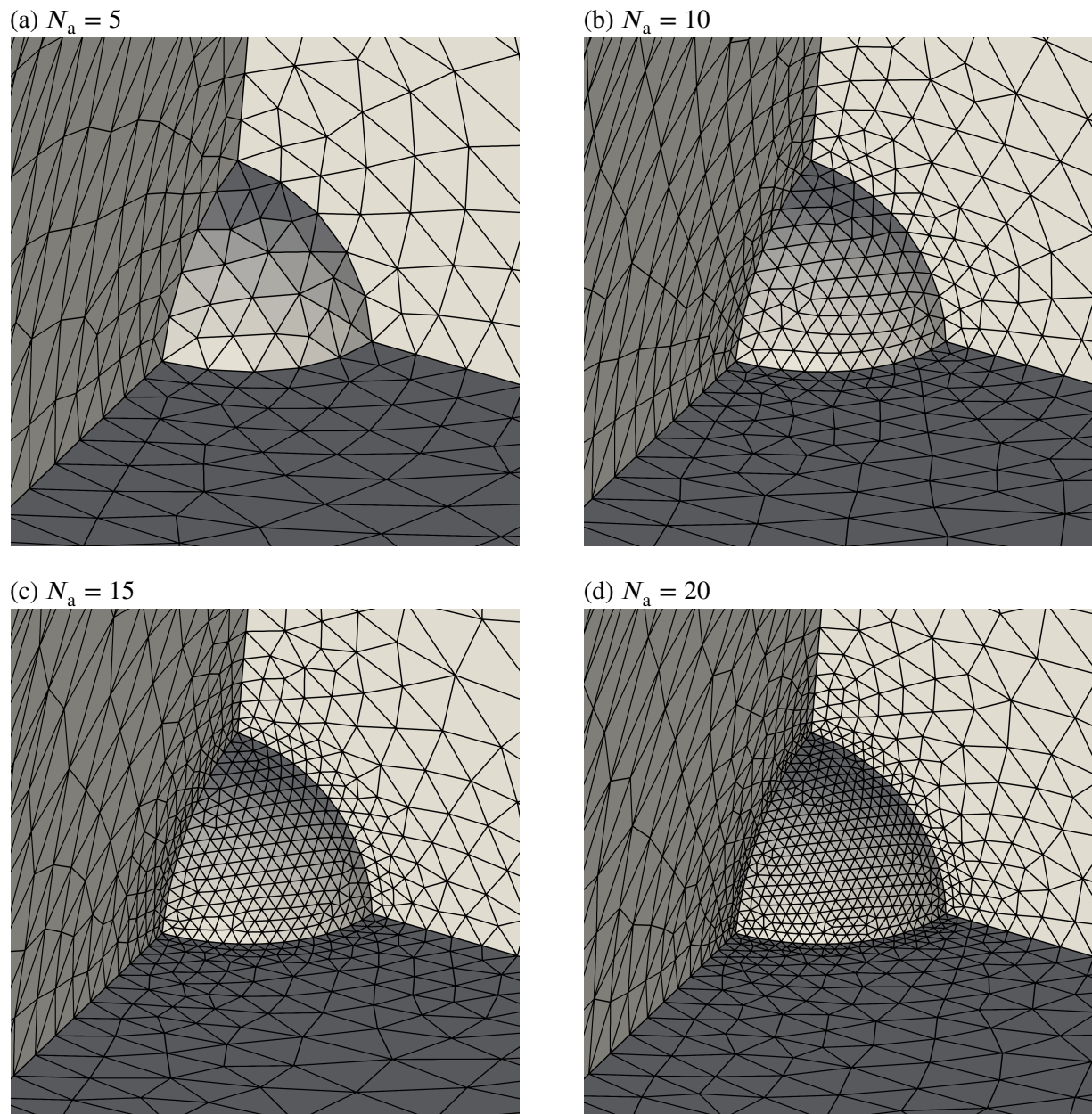


Figure 3.9.: Example meshes for different values of N_a used to check the convergence of volume average and stresslet.

4. Spherical particles

4.1. Introduction

In this chapter a problem quite similar to Einstein's original problem [1] is considered. The only, nevertheless crucial, difference is that, whereas in the calculation of Einstein the matrix fluid was Newtonian, here a non-Newtonian matrix fluid is investigated. The fluid is considered to be shear thinning and is described by the Carreau model (2.17). The effective properties of the dilute suspension of rigid spherical particles are computed as described in chapter 3. In particular, the numerical scheme for the fixed particle is used, for details refer to section 3.3. The geometry of the RVE is that of a cube with edge length $L = 1$ and a spherical hole at its center (at $\mathbf{X}_{\text{RVE}} = (0, 0, 0)^\top$), see section 3.2. The radius of the sphere r is varied as 0.02, 0.03, 0.04, 0.05. Note that the units of L and r are arbitrary: they just have to be the same, e.g. both in millimeter or micrometer. This is possible because in the following only relative values where the units cancel will be considered. The actual volume fraction of the particles is computed by a sum over the volumes of the elements in the mesh. Table 4.1 shows the computed volume fractions for the different radii used. The meshes used in the simulations are described in section 3.2 and have between ~ 12000 and ~ 14000 elements. Figure 4.1 shows exemplarily the mesh for the radius $r = 0.05$. The boundary conditions have mostly been defined already in section 3.3.2. Only the boundary conditions at Γ_1 and Γ_6 need to be specified here, see figure 3.3. At the boundary Γ_6 a traction free condition is applied: $(\boldsymbol{\sigma} - p\mathbf{1}) \cdot \mathbf{n} = \mathbf{0}$ on Γ_6 . On Γ_1 the velocity is prescribed by (3.2) using the macroscopic rate-of-strain tensor of a uniaxial extensional flow along x -direction.

Table 4.1.: Radii and the corresponding computed volume fractions of the particles.

r	φ
0.02	$3.32 \cdot 10^{-5}$
0.03	$1.13 \cdot 10^{-4}$
0.04	$2.67 \cdot 10^{-4}$
0.05	$5.23 \cdot 10^{-4}$

4. Spherical particles

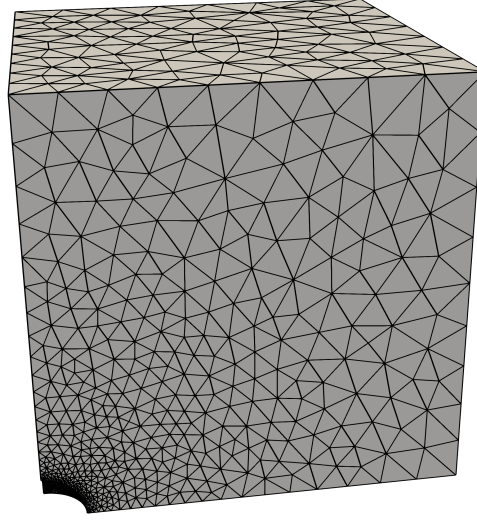


Figure 4.1.: Mesh used for the simulation for the particle with radius $r = 0.05$.

The values for the strain rates in (3.1) are given by $\dot{\epsilon}_1 = d_0$ and $\dot{\epsilon}_2 = -0.5d_0$, thus the applied macroscopic rate-of-strain tensor is:

$$\mathbf{d}_0 = d_0 \begin{pmatrix} 1 & 0 & 0 \\ 0 & -0.5 & 0 \\ 0 & 0 & -0.5 \end{pmatrix}. \quad (4.1)$$

Note, that for the rate-of-strain tensor given by (4.1) the scalar rate-of-strain, according to (2.18), is $\dot{\gamma}_0 = \sqrt{3}d_0$. It is checked that the rate-of-strain tensor averaged over the RVE agrees with a very high accuracy with the applied rate-of-strain tensor (4.1). This means that the computed velocity field complies with equation (4.1) at the boundaries of the RVE, see the end of section 3.5.2.

For the radii given in table 4.1 the intrinsic viscosity $[\eta]$ is computed as described in section 3.5.2. The applied elongation rates are ranging between $d_0 = 10^{-6} \dots 10^6 \text{ s}^{-1}$. The simulations are carried out for a number of thinning exponents in the range of $n = 0$ to $n = -0.9$. For smaller n the numerical solution becomes unstable, because the stress becomes a non-strictly monotonically increasing function [77]. The other material parameters in the Carreau model (2.17) are set to be $\eta_0 = 1 \text{ Pa s}$ and $\lambda = 1 \text{ s}$. The Newton–Raphson scheme needed up to 25 iterations to reach convergence for the smallest value of the thinning exponent, $n = -0.9$.

4.2. Simulation results

Since formally the intrinsic viscosity is only defined in the dilute limit, that is as the volume fraction of particles goes to zero (2.4), it is necessary to verify that the simulations have been carried out in this limit. To check if the dilute limit was reached, it is sufficient to show that the ratio of specific viscosity (2.3) to volume fraction is independent of the volume fraction. Figure 4.2 shows the ratio of the specific viscosity η_{sp} to the volume fraction φ versus the Carreau number $\dot{\gamma}_0\lambda$ for all the simulated radii and a thinning exponent of $n = -0.5$. In the figure it can be seen that all curves fall together, hence the simulations were done in the dilute limit. For the other thinning exponents studied in this thesis similar results are obtained and therefore not shown here.

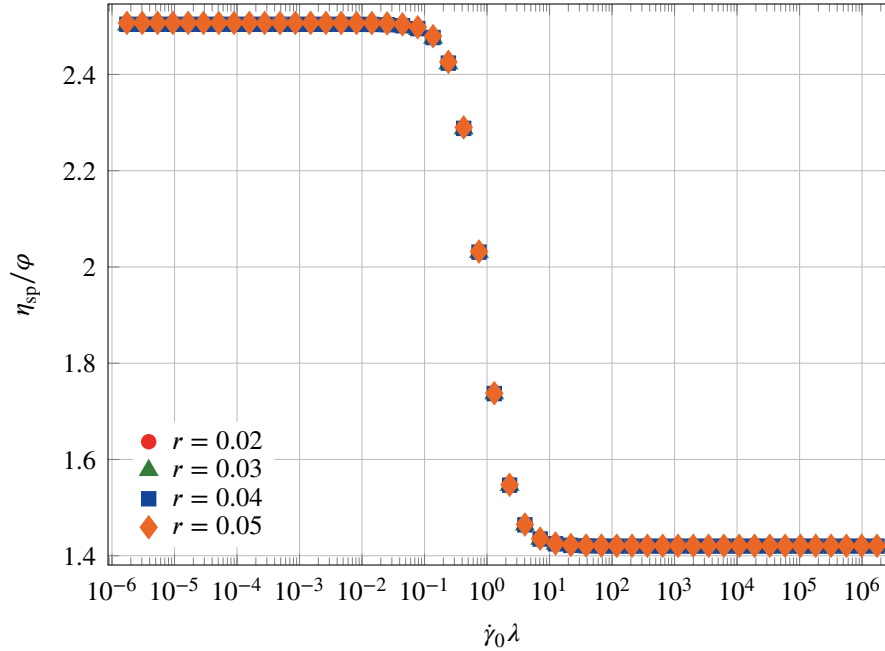


Figure 4.2.: Dependence of η_{sp}/φ on the Carreau number and the particle radius. The thinning exponent is $n = -0.5$.

The obtained intrinsic viscosities for all the simulated thinning exponents are shown in figure 4.3. For small values of the scalar deformation rate, i.e. in the linear regime, Einstein's result for the intrinsic viscosity of spherical particles $[\eta] = 2.50$ is reproduced for all n ; exact with at least 3 digits. This demonstrates the correctness and accuracy of the numerical simulations as well as of the homogenization procedure used in this work. At higher scalar deformation rates the intrinsic viscosity is found to decrease monotonically, finally attaining a plateau, the value of which depends on the thinning exponent n . Note that this lower plateau corresponds to the

4. Spherical particles

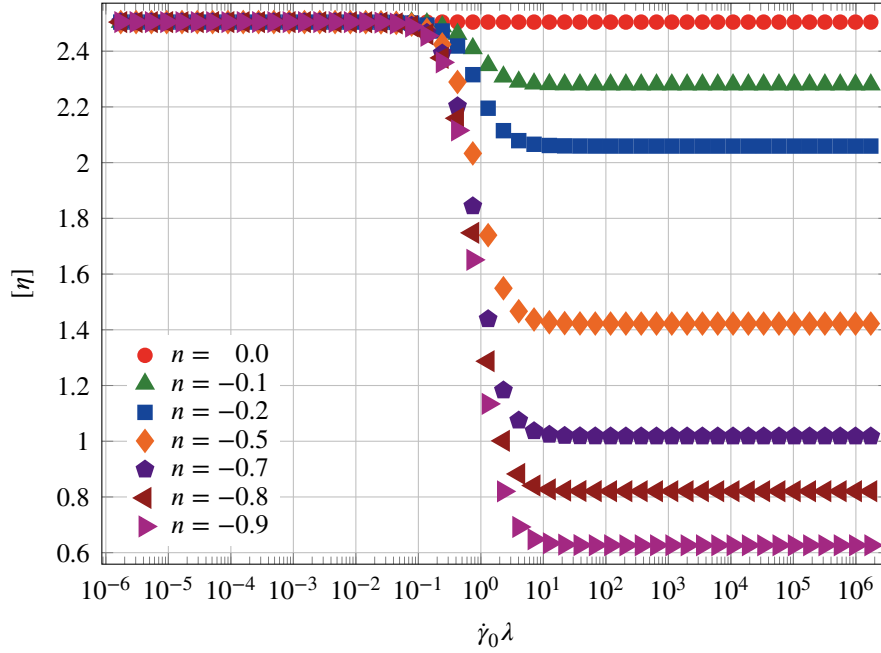


Figure 4.3.: Dependence of $[\eta]$ on the Carreau number $\dot{\gamma}_0\lambda$ for different thinning exponents.

power law thinning region of the rate dependent matrix viscosity: $\eta \sim \dot{\gamma}^n$. To understand the appearance of these three regions, seen as plateau-crossover-plateau in Fig. 4.3, let us consider Fig. 4.4. The figure depicts the flow curve for the Carreau model and exemplarily three applied deformation rates: $\dot{\gamma}_0^{(1)}$, $\dot{\gamma}_0^{(2)}$ and $\dot{\gamma}_0^{(3)}$. If a particle is present in the fluid it will disturb the otherwise homogeneous flow field and there will be a range of local deformation rates around the applied one, as depicted by the shaded regions in Fig. 4.4. For the first applied deformation rate $\dot{\gamma}_0^{(1)}$ the range of local deformation rates is always in the linear regime of the flow curve and one observes the first higher plateau in the intrinsic viscosity. For the second applied deformation rate $\dot{\gamma}_0^{(2)}$ the local deformation rates around the particle are in the crossover regime of the flow curve and correspondingly a crossover in the intrinsic viscosity is observed. For the last deformation rate $\dot{\gamma}_0^{(3)}$ the local deformation rates are completely in the non-linear regime. Here the flow curve has a constant slope n and the second lower plateau in the intrinsic viscosity is seen.

Figure 4.5 shows a plot of the values of intrinsic viscosity obtained by the CFD simulations at high values of the effective deformation rate as a function of the thinning exponent n . Here an infinity symbol as subscript is used to indicate the intrinsic viscosities at high deformation rates: $[\eta](\dot{\gamma}) = [\eta]_\infty$ if $\dot{\gamma}\lambda \gg 1$. Figure 4.5 also shows two predictions found in literature for the intrinsic viscosity in the power law regime [34, 35] as discussed already in section 2.1.2 and a Taylor expansion that has been computed in this study based on the results of the simulations.

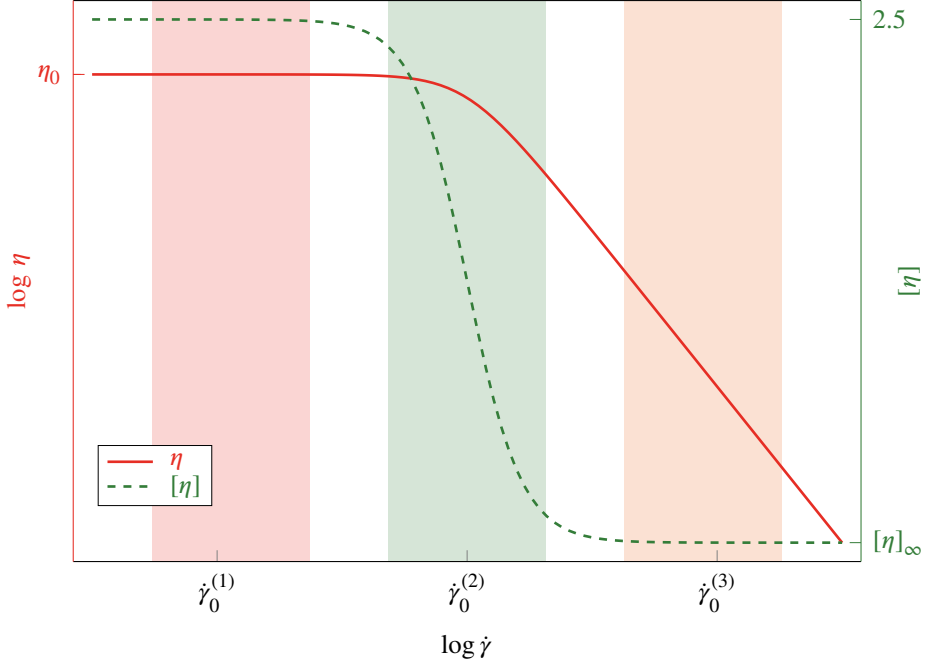


Figure 4.4.: Sketch of the different regions in the Carreau model (2.17) and their corresponding intrinsic viscosities after homogenization.

The discussion starts with the two aforementioned literature predictions.

The linear relation given by Chateau et al. [34] (2.32) does not fit to the simulation results (Figure 4.5, green dash-dotted line). Yet it predicts the two special cases exactly, that is: (i) $[\eta]_\infty(n = 0) = 2.5$ which is just Einstein's result for the Newtonian fluid and (ii) $[\eta]_\infty(n = -2) = -1$ which is an exact result in the limit of high shear rates, as will be shown below. For example the Wagner model [104] for a polymer melt has a slope of $n = -2$.

The other dependence of the high shear rate intrinsic viscosity on the thinning exponent is given by Tanner et al. [35] (2.34). Tanner's fit seems to coincide with the simulation results very well but it does not predict the special case at $n = -2$ (Figure 4.5, blue dashed line).

4.3. Taylor expansion

The already mentioned special case at $n = -2$ can be obtained by a direct comparison of macroscopic and microscopic power density as shown below. At high effective rates, $\lambda\dot{\gamma} \gg 1$, the average power density in the RVE with volume V is given by:

$$\langle P \rangle = \frac{1}{V} \int_V \eta(\dot{\gamma}) \mathbf{d} : \mathbf{d} \, dV = \frac{1}{V} \int_{V-V_p} \eta_0 \lambda^n \dot{\gamma}^{2+n} \, dV. \quad (4.2)$$

4. Spherical particles

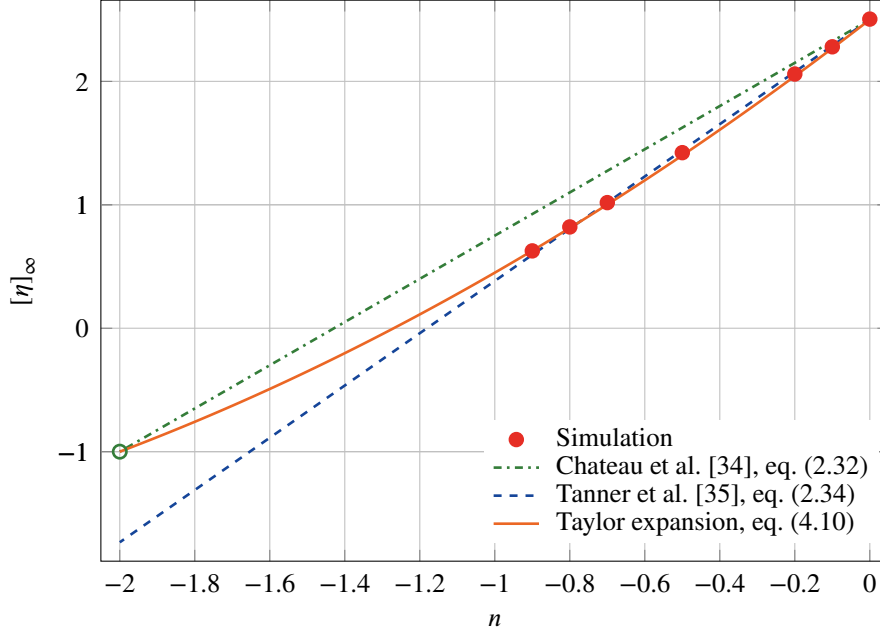


Figure 4.5.: Dependence of $[\eta]$ on the thinning exponent n at high values of the scalar deformation rate, i.e. in the region of lower plateau. The exact analytical result $[\eta]_{\infty} = -1$ for the special case $n = -2$ is marked by the green circle. It can be seen that the Taylor expansion and the prediction of Chateau et al. have the correct limit at $n = -2$, while the prediction of Tanner et al. fails to reproduce this exact analytical result.

Here, when taking the average over all positions \mathbf{x} in the volume V , the fact that there is no energy dissipation inside a rigid sphere with a volume V_p was used. According to the homogenization approach, the average power density in the microscopic RVE should be equal to the power $\langle P \rangle^{(\text{hom})}$ in the equivalent macroscopic media [101]. To calculate the latter, it is assumed that the effective viscosity of dilute suspension is described by the same Carreau model as the matrix viscosity:

$$\eta^{(\text{hom})}(\dot{\gamma}_0) = \eta_0^{(\text{hom})} \left(1 + (\lambda^{(\text{hom})} \dot{\gamma}_0)^2 \right)^{\frac{n}{2}}, \quad (4.3)$$

where $\eta_0^{(\text{hom})}$ is the viscosity of a suspension in the zero deformation rate limit, $\lambda^{(\text{hom})}$ is the characteristic relaxation time of the suspension and $\dot{\gamma}_0$ is the applied deformation rate. The experimental results of Poslinski et al. [31] presented in Section 4.6 demonstrate that this is a reasonable assumption at least up to $\varphi = 0.1$. In section 2.1.2 it has already been discussed that a dilute suspension based on a power law fluid can be described with the same power law.

4. Spherical particles

At high deformation rates, $\lambda^{(\text{hom})}\dot{\gamma}_0 \gg 1$, the macroscopic power density can be expressed to the first order of φ as:

$$\langle P \rangle^{(\text{hom})} = \eta_0^{(\text{hom})} (\lambda^{(\text{hom})})^n \dot{\gamma}_0^{2+n} = (1 + [\eta]_\infty \varphi) \eta_0 \lambda^n \dot{\gamma}_0^{2+n}. \quad (4.4)$$

The right hand side of (4.4) is readily obtained, assuming that both $\eta_0^{(\text{hom})}/\eta_0$ and $\lambda^{(\text{hom})}/\lambda$ are functions of φ and keeping the terms up to the first order of φ in a Taylor expansion of their product. The resulting pre-factor should be equal to $1 + [\eta]_\infty \varphi$ due to the definition of $[\eta]_\infty$ given on page 54.

Satisfying the requirement $\langle P \rangle = \langle P \rangle^{(\text{hom})}$, it is obtained from (4.2) and (4.4) that

$$1 + [\eta]_\infty \varphi = \frac{1}{V} \int_{V-V_p} \left[\frac{\dot{\gamma}^2}{\dot{\gamma}_0^2} \right]^{1+\frac{n}{2}} dV. \quad (4.5)$$

Representing $\dot{\gamma}^2$ as a sum of the homogeneous term $\dot{\gamma}_0^2$ and the perturbation term $\Delta(\dot{\gamma}^2) = \dot{\gamma}^2 - \dot{\gamma}_0^2$ it is possible to develop the integrand on the right hand side of (4.5) into a Taylor series in $\Delta(\dot{\gamma}^2)/\dot{\gamma}_0^2$:

$$\left[\frac{\dot{\gamma}^2}{\dot{\gamma}_0^2} \right]^{1+\frac{n}{2}} = \left[1 + \frac{\Delta(\dot{\gamma}^2)}{\dot{\gamma}_0^2} \right]^{1+\frac{n}{2}} \approx 1 + \left(1 + \frac{n}{2}\right) \frac{\Delta(\dot{\gamma}^2)}{\dot{\gamma}_0^2} + \frac{n}{4} \left(1 + \frac{n}{2}\right) \left[\frac{\Delta(\dot{\gamma}^2)}{\dot{\gamma}_0^2} \right]^2. \quad (4.6)$$

Substituting (4.6) into (4.5) the following expression is obtained

$$1 + [\eta]_\infty \varphi = 1 - \varphi + \left(1 + \frac{n}{2}\right) I_A + \frac{n}{4} \left(1 + \frac{n}{2}\right) I_B, \quad (4.7)$$

where

$$I_A = \frac{1}{V} \int_{V-V_p} \frac{\Delta(\dot{\gamma}^2)}{\dot{\gamma}_0^2} dV, \quad I_B = \frac{1}{V} \int_{V-V_p} \left[\frac{\Delta(\dot{\gamma}^2)}{\dot{\gamma}_0^2} \right]^2 dV. \quad (4.8)$$

The integral I_A can be calculated considering the Einstein limit with $n = 0$:

$$1 + 2.5\varphi = 1 - \varphi + I_A. \quad (4.9)$$

This gives $I_A = 3.5\varphi$. Note that the integral I_A is independent on $\dot{\gamma}_0$, as it defines a value of the rate-independent viscosity in the linear regime. In case that $n = -2$ in (4.7) the already mentioned value of $[\eta]_\infty = -1$ is obtained¹ as predicted for the special case of a Wagner fluid [104] by Chateau et al. [34]. The value of integral I_B can be determined from the computational fluid

¹This can be obtained immediately from (4.5), hence it is exact.

4. Spherical particles

dynamics simulation data (see Figure 4.5) using a particular numerical result for the intrinsic viscosity, for example $[\eta]_\infty \approx 0.63$ obtained for $n = -0.9$. By doing this, it is assumed that the integral I_B does not depend on $\dot{\gamma}_0$, as $[\eta]_\infty$ is found to be independent on $\dot{\gamma}_0$ for the volume fractions studied (see Figure 4.3). If $[\eta]_\infty$ will start to depend on $\dot{\gamma}_0$ at higher volume fractions, this would mean that the effective viscosity of the suspension will not be described by the same power law as the matrix viscosity but by a power law with another exponent. Finally, the intrinsic viscosity can be expressed as a function of the thinning exponent n as:

$$[\eta]_\infty \approx 2.5 + \frac{47}{20}n + \frac{3}{10}n^2. \quad (4.10)$$

For completeness, one can also do a least squares fit to obtain the value of I_B and gets:

$$[\eta]_\infty \approx 2.5 + \frac{93}{40}n + \frac{23}{80}n^2$$

but since the difference between these two relations is very small the first expression is used, i.e. (4.10), for the following calculations. The quadratic function given in (4.10) agrees very well with the CFD simulation data obtained at high values of the effective deformation rate, as can be seen from Fig. 4.5 (orange curve). It reproduces the special case at $n = -2$ as well. The function $[\eta]_\infty(n)$ will be used in the next section to define the parameters $\eta_0^{(\text{hom})}$ and $\lambda^{(\text{hom})}$ in (4.3). This allows for the extension of the Carreau model for the case of dilute suspensions of rigid spherical particles.

4.4. Fitting intrinsic viscosity

The hydrodynamic amplification factor X , defined as the ratio of the suspension viscosity to the matrix viscosity in the linear regime of deformation, is given by the Einstein formula [1, 2]:

$$X = \frac{\eta_0^{(\text{hom})}}{\eta_0} = 1 + 2.5\varphi. \quad (4.11)$$

One can see from (4.10) that the Einstein result is reproduced as $[\eta] = 2.5$ for $n = 0$, i.e. in the linear regime. At high values of the effective deformation rate it follows from (4.4) that

$$1 + [\eta]_\infty\varphi = X \left[\frac{\lambda^{(\text{hom})}}{\lambda} \right]^n. \quad (4.12)$$

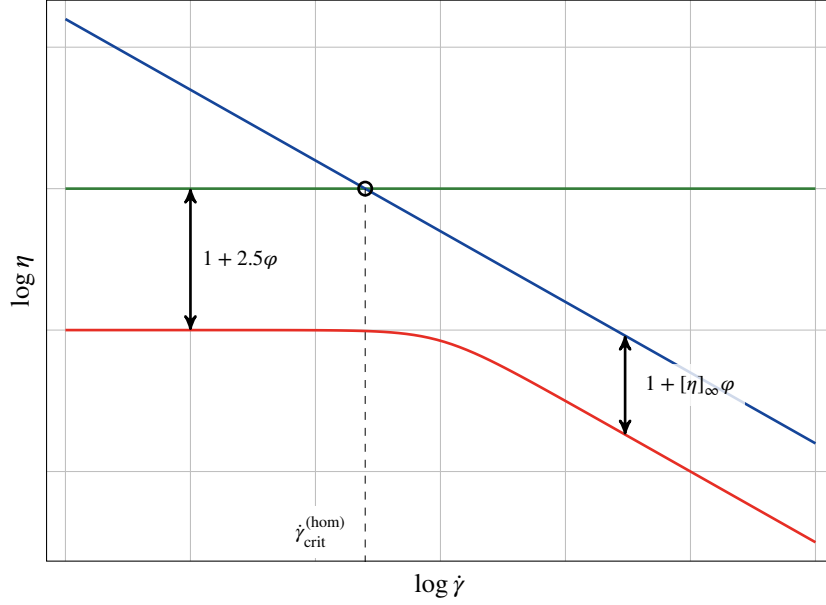


Figure 4.6.: Definition of relaxation time in the Carreau model, $\lambda = \dot{\gamma}_{\text{crit}}^{-1}$.

The characteristic relaxation time of the suspension is defined as the inverse of the deformation rate corresponding to the crossing-point of the two dependences, given by (4.11) and (4.12). This is shown schematically in Fig. 4.6 and results to the first order of φ in

$$\lambda^{(\text{hom})} = \left(1 + \frac{6n + 47}{20} \varphi\right) \lambda. \quad (4.13)$$

Finally, substituting (4.11) and (4.13) into (4.3), it is obtained that

$$\eta^{(\text{hom})}(\dot{\gamma}_0) = (1 + 2.5\varphi)\eta_0 \left\{ 1 + \left[\left(1 + \frac{6n + 47}{20} \varphi\right) \lambda \dot{\gamma}_0 \right]^2 \right\}^{\frac{n}{2}}. \quad (4.14)$$

Figure 4.7 shows exemplarily the comparison of the simulation data for the intrinsic viscosity at $n = -0.2$, $n = -0.5$ and $n = -0.9$ with the results predicted by the modified Carreau model given by (4.14). It can be seen that the modified Carreau model describes the simulation data at all deformation rates quite well, even the transition region between the linear (high plateau) and power law (low plateau) regimes. Similar results are obtained for all other values of the thinning exponent n .

It is interesting to consider another quantity which is usually used to describe the onset of the non-linear regime. This is the so-called critical deformation rate $\dot{\gamma}_{\text{crit}}$ which is equal to the inverse of the characteristic relaxation time in (2.17) or (4.3) and is marked by a circle in figure 4.6. This

4. Spherical particles

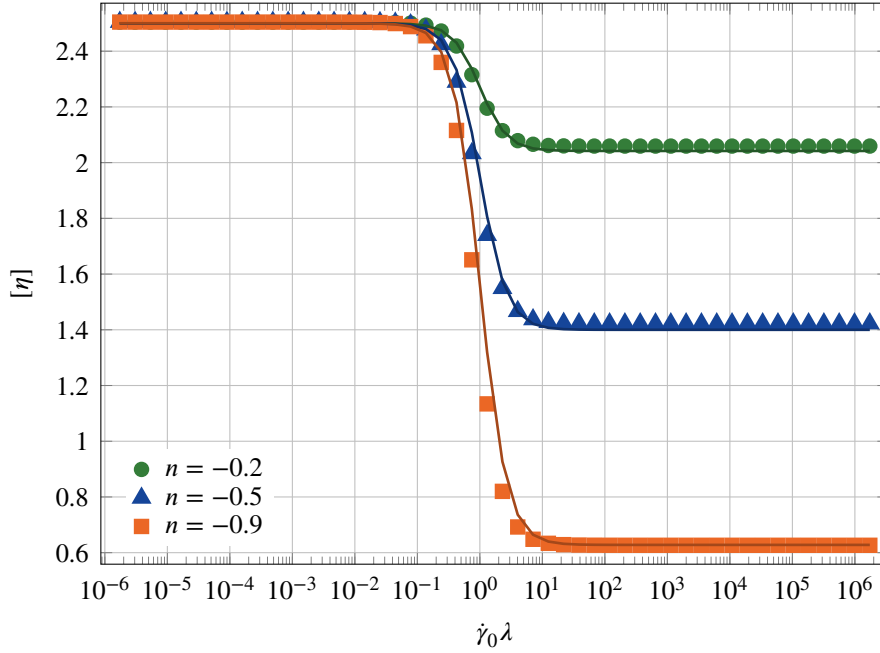


Figure 4.7.: Dependence of the intrinsic viscosity on the Carreau number. Simulation results: symbols; prediction of the modified Carreau model as given by (4.14): lines.

study predicts that $\dot{\gamma}_{\text{crit}}^{(\text{hom})}$ for the suspension of hard spheres decreases with the increase of volume fraction φ as

$$\dot{\gamma}_{\text{crit}}^{(\text{hom})}(\varphi) = \left(1 - \frac{6n + 47}{20}\varphi\right) \dot{\gamma}_{\text{crit}}, \quad (4.15)$$

where $\dot{\gamma}_{\text{crit}} = \lambda^{-1}$. A decrease in the critical deformation rate reflects the effect of strain amplification in the matrix fluid. The critical deformation rate exhibits a weak dependence on n as shown in figure 4.8 for a volume fraction of $\varphi = 0.05$. The figure shows further the graphs of the strain amplification factor as used in Domurath et al. [61]

$$\dot{\gamma}_{\text{crit, simple}}^{(\text{hom})} = (1 - \varphi)\dot{\gamma}_{\text{crit}} \quad (4.16)$$

and the strain amplification factor used by Chateau et al. [34], that is:

$$\dot{\gamma}_{\text{crit, Chateau}}^{(\text{hom})} = \sqrt{\frac{1 - \varphi}{X}} \dot{\gamma}_{\text{crit}} = \sqrt{\frac{1 - \varphi}{1 + 2.5\varphi}} \dot{\gamma}_{\text{crit}} \approx \left(1 - \frac{7}{4}\varphi\right) \dot{\gamma}_{\text{crit}}. \quad (4.17)$$

The latter two equations do not depend on the thinning exponent n . It can be seen in Fig. 4.8 that the present result for the critical deformation rate (4.15) and the factor used by Chateau et al. [34] (4.17) intersect at $n = -2$ and that they differ more and more with increasing n . One should

4. Spherical particles

keep in mind that the critical shear rate has no meaning in the case when $n = 0$. The simple average as given by (4.16) is always above, hence it underpredicts the strain amplification.

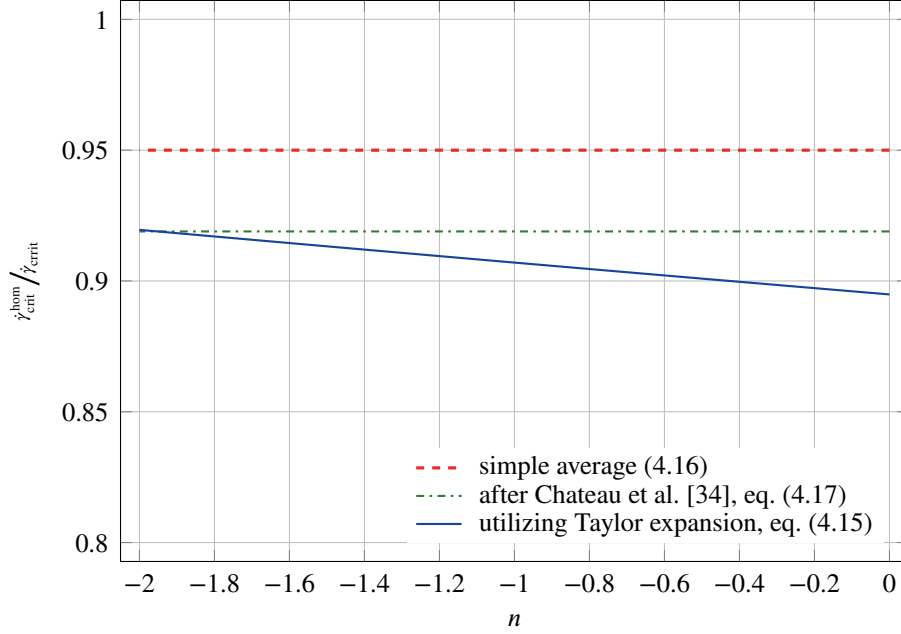


Figure 4.8.: Dependence of the relative critical deformation rate on the thinning exponent n as given by (4.15). We plot results at $\varphi = 0.05$ for better comparison.

4.5. Discussion of strain amplification

In the previous study of Domurath et al. [61] it has been proposed to modify the Carreau equation for a suspension of rigid spherical particles in a thermoplastic matrix as follows:

$$\eta^{(\text{hom})}(\dot{\gamma}_0) = X\eta_0 \left(1 + (a_d \lambda \dot{\gamma}_0)^2\right)^{\frac{n}{2}}. \quad (4.18)$$

where the strain amplification factor a_d is defined by (2.21) and X is given by the Einstein formula (4.11). This proposal was based on the stress and strain amplification approach (SSAA) for non-linear constitutive equations. Equation (4.14) elaborated in this work is clearly of the same form as (4.18). The only, but nevertheless essential, difference is the dependence of the strain amplification factor a_d on φ and n . Comparing (4.14) and (4.18), the following expression for a_d up to the 1st order in n is obtained:

$$a_d = 1 + \frac{6n + 47}{20} \varphi. \quad (4.19)$$

4. Spherical particles

This expression is an outcome of CFD simulation data, in which different powers of the scalar deformation rate $\dot{\gamma}$ have been averaged over the representative volume element. The effective viscosity of a suspension based on the Carreau matrix with the thinning exponent n is defined by two averages: by $\langle \dot{\gamma}^2 \rangle$ in the region of the Newtonian plateau and by $\langle \dot{\gamma}^{n+2} \rangle$ in the power law region. As the latter average carries in it the dependence on n , the strain amplification factor depends also on n . This effect has not been taken into account in a previous study of Domurath et al. [61]. Instead it was assumed that averages of other powers of $\dot{\gamma}$ over the deformable volume $V_m = V - V_p$ can be approximated by the respective powers of $\langle \dot{\gamma} \rangle_m$ defined by (2.21):

$$\langle \dot{\gamma}^n \rangle_m \approx \langle \dot{\gamma} \rangle_m^n = (1 - \varphi)^{-n} \dot{\gamma}_0^n, \quad (4.20)$$

Such an approach predicts that the critical shear rate decreases with the increase of volume fraction as given in (4.16). Another approach that can be found in literature [62, 63, 105] is to use $\langle \dot{\gamma}^2 \rangle_m$ to calculate averages of other powers of $\dot{\gamma}$:

$$\langle \dot{\gamma}^n \rangle_m \approx \langle \dot{\gamma}^2 \rangle_m^{n/2} = \left(\frac{X}{1 - \varphi} \right)^{n/2} \dot{\gamma}_0^n. \quad (4.21)$$

These averages then replace the corresponding powers of the magnitude of applied rate-of-strain tensor in modified non-linear equations. Based on this suggestion, Chateau et al. [34] obtained the already mentioned linear estimate for the intrinsic viscosity of a dilute suspensions, see (2.32). Further, it follows from (4.21) that the critical deformation rate should decrease with the increase of volume fraction as given in (4.17). From the approach taken by Chateau et al. [34] the aforementioned intersection of the two results given by (4.15) and (4.17) at $n = -2$ is to be expected as at this value of n the behaviour of the modified Carreau model is exactly given by the average $\langle \dot{\gamma}^2 \rangle_m$. Overall, the estimate given by Chateau et al. [34] is closer to the CFD results and this is further in accordance with the finding of Suquet [62] that the approximation (4.21) provides more accurate results than the approximation (4.20). A question arises whether results obtained in this study can be used to obtain more accurate predictions for suspensions based on non-linear viscoelastic matrices for example described by the Wagner [104] and the Doi-Edwards [106] constitutive models. As found in this study, the stress and strain amplification approach proposed by Domurath et al. [61] correctly predicts the form of a constitutive law for viscous suspensions and even reproduces the CFD result if a correct average of $\dot{\gamma}$ is used. This average can be obtained knowing the thinning exponent of the non-linear constitutive equation, namely $n = -2$ for the Wagner model [104] and $n = -3/2$ for the Doi-Edwards model [51, 106].

4.6. Extension to higher volume fractions

Until now only the dilute limit was considered but in practical applications one normally deals with higher volume fractions, say 20% to 30%.

To extend the obtained results to higher volume fractions a mean-field type approach, in the style of Krieger and Dougherty [9], is used. In the following only a short derivation is presented, for a more elaborate one the reader is referred to [57]. The argumentation begins with assuming that every new particle added to a fluid changes its viscosity as:

$$d\eta^{(\text{hom})} = \eta^{(\text{hom})}[\eta] d\varphi. \quad (4.22)$$

It is then stated that there are already a few particles in the fluid and it has already a viscosity of $\eta^{(\text{hom})}(\varphi)$ and the occupiable volume that is left for new particles has decreased to $1 - k\varphi$. The factor k is a correction constant, because it will not be possible to have only particles, some maximum packing will be reached first. When a new particle is added to the suspension its viscosity becomes

$$\eta^{(\text{hom})}(\varphi) + d\eta^{(\text{hom})} = \eta^{(\text{hom})}(\varphi) \left\{ 1 + [\eta] \frac{d\varphi}{1 - k\varphi} \right\}. \quad (4.23)$$

This equation can be rearranged and integrated to get

$$\int_{\eta'=\eta}^{\eta^{(\text{hom})}(\varphi)} d \ln \eta' = \int_{\varphi'=0}^{\varphi} \frac{[\eta]}{k} d \ln(1 - k\varphi'), \quad (4.24)$$

where η is the viscosity of the matrix fluid and $\eta^{(\text{hom})}$ is the zero shear viscosity of the suspension. Evaluating the integrals in (4.24) it is obtained

$$\frac{\eta^{(\text{hom})}}{\eta} = \left(1 - \frac{\varphi}{\varphi_{\max}} \right)^{-[\eta]\varphi_{\max}}. \quad (4.25)$$

Here k is assumed to be equal to $k = 1/\varphi_{\max}$ with φ_{\max} a maximum volume fraction of particles. Thus, the viscosity diverges when the dense packing of particles is reached.

In the specific case considered in this study the value for amplification factor of the zero shear viscosity is then found to be:

$$X = \left(1 - \frac{\varphi}{\varphi_{\max}} \right)^{-2.5\varphi_{\max}}, \quad (4.26)$$

which is just the Krieger-Dougherty equation [9]. By similar argumentation as in section 4.4 it is

4. Spherical particles

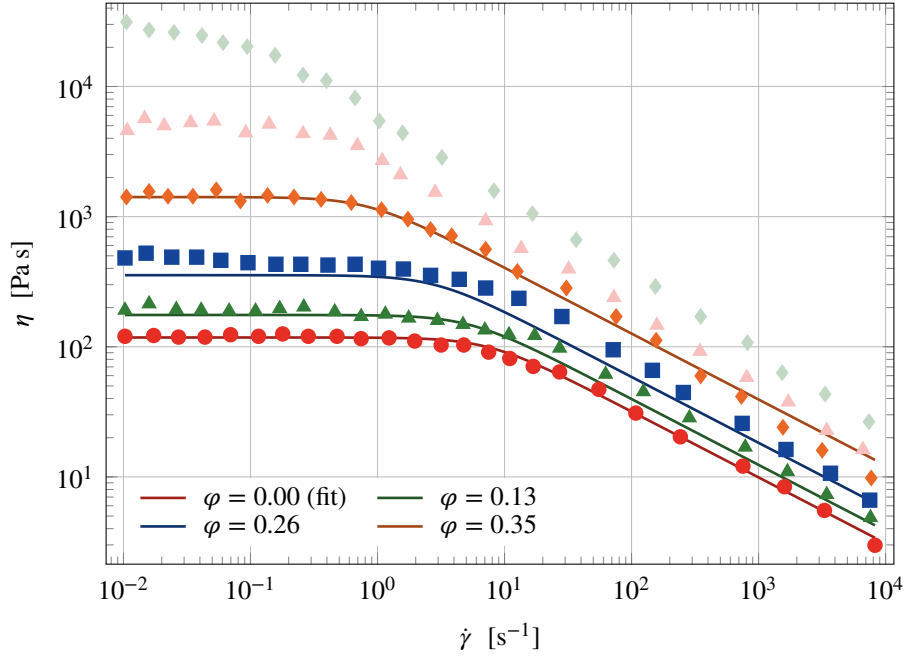


Figure 4.9.: Application of (4.18) to the data of Poslinski et al. [31], with $\eta_0 = 118 \text{ Pa s}$, $\lambda = 0.13 \text{ s}^{-1}$, $n = -0.5$ and $\varphi_{max} = 0.38$. The two highest volume fractions (0.46 and 0.6) are omitted, see text.

possible to obtain an expression for the strain amplification factor similar to (4.26)

$$\left(1 - \frac{\varphi}{\varphi_{max}}\right)^{-[\eta]_{\infty} \varphi_{max}} = X \left[\frac{\lambda^{(hom)}}{\lambda}\right]^n \quad (4.27)$$

where X is now given by (4.26). Equation (4.27) can be rearranged to obtain the strain amplification factor as

$$a_d = \frac{\lambda^{(hom)}}{\lambda} = \left(1 - \frac{\varphi}{\varphi_{max}}\right)^{-\frac{6n+47}{20} \varphi_{max}}. \quad (4.28)$$

The factors (4.26) and (4.28) can be used in the modified Carreau model (4.18). In this approach the only free parameters are the zero shear viscosity and characteristic time of the unfilled system and a maximal volume fraction, φ_{max} , for the suspension. There is only one parameter φ_{max} to describe the change of viscosity and characteristic time with increasing filler volume. Figure 4.9 shows the prediction of our approach compared with data from Poslinski et al. [31]. For this the Carreau model was fitted to the data set with $\varphi = 0$ to extract the zero shear viscosity and characteristic time of the unfilled system. Afterwards the zero shear viscosities for all volume fractions have been fitted with (4.26) to obtain the value of φ_{max} . The two highest volume fractions can not be fitted well to the Krieger-Dougherty equation (4.26) and are omitted. As can be seen

from Figure 4.9, the predictions are quite good, especially for the onset of shear thinning. Yet at high shear rates there is a change in slope in the data of Poslinski et al. [31] and the presented approach cannot predict this kind of behaviour, as at high shear rates the predicted slope is always the same (independent of filler volume) and has the value of the unfilled system.

4.7. Summary

- Computational fluid dynamics (CFD) simulations are performed to determine the intrinsic viscosity in a Carreau fluid filled with rigid spherical particles.
- A modified Carreau model is proposed for a dilute suspension of rigid spheres in a Carreau fluid. The model has the following form

$$\eta^{(\text{hom})}(\dot{\gamma}_0) = X\eta_0 \left(1 + (a_d \lambda \dot{\gamma}_0)^2\right)^{\frac{n}{2}}.$$

with X the linear hydrodynamic amplification factor and a_d the strain amplification factor.

- The strain amplification factor a_d is a linear function in the thinning exponent n of the Carreau model

$$a_d = 1 + \frac{6n + 47}{20}\varphi.$$

- The critical deformation rate, that marks the onset of the non-linear regime, thereby also depends on the thinning exponent n . This result differs noticeably from the two n -independent estimates found in literature.
- The model is extended to high volume fraction of particle using a mean field approach and successfully compared to experimental data of Poslinski et al.

5. Spheroidal particles

5.1. Introduction

In this chapter computational fluid dynamics simulations are performed to study the bulk properties of dilute suspensions of rigid spheroidal particles in a non-Newtonian matrix fluid. In particular, the simulations are performed for a wide range of aspect ratios from highly oblate to highly prolate spheroids. The CFD simulations allow to compute the rheological coefficients A , B and C for the TIF equation (2.50) in the case of a non-Newtonian matrix fluid. As in the previous chapter a Carreau model is used to describe the matrix. The key difference to the previous simulations of suspensions of spherical particles is that, additionally to the dependence on the thinning exponent n , a dependence on the particles aspect ratio r_a and, possibly, a dependence on the particle orientation is expected.

To determine the rheological coefficients it is necessary to solve for at least three particle orientations. This can be seen from the TIF equation (2.50) as the stress and thus the intrinsic viscosity is defined by a combination of the three rheological coefficients A , B and C . To reduce numerical effort it is feasible to choose particle orientations and flows where symmetry of the problem can be exploited and the particles do not translate. This has been already discussed in section 3.1. By directly employing the homogenization procedure outlined in section 3.5.2, it is possible to find relations for the intrinsic viscosity of the transversely isotropic fluid. The stress in the suspension is given by (2.50) and the power density as¹

$$P^{(\text{TIF})} = \boldsymbol{\sigma}^{(\text{TIF})}(\mathbf{d}_0) : \mathbf{d}_0 \quad (5.1)$$

where \mathbf{d}_0 is the macroscopically applied rate of strain tensor. The stress can also be expressed as

$$\boldsymbol{\sigma}^{(\text{hom})} = 2\eta^{(\text{hom})} \mathbf{d}_0 \quad (5.2)$$

¹Here $\boldsymbol{\sigma}$ is used as symbol for the stress tensor, implying that the pressure has been dropped; as it does not contribute to the power density, see (3.29).

5. Spheroidal particles

with $\eta^{(\text{hom})}$ the homogeneous viscosity of the suspension. Using the above relation for the stress tensor $\boldsymbol{\sigma}^{(\text{hom})}$ the power density is given by

$$\mathbf{P}^{(\text{hom})} = \boldsymbol{\sigma}^{(\text{hom})} : \mathbf{d}_0 = 2\eta^{(\text{hom})} \mathbf{d}_0 : \mathbf{d}_0. \quad (5.3)$$

Since (5.1) and (5.3) describe the exactly the same suspension it follows that $\mathbf{P}^{(\text{TIF})} = \mathbf{P}^{(\text{hom})}$. Realizing that

$$\eta^{(\text{hom})} = \frac{\mathbf{P}^{(\text{TIF})}}{2\mathbf{d}_0 : \mathbf{d}_0}, \quad (5.4)$$

compare this expression with (3.36), it is possible to rearrange (2.5) to give the intrinsic viscosity as

$$[\eta] = \frac{\frac{\mathbf{P}^{(\text{TIF})}(\mathbf{d}_0)}{2\eta \mathbf{d}_0 : \mathbf{d}_0} - 1}{\varphi}. \quad (5.5)$$

The configurations, that is particle position and flow, with the highest symmetry are when the particle is placed in the stagnation point of an elongational flow (uniaxial or planar) and the particle is oriented along one of the coordinate axes. For such configurations the problem can be solved only on one eighth of the RVE. For the afore mentioned configurations in elongation it is possible to find 4 unique configuration by evaluating (5.5), these are shown in table 5.1. The configurations can be altered by permutation the corresponding rows in \mathbf{p} and \mathbf{d}_0 while still giving the same result. It is preferable to always use the same particle orientation \mathbf{p} since the same mesh can be used for all simulations. The configuration (c3) in table 5.1 is particularly nice because it immediately gives the value of C . Nevertheless it is not possible to construct a consistent system of equations from the configurations given in table 5.1 to solve for all three rheological coefficients. This can be seen as the coefficients A and B are linearly dependent in (c1), (c2) and (c4). Therefore, another configuration is needed to separate the rheological coefficients A and B . In a simple shear flow two additional configurations can be found, they are listed in table 5.2. Here it is also assumed that the particle is oriented along one of the coordinate axes. By exploiting the symmetry of the problem it is only necessary to consider one half of the RVE, see section 3.1. Configuration (c6) gives the same result as configuration (c3) but using (c5) it is possible to construct a consistent and determined system of equations to compute the rheological coefficients A , B and C . It is thus possible to compute the rheological coefficients using the configuration (c3) and any of the configurations (c1), (c2) and (c4) in elongation as given in table 5.1 and the configuration (c5) in simple shear from table 5.2.

5. Spheroidal particles

\boldsymbol{p}	\boldsymbol{d}_0	$[\eta]$	
$\begin{bmatrix} 1 \\ 0 \\ 0 \end{bmatrix}$	$d_0 \begin{bmatrix} 1 & 0 & 0 \\ 0 & -\frac{1}{2} & 0 \\ 0 & 0 & -\frac{1}{2} \end{bmatrix}$	$\frac{2A}{3} + \frac{4B}{3} + C$	(c1)
$\begin{bmatrix} 1 \\ 0 \\ 0 \end{bmatrix}$	$d_0 \begin{bmatrix} -\frac{1}{2} & 0 & 0 \\ 0 & 1 & 0 \\ 0 & 0 & -\frac{1}{2} \end{bmatrix}$	$\frac{A}{6} + \frac{B}{3} + C$	(c2)
$\begin{bmatrix} 1 \\ 0 \\ 0 \end{bmatrix}$	$d_0 \begin{bmatrix} 0 & 0 & 0 \\ 0 & -1 & 0 \\ 0 & 0 & 1 \end{bmatrix}$	C	(c3)
$\begin{bmatrix} 1 \\ 0 \\ 0 \end{bmatrix}$	$d_0 \begin{bmatrix} 1 & 0 & 0 \\ 0 & -1 & 0 \\ 0 & 0 & 0 \end{bmatrix}$	$\frac{A}{2} + B + C$	(c4)

Table 5.1.: Unique configurations in uniaxial and planar elongation. Here \boldsymbol{p} is the orientation vector of the particle, \boldsymbol{d}_0 is the applied rate of strain tensor and $[\eta]$ the intrinsic viscosity.

\boldsymbol{p}	\boldsymbol{d}_0	\boldsymbol{w}_0	$[\eta]$	
$\begin{bmatrix} 1 \\ 0 \\ 0 \end{bmatrix}$	$d_0 \begin{bmatrix} 0 & \frac{1}{2} & 0 \\ \frac{1}{2} & 0 & 0 \\ 0 & 0 & 0 \end{bmatrix}$	$d_0 \begin{bmatrix} 0 & \frac{1}{2} & 0 \\ -\frac{1}{2} & 0 & 0 \\ 0 & 0 & 0 \end{bmatrix}$	$B + C$	(c5)
$\begin{bmatrix} 0 \\ 0 \\ 1 \end{bmatrix}$	$d_0 \begin{bmatrix} 0 & \frac{1}{2} & 0 \\ \frac{1}{2} & 0 & 0 \\ 0 & 0 & 0 \end{bmatrix}$	$d_0 \begin{bmatrix} 0 & \frac{1}{2} & 0 \\ -\frac{1}{2} & 0 & 0 \\ 0 & 0 & 0 \end{bmatrix}$	C	(c6)

Table 5.2.: Unique configurations in simple shear. Here \boldsymbol{p} is the orientation vector of the particle, \boldsymbol{d}_0 and \boldsymbol{w}_0 are the applied rate of strain and vorticity tensors and $[\eta]$ the intrinsic viscosity.

5. Spheroidal particles

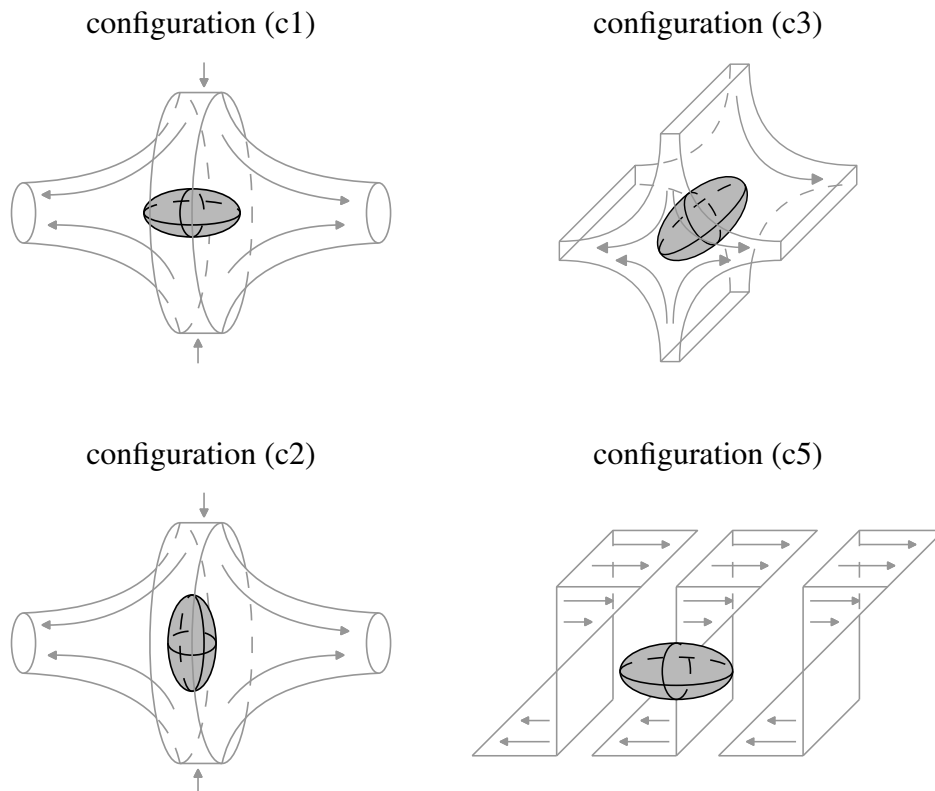


Figure 5.1.: Sketches of the four selected configurations: uniaxial elongation (c1) and (c2), planar elongation (c3) and simple shear (c5).

As mentioned in the literature review, there exist calculations that predict an additional dependence of the stress tensor on the particle orientation for power law fluids filled with rods, see (2.59) in section 2.2.2. Therefore it seems reasonable to check if this is the case for ellipsoids. To check for a possible orientation dependence of the rheological coefficients an additional configuration to the three necessary ones to determine A , B and C is simulated.

Finally the configurations (c1), (c2), (c3) and (c5) have been selected to compute the rheological coefficients and check for a possible orientation dependence. Figure 5.1 shows sketches of these four configurations. The configuration (c3) allows for direct computation of the coefficient C using additionally (c5) one can obtain the coefficient B . Using the results of the intrinsic viscosity for the configurations (c1) and (c2) the coefficient A can be computed in two different ways. In case that the rheological coefficients are independent of the particle orientation, the two computed values of A should be equal. If it is not the case this indicates that there is indeed an additional orientation dependence of the rheological coefficients. It is only possible to check if there is an orientation dependence of A , B and C . To actually determine the dependence on the particle orientation additional simulations will be necessary.

5. Spheroidal particles

The simulations for the configurations (c1), (c2) and (c3) are performed using the method for a fixed particle as described in section 3.3. The boundary conditions have mostly been defined already in section 3.3.2. Only the boundary conditions at Γ_1 and Γ_6 need to be specified here, see figure 3.3. On the boundaries Γ_1 and Γ_6 the velocity is prescribed by means of the macroscopic rate-of-strain tensor, using (3.2). The values for the strain rates in (3.1) are given for the three configurations by

$$\dot{\epsilon}_1 = d_0 \text{ and } \dot{\epsilon}_2 = -0.5d_0 \text{ for configuration (c1),}$$

$$\dot{\epsilon}_1 = -0.5d_0 \text{ and } \dot{\epsilon}_2 = d_0 \text{ for configuration (c2),}$$

$$\dot{\epsilon}_1 = 0 \text{ and } \dot{\epsilon}_2 = -d_0 \text{ for configuration (c3).}$$

The configuration (c5) has been simulated using the method described in section 3.4. For the boundary conditions as described in section 3.4.2 the value of $\dot{\gamma}$ in (3.5) is set equal to d_0 .

To investigate the influence of the shape of the spheroidal particles the simulations are performed for many aspect ratios

$$r_a = \frac{1}{20}, \frac{1}{18}, \dots, \frac{1}{2}, 1, 2, \dots, 18, 20. \quad (5.6)$$

For aspect ratios higher than 20 the particle becomes so pointed that generating proper meshes was a problem. Figures 5.2 and 5.3 show exemplarily the meshes for a prolate and an oblate spheroid. The mesh shown in figure 5.2 shows a prolate particle with an aspect ratio of 10, here only one eighth of the reference cube is meshed since this mesh is for simulations in elongation. The particle in figure 5.3 has an aspect ratio of 1/10. The mesh is cut in half for better visibility of the oblate, since this mesh is for simulations in shear only half of the RVE needs to be meshed. The simulations are performed for the thinning exponents

$$n = 0.0, -0.2, -0.4, -0.6, -0.8. \quad (5.7)$$

The deformation rate d_0 in the rate of strain tensor in the configurations (c1), (c2), (c3) and (c5) is varied between 10^{-6} s^{-1} and 10^{-6} s^{-1} in 50 steps. This results in different scalar deformation rates $\dot{\gamma}$ according to (2.18). In configurations (c1) and (c2) $\dot{\gamma}_0 = \sqrt{3}d_0$, in (c3) $\dot{\gamma}_0 = 2d_0$ and in (c5) $\dot{\gamma}_0 = d_0$. Furthermore, the same material parameters for the Carreau model (2.17) are chosen as for simulations of suspensions of rigid spheres in the previous chapter. These are set to be $\eta_0 = 1 \text{ Pa s}$ and $\lambda = 1 \text{ s}$.

Similar to the suspensions of rigid spheres, it is necessary to check that the simulations are performed in the dilute limit. This is again done by computing the intrinsic viscosity for different volume fractions and if the curves fall together the simulations are performed in the dilute limit. To check this, the intrinsic viscosity has been computed for configuration (c1) for three different

5. Spheroidal particles

volume fractions of the particles. The simulated volume fractions are 10^{-6} , 5×10^{-6} and 10^{-5} . The results are shown in figures 5.4 and 5.5 for all thinning exponents but only for the aspect ratios 18 and 1/18. For the other aspect ratios similar results are obtained. The results for the different volume fractions fall nicely together and hence the simulations are indeed done in the dilute regime. Therefore, the simulations of the other configurations only the volume fraction $\varphi = 10^{-5}$ has been chosen.

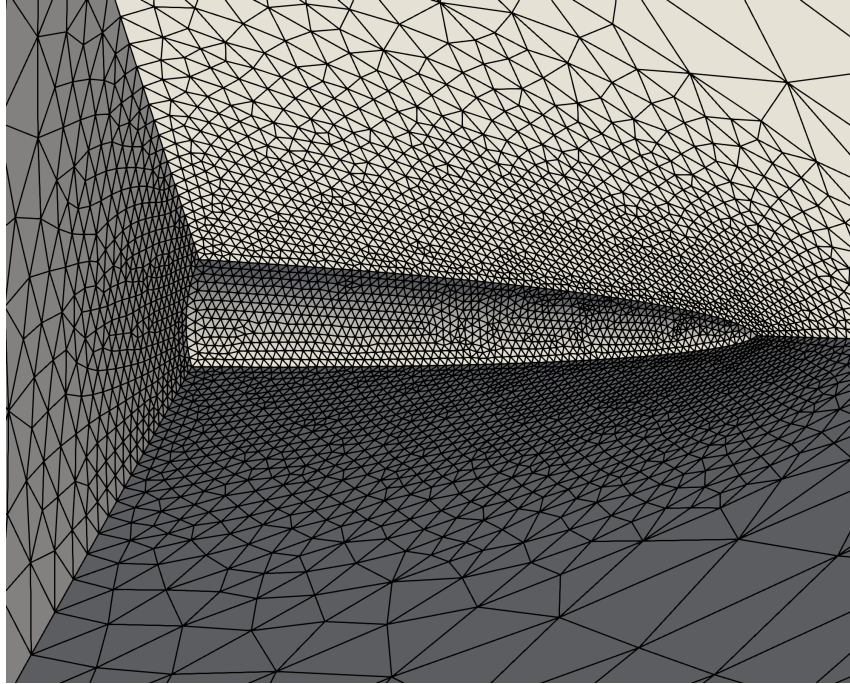


Figure 5.2.: Prolate particle mesh for elongation with an aspect ratio $r_a = 10$.

5.2. Simulation Results

In this section the numerical results for the simulation of suspensions with spheroidal particles in a non-Newtonian fluid are discussed. In figures 5.4 and 5.5 the value of the intrinsic viscosity is plotted against the Carreau number $\dot{\gamma}_0 \lambda$. In these figures the same principal behavior as for spherical particles can be observed for prolate and oblate spheroids. Compare with figure 4.3 in section 4.2. As for the rigid spheres the plateau-crossover-plateau behavior is observed for oblate and prolate spheroids. To explain this behavior it is referred to section 4.2. In the rest of this section only the value of the intrinsic viscosity at high deformation rates is discussed. This value corresponds to the second plateau in case of a non-Newtonian matrix fluid ($n < 0$). This is indicated by an infinity symbol as index.

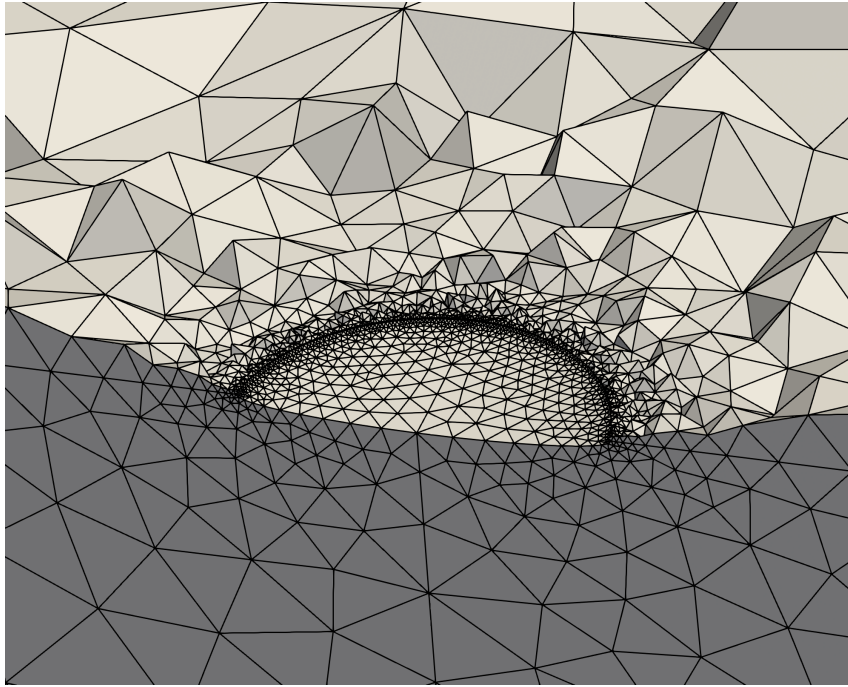


Figure 5.3.: Oblate particle mesh for shear. The mesh is cut in the middle of the oblate with an aspect ratio $r_a = 1/10$.

Figures 5.6 to 5.9 show the intrinsic viscosities at high deformation rates for the four considered configurations. For the Newtonian regime with $n = 0$ the analytical solution of Lipscomb et al. [14] (2.52) for intrinsic viscosity is also plotted. For that the rheological coefficients of Lipscomb et al. [14] (2.52) are inserted into the relations for the intrinsic viscosity given in tables 5.1 and 5.2. In all four cases the numerical data coincides very well with the result of Lipscomb et al. To the author's knowledge this is the first time that the analytical solution for rheological coefficients by Lipscomb has been verified by direct numerical simulations. With decreasing values of n a decrease in the intrinsic viscosity can be observed. This decrease in the intrinsic viscosity becomes more pronounced with increasing (> 1) or decreasing (< 1) aspect ratios. For the configuration (c1) for uniaxial elongation, with the particle aligned with the x direction, the effect of the thinning exponent n on the intrinsic viscosity is stronger for prolate particles. On the contrary, for configuration (c3) in planar elongation the change is more pronounced for oblates. For the configurations (c2) for uniaxial elongation, with the particle aligned with the y direction, and (c5) for simple shear the changes are similar for prolate and oblate particles. The relative change in the intrinsic viscosity at high deformation rates is also different for the different configurations. For example in configuration (c1) for $r_a = 20$ the relative change of $[\eta]_\infty$ between the $n = 0$ and $n = -0.8$ is about 4 while for (c1) it is about 2.5.

5. Spheroidal particles

Using the results for the intrinsic viscosity of the four configurations the rheological coefficients have been calculated and are shown in figures 5.10 till 5.13, in reverse order from C to A . In all figures dashed lines indicate special cases. The vertical line marks the case of a spherical particle with aspect ratio $r_a = 1$. For C_∞ in figure 5.10 the value $C_\infty = 2.5$ is marked as the solution for a spherical particle and the value of 2 as C approaches 2 as the aspect ratio r_a goes to infinity in the case of a Newtonian matrix fluid. The value of B approaches zero as $r_a \rightarrow \infty$ in the Newtonian case. In all figures the results of Lipscomb et al. [14] (2.52) are plotted and the simulations coincide with the analytical solution. Generally in the plots a decrease in the magnitude of the rheological coefficients can be observed as the matrix fluid becomes more non-linear.

In figure 5.10 it can be seen that value of C_∞ for a specific n also converges to constant value as the aspect ratio goes to infinity, as in the Newtonian case. This constant value at large r_a decreases with decreasing n .

For B_∞ in figure 5.11 a decrease in the magnitude with decreasing n can be observed. This decrease is more pronounced for oblate particles. As the aspect ratio tends to infinity the value of B_∞ approaches zero, here no influence of the non-Newtonian matrix behavior can be observed. For a spherical particle, $r_a = 1$, the value of B_∞ is independent of n and takes the value zero.

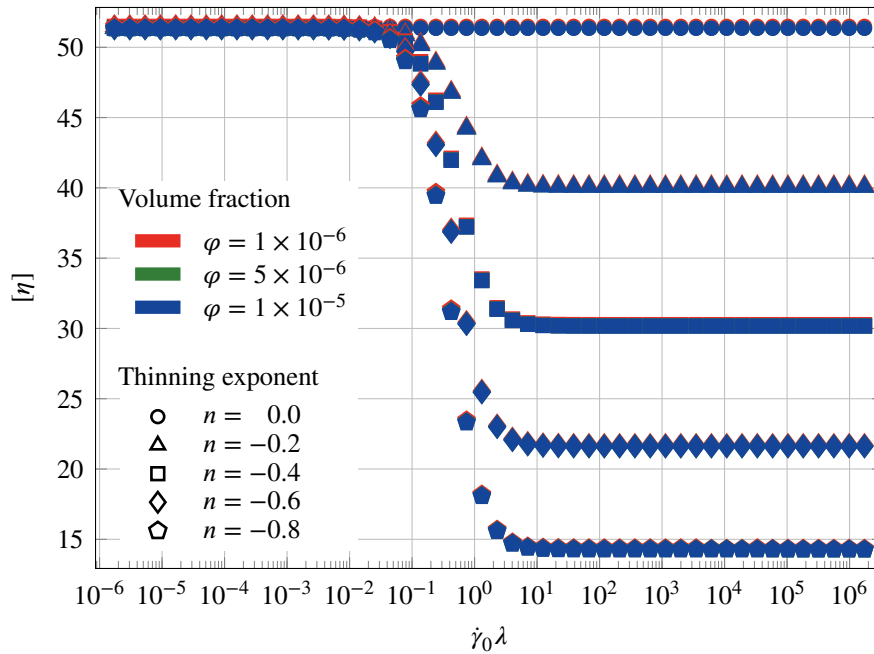


Figure 5.4.: Intrinsic viscosity for different particle volumes, $r_a = 18$. The particles are placed in the stagnation point of a uniaxial elongational flow and oriented along the x direction, configuration (c1).

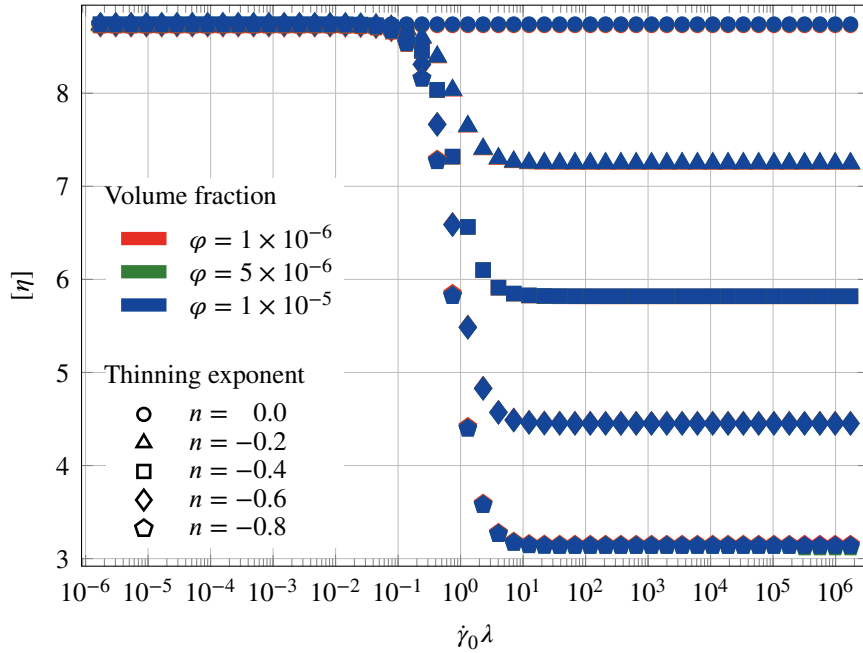


Figure 5.5.: Intrinsic viscosity for different particle volumes, $r_a = \frac{1}{18}$. The particles are placed in the stagnation point of a uniaxial elongational flow and oriented along the x direction, configuration (c1).

In figures 5.12 and 5.13 the values of A_∞ , computed from the two different configurations in uniaxial elongation (c1) and (c2), are plotted. As for B_∞ the value at $r_a = 1$ is independent of n and equal to zero. The curves for the two different orientations of the particle in the uniaxial elongation are qualitatively similar: there is a strong dependence on the aspect ratio for both prolate and oblate particles, as well a noticeable drop of A_∞ with decreasing n . Figure 5.14 shows the comparison of the two configurations for A_∞ at three values of n . For the Newtonian case the results coincide, thus no dependence on the particle orientation can be observed. For the non-Newtonian case the curves for the same n differ more and more with increasing ($r_a > 1$) aspect ratios. For decreasing ($r_a < 1$) aspect ratios there is a slight difference between the two particle orientations, about 4% for $n = -0.8$ and $r_a = 1/20$, which can be neglected. The changes due to the different orientations can be quite significant, for $n = -0.8$ and $r_a = 20$ the values of A_∞ differ by over 40%. This implies an influence of the particle orientation on the rheological coefficient A_∞ . Nevertheless, from the results of the simulation of two fixed orientations it is not possible to conclude how the rheological coefficient A_∞ depends on the orientation of the particle in a flow, nor can be concluded whether the rheological coefficients B_∞ and C_∞ also depend on the particle orientation.

5. Spheroidal particles

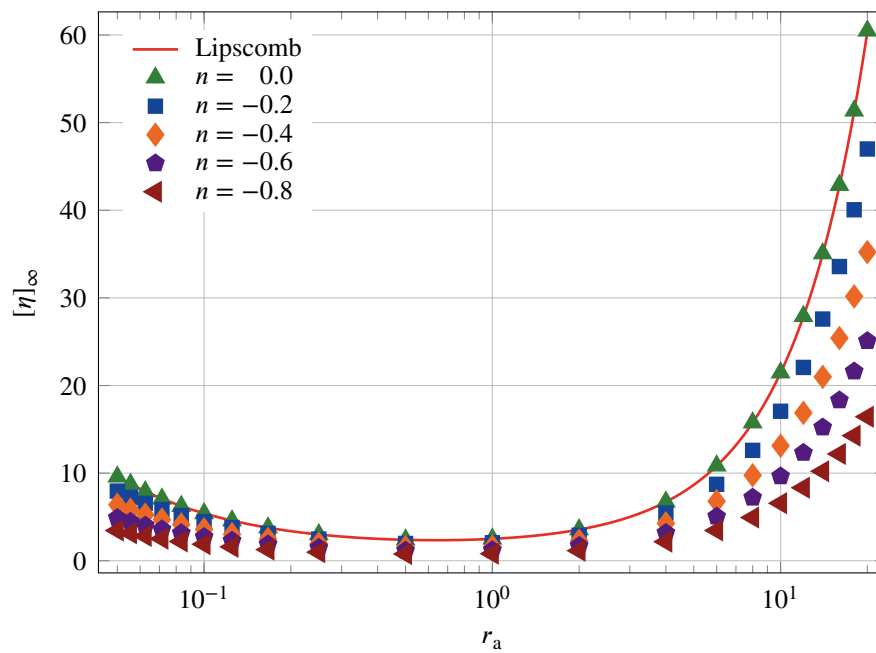


Figure 5.6.: Intrinsic viscosity as function of the particle aspect ratio for configuration (c1), uniaxial elongational flow with the particle aligned with the x direction.

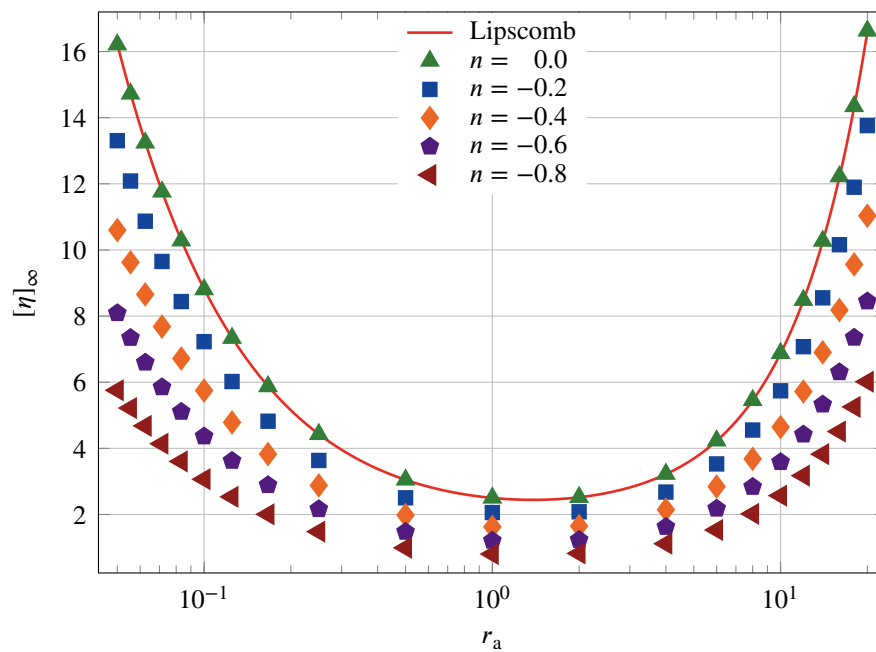


Figure 5.7.: Intrinsic viscosity as function of the particle aspect ratio for configuration (c2), uniaxial elongational flow with the particle aligned with the y direction.

5. Spheroidal particles

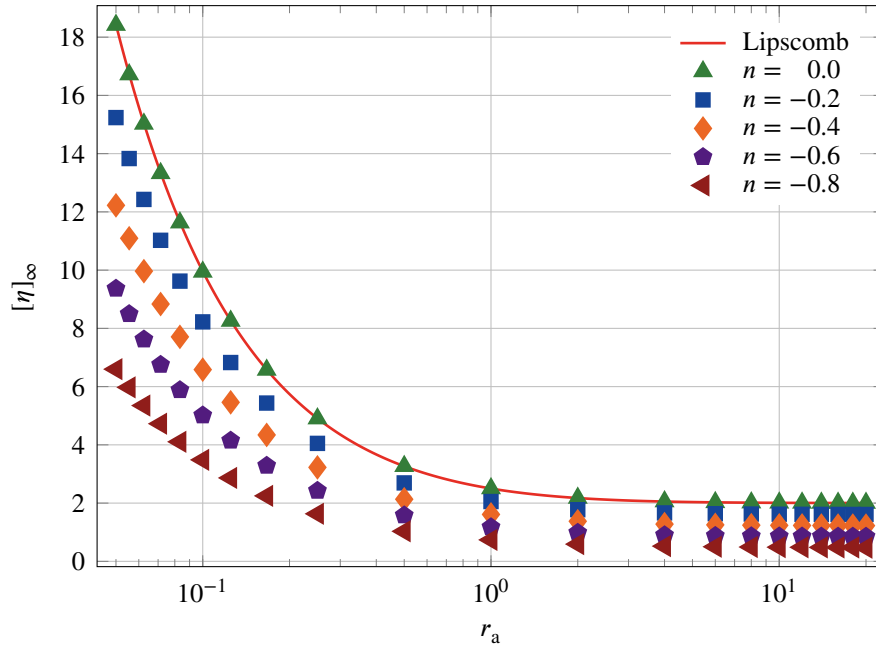


Figure 5.8.: Intrinsic viscosity as function of the particle aspect ratio for configuration (c3), planar elongational flow with the particle aligned with the x direction. The values are equal to C_∞

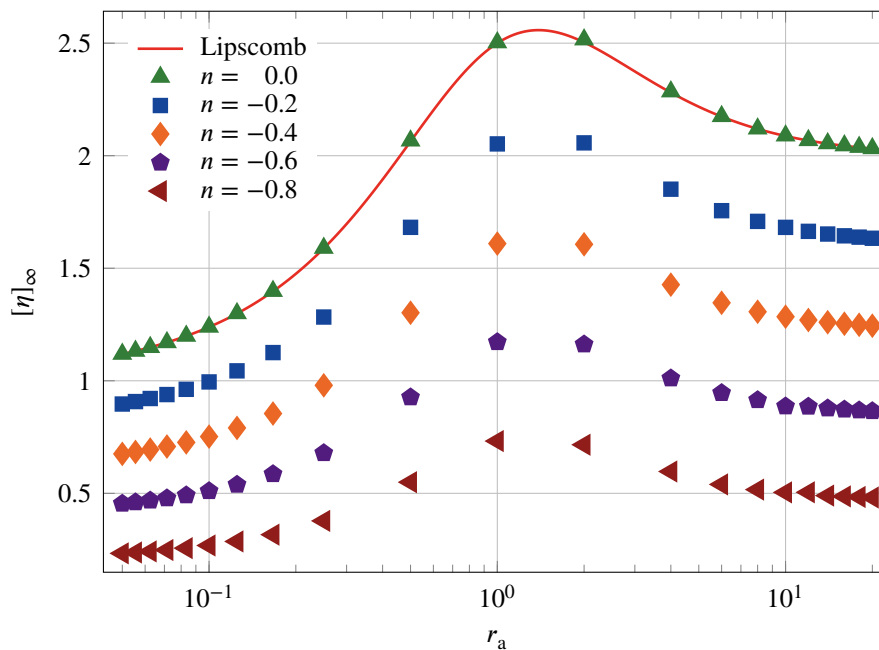


Figure 5.9.: Intrinsic viscosity as function of the particle aspect ratio for configuration (c5), simple shear flow with the particle aligned with the x direction.

5. Spheroidal particles

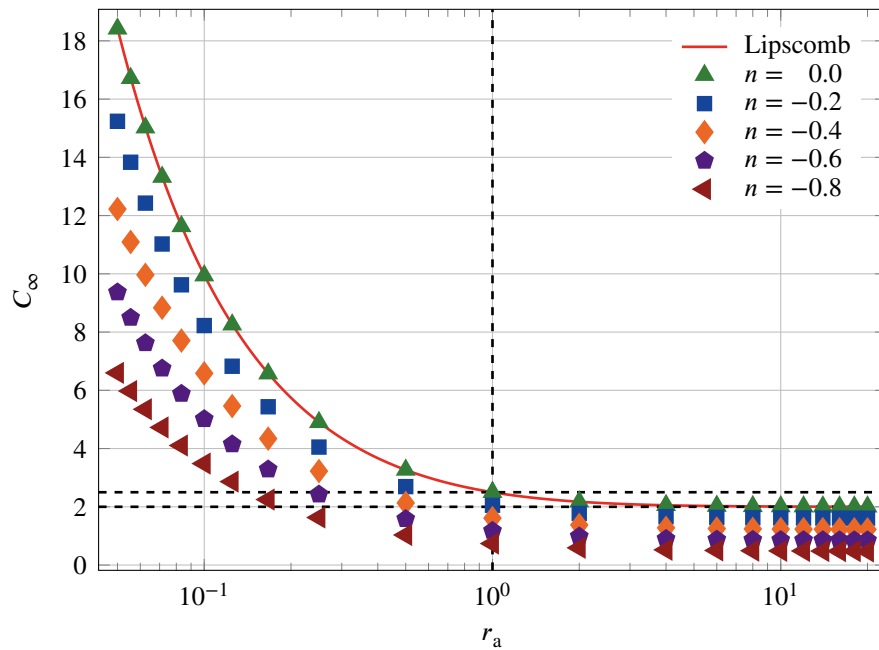


Figure 5.10.: Values for the rheological coefficient C_∞ . In the Newtonian regime for $n = 0$ the results coincide with the solution of Lipscomb et al. [14] given in (2.52).

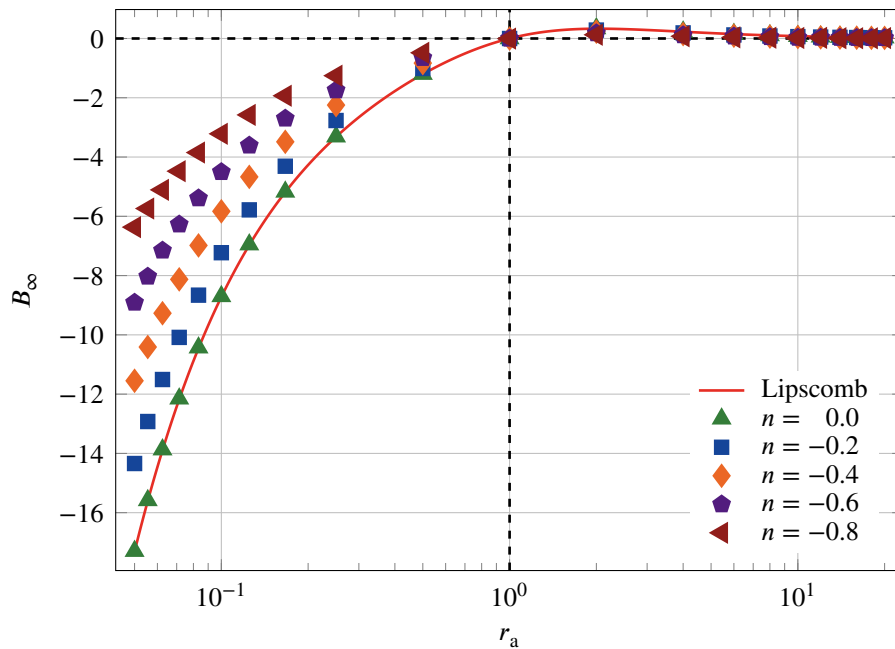


Figure 5.11.: Values for the rheological coefficient B_∞ . In the Newtonian regime for $n = 0$ the results coincide with the solution of Lipscomb et al. [14] given in (2.52).

5. Spheroidal particles

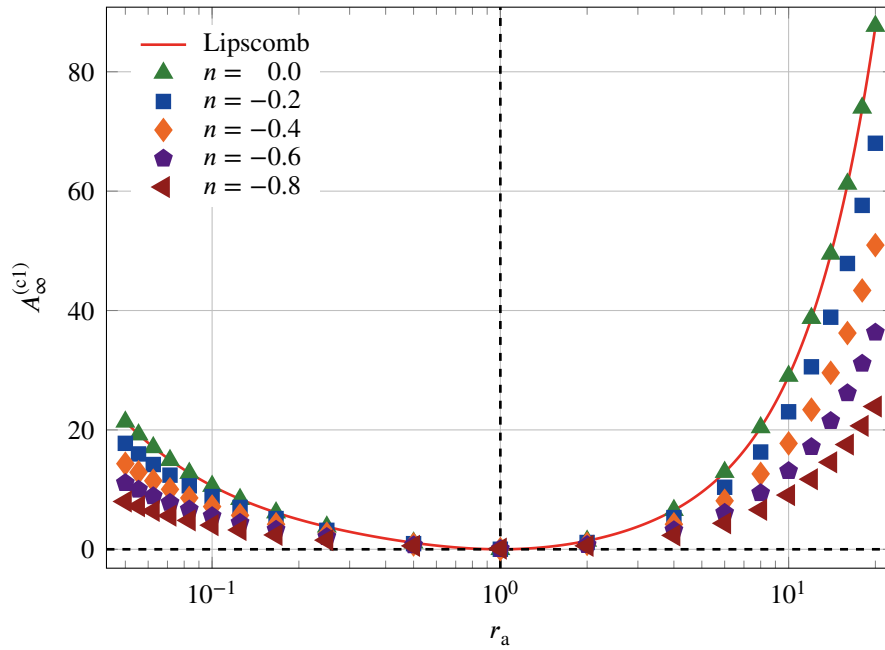


Figure 5.12.: Values for the rheological coefficient A_∞ for the configuration (c1). In the Newtonian regime for $n = 0$ the results coincide with the solution of Lipscomb et al. [14] given in (2.52).

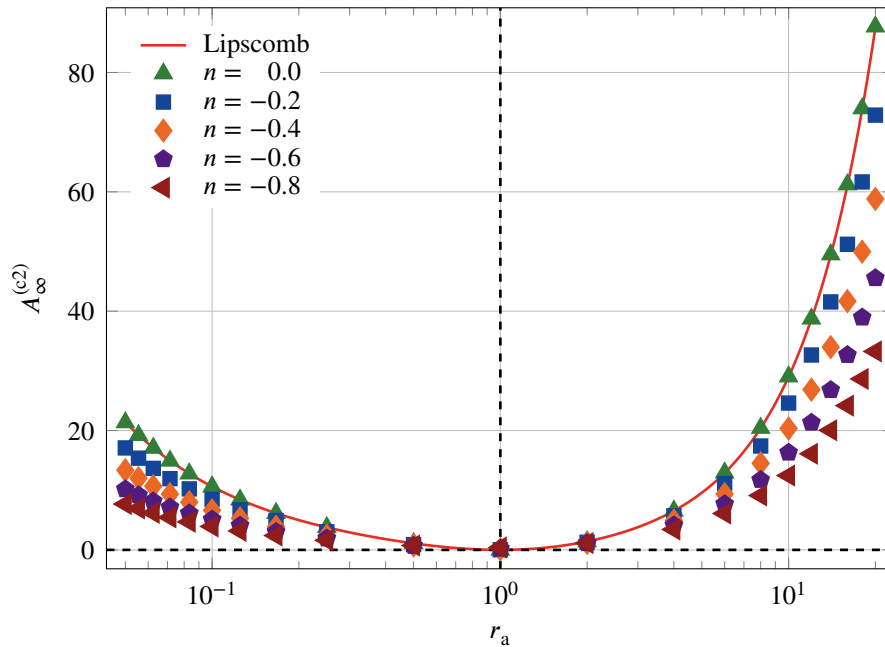


Figure 5.13.: Values for the rheological coefficient A_∞ for the configuration (c2). In the Newtonian regime for $n = 0$ the results coincide with the solution of Lipscomb et al. [14] given in (2.52).

5. Spheroidal particles

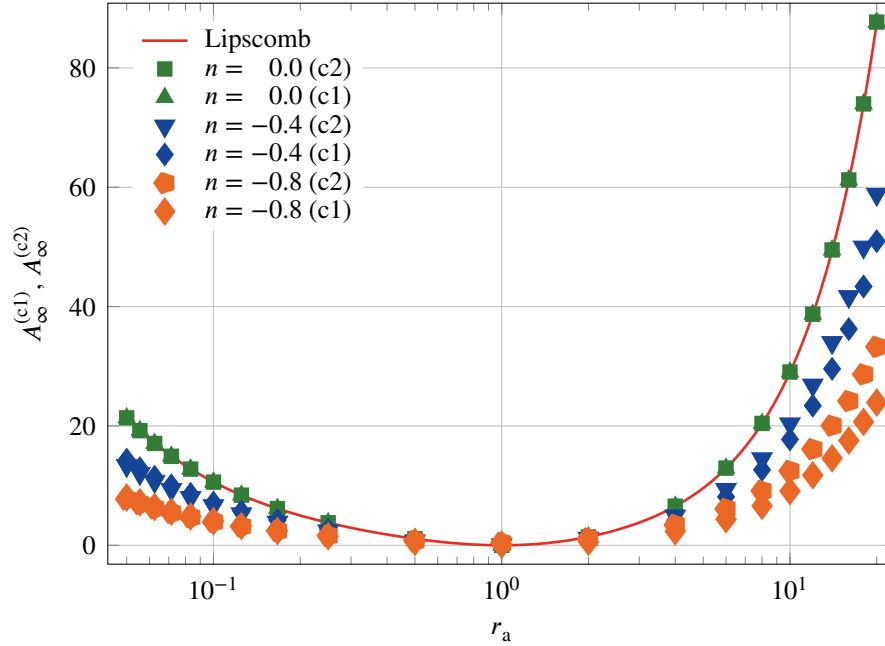


Figure 5.14.: Comparison of the coefficients $A_\infty^{(c1)}$ and $A_\infty^{(c2)}$. In the Newtonian regime for $n = 0$ the results coincide, otherwise not.

As the value of B_∞ goes to zero with increasing aspect ratio for all thinning exponents n , the intrinsic viscosity in configuration (c5) $[\eta]^{(c5)} = B + C$ will converge to the value of C as the aspect ratio is increased. This opens another possibility to check whether an orientation dependence exists for the rheological coefficient C . Since the configuration (c3) in planar elongation directly gives the value of C , it is possible to check if C depends on the orientation of the particle. Since the types of flows in (c3) and (c5) are different it is further possible to check if C depends the type of flow. Figure 5.15 shows the values of the intrinsic viscosities at high deformation rates for the two configurations. The results for aspect ratios smaller than $1/2$ are not shown because B_∞ becomes negative for oblate particles, see figure 5.11. In figure 5.15 it can be nicely seen that for a spherical particle, indicated by the dashed line, the intrinsic viscosities in the two configurations are equal, as $B = 0$ for spheres. For increasing aspect ratios the results for the two configurations converge to the same value for the same thinning exponent. Thus, the simulations indicate that there is no orientation dependence for the rheological coefficient C_∞ in the two considered configurations.

The configuration (c5) describes a rotating particle in a simple shear flow. Therefore, it was also solved for the angular velocity of the particle. It is interesting to compare the angular velocities in a Newtonian matrix with those in a non-Newtonian matrix. For a spherical particle in a simple

5. Spheroidal particles

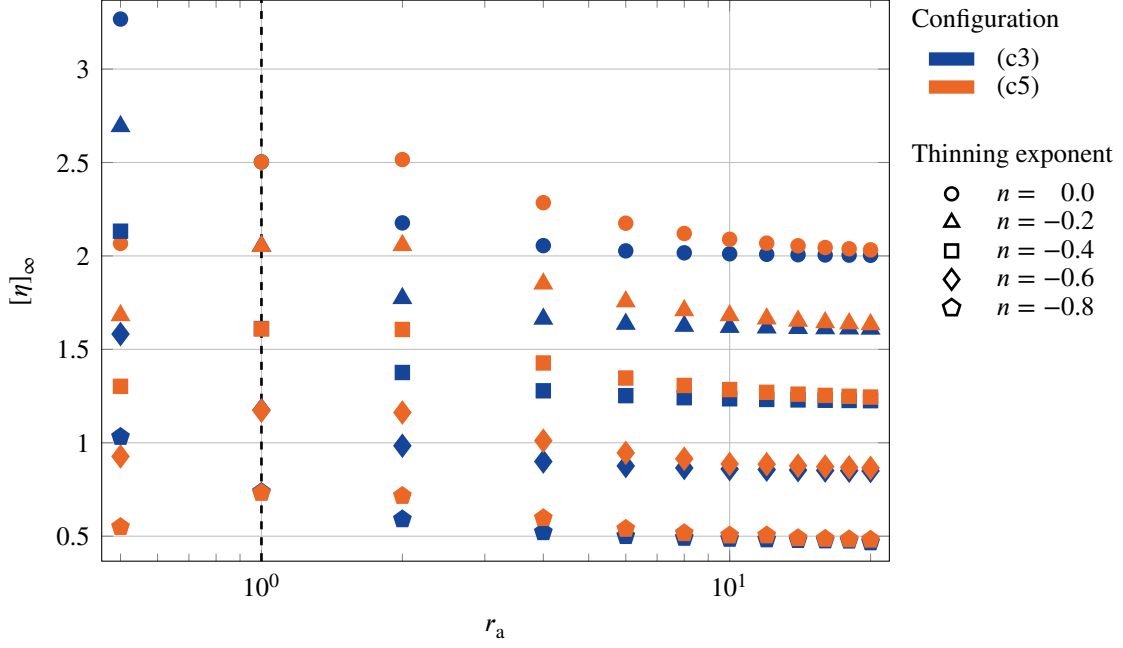


Figure 5.15.: Comparison of $[\eta]_{\infty} = B_{\infty} + C_{\infty}$ in simple shear (c5) and $[\eta]_{\infty} = C_{\infty}$ in planar elongation (c3), for large r_a they converge to the same value, for a given n .

shear flow of a Newtonian fluid the angular velocity is given by

$$\boldsymbol{\omega} = -\frac{1}{2} \text{curl}(\mathbf{u}). \quad (5.8)$$

For the simulated velocity field this results in the angular velocity of a spherical particle

$$\boldsymbol{\omega} = -\frac{1}{2} d_0 \begin{pmatrix} 0 \\ 0 \\ 1 \end{pmatrix}. \quad (5.9)$$

In figure 5.16 the values for the z -component of $\boldsymbol{\omega}$ normalized by d_0 for $n = 0$ and $n = -0.8$ are shown. The other components of $\boldsymbol{\omega}$ are zero, see (5.9), and thus not shown. For the spherical particle the result is independent of n and is equal to $-1/2$. The oblate particles rotate more rapidly, for example the highly oblate particle with $r_a = 1/20$ rotates twice faster than a sphere. Contrary, the rotation of prolate particles slows down with the increase of r_a . This becomes clear as in the considered configuration the particle orientation vector is aligned with the flow direction. Thus, the long semi-axis of the oblate particle stands perpendicular to the flow direction which results in large torque exerted by the fluid on the particle and hence the high angular velocity.

5. Spheroidal particles

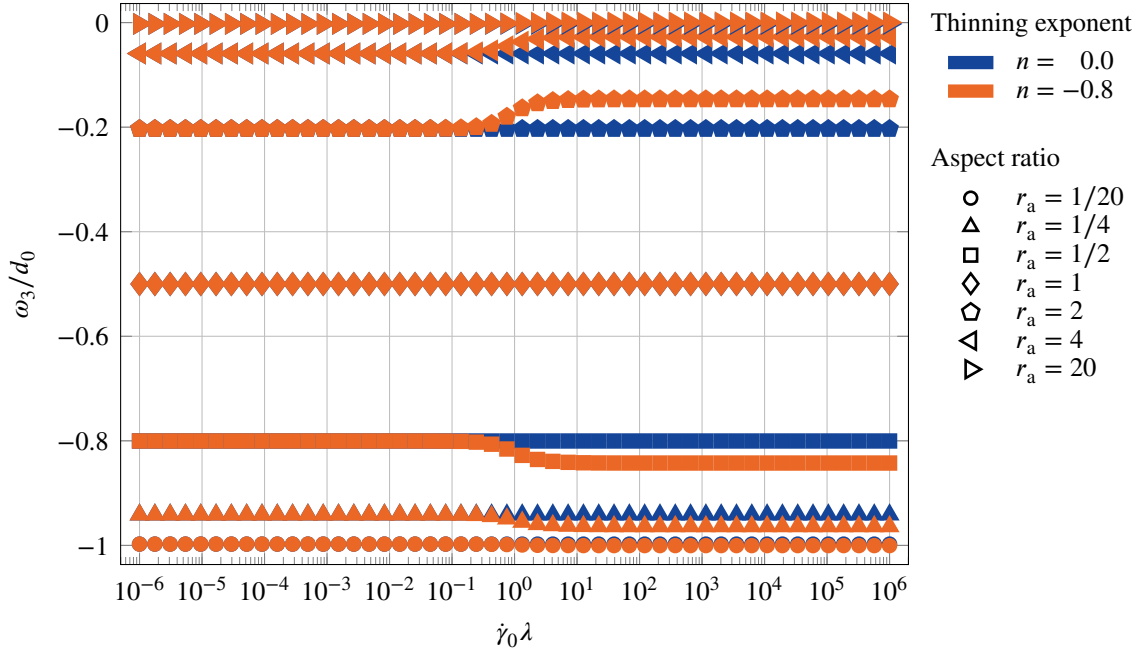


Figure 5.16.: Comparison of the z-component of the angular velocity of particles with different aspect ratios in a simple shear flow.

For the prolate particle it is opposite. For non spherical particles the results for the angular velocity differ slightly in the non-linear regime from those in the linear regime. The change in the non-linear regime is more pronounced for the particle whose aspect ratios are close to a sphere. For the particle with the largest aspect ratio the angular velocity is almost zero. The result corresponds to the result obtained in section 3.1, see equation (3.7). There it was obtained that a spheroidal particle with a large aspect ratio in a shear flow will not change its orientation.

5.3. Ad hoc model for the rheological coefficients

For dilute suspensions of spherical particles it was shown in section 4.3 that in the power law regime the relative change in the power density can be expressed using (4.7). Since a suspension of rigid spherical particles is a spherical case of the TIF equation where $A = B = 0$ it can be assumed that the value of C_∞ can be expressed in a similar form as $[\eta]_\infty$ for spheres, see section 4.4. Thus,

$$C_\infty \varphi = -\varphi c_1 + \left(1 + \frac{n}{2}\right) c_2 + \frac{n}{4} \left(1 + \frac{n}{2}\right) c_3 \quad (5.10)$$

5. Spheroidal particles

with c_1 , c_2 and c_3 being scalar parameters. It is now assumed that the rheological coefficients A_∞ and B_∞ can be expressed in the same form:

$$A_\infty \varphi = -\varphi a_1 + \left(1 + \frac{n}{2}\right) a_2 + \frac{n}{4} \left(1 + \frac{n}{2}\right) a_3 \quad (5.11a)$$

$$B_\infty \varphi = -\varphi b_1 + \left(1 + \frac{n}{2}\right) b_2 + \frac{n}{4} \left(1 + \frac{n}{2}\right) b_3 \quad (5.11b)$$

with a_1 , a_2 , a_3 , b_1 , b_2 and b_3 being scalar parameters. It is possible to determine the values of most parameters from the following considerations. First, as was discussed in chapter 4 the intrinsic viscosity must be equal to -1 for $n = -2$. In this case the relations (5.10) and (5.11) reduce to

$$A_\infty = -a_1 \quad (5.12a)$$

$$B_\infty = -b_1 \quad (5.12b)$$

$$C_\infty = -c_1. \quad (5.12c)$$

As $[\eta] = -1$ for $n = -2$ must hold for any particle orientation, this implies that $a_1 = b_1 = 0$ and $c_1 = -1$ as the term involving C is the only term in the TIF equation that does not depend on the particle orientation.

The parameters a_2 , b_2 and c_2 can be determined by requiring that for $n = 0$ the Newtonian solution must be obtained. This gives $a_2 = A\varphi$, $b_2 = B\varphi$ and $c_2 = (C + 1)\varphi$, where A , B and C are the rheological coefficients given the solution of Lipscomb et al. [14] (2.52).

For the values of the remaining parameters the following assumptions are made

$$a_3 = x_A A \varphi \quad (5.13a)$$

$$b_3 = x_B B \varphi \quad (5.13b)$$

$$c_3 = x_C C \varphi \quad (5.13c)$$

where x_A , x_B and x_C are parameters. If the parameters x_\square are zero the rheological coefficients at high deformation rates are linear functions in n and independent of the particle orientation. Using the parameters x_\square it is thus possible to introduce a dependence of the rheological coefficients on the particle orientation.

5. Spheroidal particles

Thus the model for the rheological coefficients becomes

$$A_\infty = \left(1 + \frac{n}{2}\right) A + \frac{n}{4} \left(1 + \frac{n}{2}\right) x_A A \quad (5.14a)$$

$$B_\infty = \left(1 + \frac{n}{2}\right) B + \frac{n}{4} \left(1 + \frac{n}{2}\right) x_B B \quad (5.14b)$$

$$C_\infty = -1 + \left(1 + \frac{n}{2}\right) (C + 1) + \frac{n}{4} \left(1 + \frac{n}{2}\right) x_C C. \quad (5.14c)$$

In the model (5.14) there is only one free parameter x_\square for each rheological coefficient.

In figures 5.17 to 5.20 the model given in (5.14) is compared with the numerical results obtained. The proposed model fits very well to the numerical results. The values of the parameters x_A , x_B and x_C are “chosen by hand”, no fit has been made. It is surprising that the parameters for the model are the same for $A_\infty^{(c2)}$, B_∞ and C_∞ , that is $x_A^{(c2)} = x_B = x_C = 1.8$. Nevertheless for $A_\infty^{(c1)}$ the model does not fit quite as well as for the other cases, especially at small n .

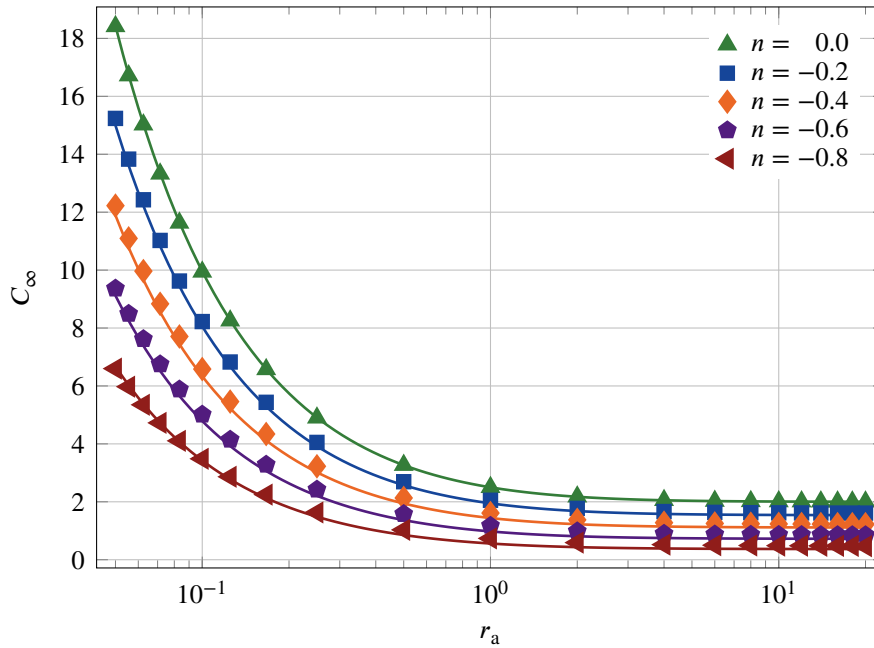


Figure 5.17.: Comparison of the numerical results for C_∞ with the model proposed in (5.14c), curves for $x_C = 1.8$.

5. Spheroidal particles

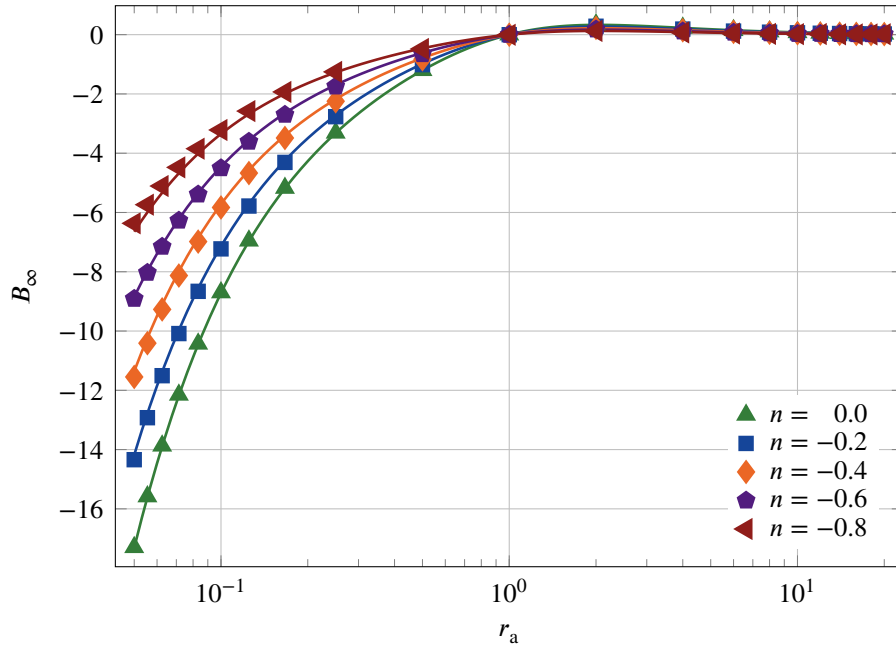


Figure 5.18.: Comparison of the numerical results for B_∞ with the model proposed in (5.14b), curves for $x_B = 1.8$.

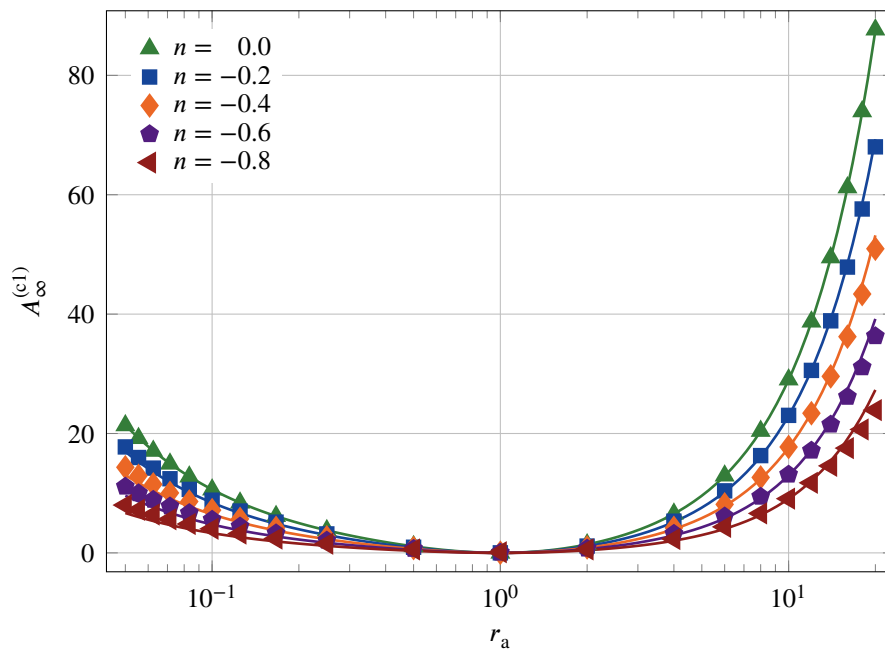


Figure 5.19.: Comparison of the numerical results for $A_\infty^{(c1)}$ with the model proposed in (5.14a), curves for $x_A^{(c1)} = 2.4$

5. Spheroidal particles

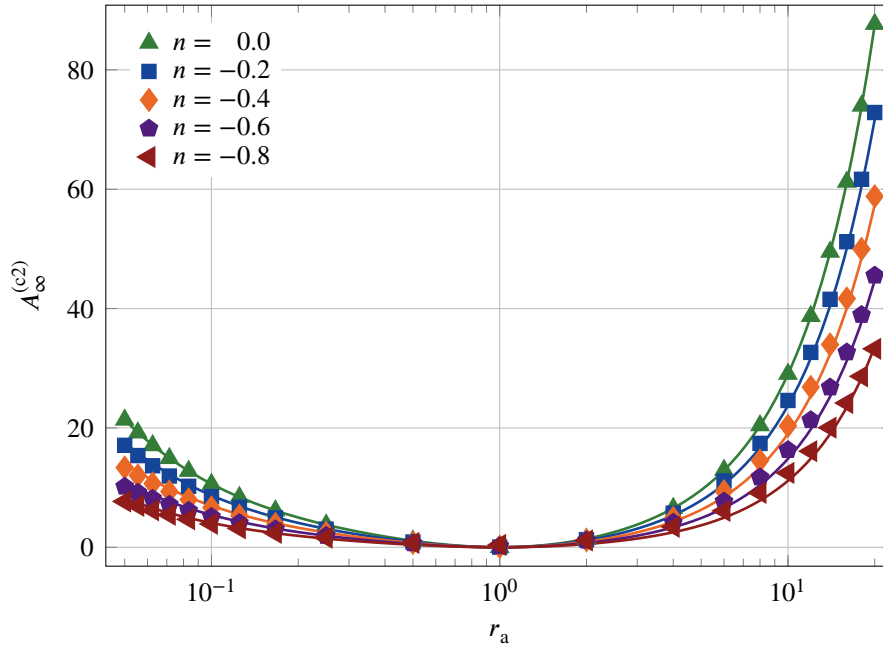


Figure 5.20.: Comparison of the numerical results for $A_{\infty}^{(c2)}$ with the model proposed in (5.14a), curves for $x_A^{(c2)} = 1.8$

5.4. Re-evaluating spherical particles

Using the results obtained in the current chapter it is possible to re-evaluate the model proposed for the intrinsic viscosity at high rates (4.10) for a suspension of spherical particles in chapter 4. Figure 5.21 shows the intrinsic viscosities for spherical particles for the four configurations considered in this chapter. In the Newtonian case the solutions for all four configurations coincide but in the non-Newtonian regime the solutions differ slightly.

The configurations (c1) and (c2) in a uniaxial elongational flow are the same for a spherical particle and thus the same result is obtained. The same case was considered in chapter 4 and therefore the results shown for (c1) and (c2) coincide with the results shown on figure 4.5. Interestingly the values of the intrinsic viscosities for the configurations in planar elongation (c3) and simple shear (c5) are equal but differ slightly from the values obtained for the configurations (c1) and (c2), about 8% for $n = -0.8$. The difference between the configurations (c1) and (c2) and the configurations (c3) and (c5) increases with decreasing values of the thinning exponent n .

In figure 5.22 the numerical results for intrinsic viscosity at high deformation rates are compared with the model for the intrinsic viscosity at high deformation rates (4.10) proposed in chapter 4. The model fits very well to the configurations (c1) and (c2) which is to be expected as these are the configurations the model was initially created for. For the configurations (c3) and (c5)

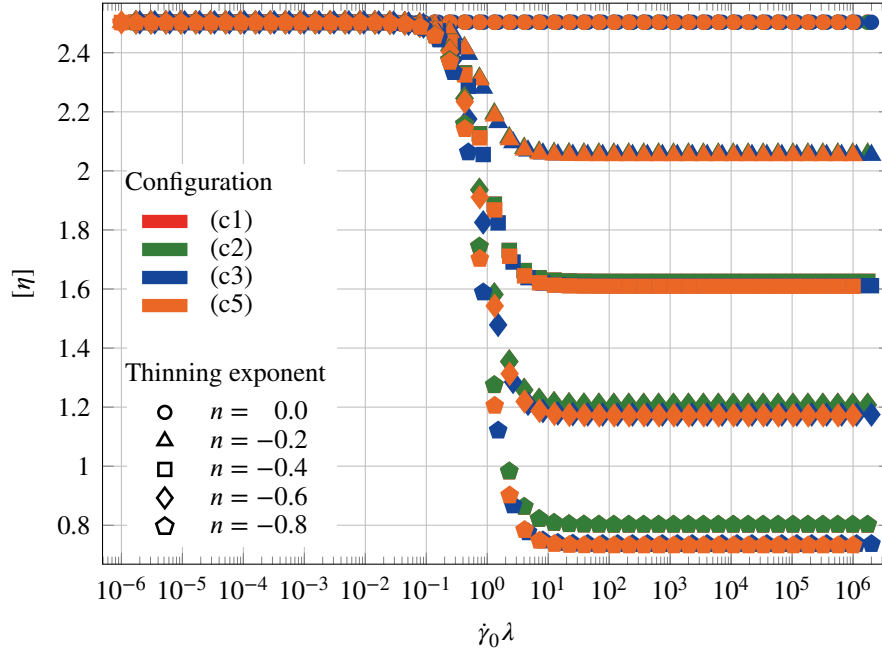


Figure 5.21.: Comparison of $[\eta]$ for spherical particles for the four different configurations.

the numerical results deviate slightly from the curve with decreasing values of n . The difference between the model and the data is still very small. Using the new data one can reevaluate the integrals in (4.8). The cases with $n = 0$ and $n = -2$ are the same. The only difference is that now for $n = -0.8$ the intrinsic viscosity at high rates is $[\eta]_{\infty} \approx 0.74$, this gives

$$[\eta]_{\infty}^{(c3, c5)} = 2.5(1 + n) + \frac{3}{8}n^2. \quad (5.15)$$

It is also possible to apply the model given in equations (5.14) as the spherical case is a special case of this model. In this case $A = B = 0$ and $C = 2.5$ and the model reduces to

$$C_{\infty}^{(\text{sphere})} = [\eta]_{\infty} = -1 + \left(1 + \frac{n}{2}\right) 3.5 + \frac{5n}{8} \left(1 + \frac{n}{2}\right) x_C. \quad (5.16)$$

Equations (5.15) and (4.10) can be reproduced by setting the value x_C in (5.16) to $x_C^{(c3, c5)} = 1.2$ and $x_C^{(c1, c2)} = 0.96$ respectively.

The results presented in this section confirm the conclusion from section 5.2, that in configurations (c3) and (c5) C_{∞} is equal for spheres. Though, the results here imply that there is a dependence on the flow for C_{∞} .

5. Spheroidal particles

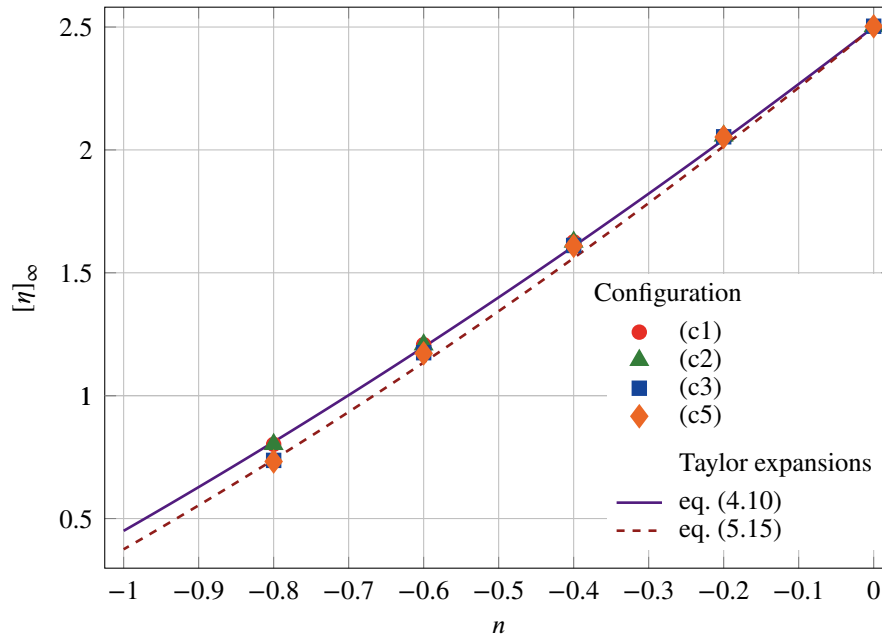


Figure 5.22.: Comparison of the model for $[\eta]_{\infty}$ given by (4.10) with the results for the different configurations.

5.5. Summary

- Computational fluid dynamics (CFD) simulations are performed for different types of flows and multiple particle orientations and the intrinsic viscosities are computed for each flow - particle configuration. From a set of intrinsic viscosities the rheological coefficients for the transversely isotropic fluid (TIF) equation can be determined.
- The numerically computed rheological coefficients for the TIF equation in the Newtonian regime coincide with the analytical result of Lipscomb et al.
- In the non-Newtonian regime the rheological coefficients depend not only on the thinning index n but also on the particle orientation.
- In the power law regime the coefficient B is independent of the thinning exponent n for large aspect ratios being equal to zero.
- An ad hoc model to describe the obtained results for the rheological coefficients is proposed. The model predicts a quadratic dependence on n for all rheological coefficients.
- For spherical particles there is a slight dependence of the intrinsic viscosity on the type of flow.

6. Conclusions

In the present PhD studies the influence of a non-Newtonian matrix fluid on the effective properties of a suspension of rigid spheroidal particles is investigated. A critical review of literature results is given in chapter 2, where it is shown that a superposition of viscosity-stress curves for polymer melts filled with rigid spherical particles by only a vertical shift is unlikely.

To determine the effective properties of the suspensions computational fluid dynamics (CFD) simulations based on the finite element method (FEM) are performed. The suspensions are considered to be dilute and the matrix fluid is modeled using a Carreau model. The simulations are performed for different values of the thinning exponent in the Carreau model and different aspect ratios of rigid spheroidal particles are considered.

To perform the CFD simulations, two different codes are implemented for this thesis. In one code the particle is considered to be fixed, as this is shown to be a possible case for elongational flows. In the other implemented code the particles can flow with the surrounding fluid. Using the implemented software spherical and spheroidal particles are investigated.

Based on the results of the CFD simulations, a modified Carreau model is proposed for a dilute suspension of rigid spheres in a Carreau fluid. The model has the following form

$$\eta^{(\text{hom})}(\dot{\gamma}_0) = X\eta_0 \left(1 + (a_d \lambda \dot{\gamma}_0)^2\right)^{\frac{n}{2}}$$

with X the linear hydrodynamic amplification factor and a_d the strain amplification factor given by

$$a_d = 1 + \frac{6n + 47}{20} \varphi.$$

An important result of the study is that the critical deformation rate that marks the onset of the non-linear regime depends on the thinning exponent n . Therefore, the critical deformation rate differs noticeably from the two n -independent estimates found in literature. The reason is that these two estimates are made using a particular average of the rate-of-strain tensor magnitude over the matrix volume: either on its first or its second power. However, the exact results are defined by averages of the n -th power. Using a mean-field approach the result for the dilute limit

6. Conclusions

is extended to higher volume fractions and is compared with measurements by Poslinski et al. The proposed model agrees well with the data, especially the onset of shear thinning is described very well. One effect observed by Poslinski et al. that the thinning exponent decreases with increasing filler volume cannot be explained the results. The proposed model improves models for power law fluids proposed in literature, as it can also model the crossover from the Newtonian to the power law regime. To investigate the experimentally observed change in the thinning exponent it is necessary to simulate higher concentrations of particles. This is out of the scope of this thesis and is left for future studies within a currently funded DFG project.

For spheroidal particles the rheological coefficients for the transversely isotropic fluid (TIF) equation are numerically computed and coincide with the analytical result of Lipscomb et al. in the case of a Newtonian matrix fluid. It is found, that in the non-Newtonian regime the rheological coefficients differ considerably from the coefficients in the Newtonian case. This clearly shows that the assumption of n -independent rheological coefficients is not valid for filled polymer melts, as commonly presumed in literature. For a non-Newtonian matrix fluid the results show that the rheological coefficients depend on the thinning index n and on the particle orientation. It is found that the coefficient B for large aspect ratios is not influenced by the non-linear behavior and always converges to zero as the aspect ratio increases. A dependence on the particle orientation was found for the coefficient A . Interestingly the orientation dependence is more pronounced for prolate particles. The exact dependence of the rheological coefficients on the particle orientation can not be determined within the present work as this requires more simulations. Thus this is left for a future work in the frame of the DFG project. Nevertheless an ad hoc model to describe the obtained results for the rheological coefficients is proposed. The model works surprisingly well. For spherical particles a slight dependence of the intrinsic viscosity on the type of flow is found. This implies that the rheological coefficients will generally depend on the bulk flow. For aspect ratios larger than 20 it was not possible to create proper meshes anymore. To obtain results such large aspect ratios it is be interesting to simulate capped fibers. These results can also be compared with the models proposed by Gibson and Toll and Souloumiac and Vincent. These simulation studies are presently in progress.

A. Notation

Given the Cartesian basis vectors \mathbf{e}_i

$$\mathbf{e}_1 = \begin{pmatrix} 1 \\ 0 \\ 0 \end{pmatrix} \quad \mathbf{e}_2 = \begin{pmatrix} 0 \\ 1 \\ 0 \end{pmatrix} \quad \mathbf{e}_3 = \begin{pmatrix} 0 \\ 0 \\ 1 \end{pmatrix} \quad (\text{A.1})$$

a vector is defined as

$$\mathbf{a} = a_i \mathbf{e}_i = a_1 \mathbf{e}_1 + a_2 \mathbf{e}_2 + a_3 \mathbf{e}_3 \quad (\text{A.2})$$

and a 2nd order tensor is given by

$$\mathbf{a} = a_{ij} \mathbf{e}_i \mathbf{e}_j = a_{11} \mathbf{e}_1 \mathbf{e}_1 + a_{12} \mathbf{e}_1 \mathbf{e}_2 + \dots \quad (\text{A.3})$$

In the following the basis vectors are omitted, thus instead of $a_i \mathbf{e}_i$ it is just written a_i and the basis vector is implied.

Transpose, symmetry and skew of second order tensors

$$\mathbf{a}^\top = a_{ij}^\top = a_{ji} \quad (\text{A.4})$$

A tensor \mathbf{a} is symmetric if

$$\mathbf{a} = \mathbf{a}^\top \quad (\text{A.5})$$

and skew if

$$\mathbf{a} = -\mathbf{a}^\top. \quad (\text{A.6})$$

A. Notation

A tensor \mathbf{a} can be split into a symmetric and skew part by

$$\mathbf{a} = \underbrace{\frac{1}{2}(\mathbf{a} + \mathbf{a}^\top)}_{\text{sym}(\mathbf{a})} + \underbrace{\frac{1}{2}(\mathbf{a} - \mathbf{a}^\top)}_{\text{skew}(\mathbf{a})} \quad (\text{A.7})$$

The trace of a second order tensor is defines as

$$\text{tr}(\mathbf{a}) = a_{ij} \underbrace{\mathbf{e}_i \cdot \mathbf{e}_j}_{\delta_{ij}} = a_{ii} \quad (\text{A.8})$$

Kronecker delta δ_{ij} and unit tensor $\mathbf{1}$

$$\delta_{ij} = \begin{cases} 0 & \text{if } i \neq j \\ 1 & \text{if } i = j \end{cases} \quad (\text{A.9})$$

$$\mathbf{1} = \delta_{ij} \mathbf{e}_i \mathbf{e}_j \quad (\text{A.10})$$

Permutation tensor or Levi-Civita symbol is defined in 3 spatial dimensions as

$$\varepsilon_{ijk} = \begin{cases} +1 & \text{if } (i, j, k) \text{ is } (1, 2, 3), (2, 3, 1), \text{ or } (3, 1, 2), \\ -1 & \text{if } (i, j, k) \text{ is } (3, 2, 1), (1, 3, 2), \text{ or } (2, 1, 3), \\ 0 & \text{if } i = j, \text{ or } j = k, \text{ or } k = i \end{cases} \quad (\text{A.11})$$

Gradient, Divergence and Curl; following [107].

The gradient of a vector is defined as:

$$\text{grad}(\mathbf{a}) \equiv \frac{\partial a_i}{\partial x_j} = a_{i,j} = L_{ij}. \quad (\text{A.12})$$

If the gradient is defined as above the derivative is taken with respect to the second index.

The divergence of a second tensor is defined as:

$$\text{div}(\mathbf{a}) \equiv \frac{\partial a_{ij}}{\partial x_j} \mathbf{e}_i = D_i = \frac{\partial a_{ij}}{\partial x_j}. \quad (\text{A.13})$$

The curl of a tensor of a vector is defined as:

$$\text{curl}(\mathbf{a}) \equiv \frac{\partial a_k}{\partial x_j} \varepsilon_{ijk} \mathbf{e}_i = A_i. \quad (\text{A.14})$$

Products

$$\mathbf{a} \cdot \mathbf{b} = a_i \mathbf{e}_i \cdot b_j \mathbf{e}_j = a_i b_j \underbrace{\mathbf{e}_i \cdot \mathbf{e}_j}_{\delta_{ij}} = a_i b_i \quad (\text{A.15})$$

$$\mathbf{a} : \mathbf{b} = a_{ij} \mathbf{e}_i \mathbf{e}_j : b_{kl} \mathbf{e}_k \mathbf{e}_l = a_{ij} b_{kl} \underbrace{(\mathbf{e}_j \cdot \mathbf{e}_k)}_{\delta_{jk}} \underbrace{(\mathbf{e}_i \cdot \mathbf{e}_l)}_{\delta_{il}} = a_{ij} b_{ji} = \text{tr}(\mathbf{a} \cdot \mathbf{b}) \quad (\text{A.16})$$

multiplying from the inside out. Note that $\mathbf{S} : \mathbf{b} = \mathbf{S} : \mathbf{b}^\top = \mathbf{S}^\top : \mathbf{b}$ if \mathbf{S} is symmetric. For example the double dot product of a second order tensor with a third order tensor is:

$$a_{ij} : b_{klm} = a_{ij} b_{jim} = c_m \quad (\text{A.17})$$

Bibliography

- [1] A. Einstein. “Eine neue Bestimmung der Moleküldimensionen”. In: *Annalen der Physik* 324.2 (1906), pp. 289–306. DOI: 10.1002/andp.19063240204.
- [2] A. Einstein. “Berichtigung zu meiner Arbeit: „Eine neue Bestimmung der Moleküldimensionen””. In: *Annalen der Physik* 339.3 (1911), pp. 591–592. DOI: 10.1002/andp.19113390313.
- [3] O. Gold. “Beiträge zur Hydrodynamik der zähen Flüssigkeiten”. PhD thesis. Universität Wien, 1936.
- [4] E. Guth and R. Simha. “Untersuchungen über die Viskosität von Suspensionen und Lösungen. 3. Über die Viskosität von Kugelsuspensionen”. In: *Colloid & Polymer Science* 74.3 (1936), pp. 266–275. DOI: 10.1007/BF01428643.
- [5] G. K. Batchelor and J. T. Green. “The determination of the bulk stress in a suspension of spherical particles to order c^2 ”. In: *Journal of Fluid Mechanics* 56.03 (1972), pp. 401–427. DOI: 10.1017/S0022112072002435.
- [6] G. K. Batchelor. “The effect of Brownian motion on the bulk stress in a suspension of spherical particles”. In: *Journal of Fluid Mechanics* 83.01 (1977), pp. 97–117. DOI: 10.1017/S0022112077001062.
- [7] H. Eilers. “Die Viskosität von Emulsionen hochviskoser Stoffe als Funktion der Konzentration”. In: *Kolloid-Zeitschrift* 97.3 (1941), pp. 313–321. DOI: 10.1007/BF01503023.
- [8] S. H. Maron and P. E. Pierce. “Application of Ree-Eyring generalized flow theory to suspensions of spherical particles”. In: *Journal of Colloid Science* 11.1 (1956), pp. 80–95. DOI: 10.1016/0095-8522(56)90023-X.
- [9] I. M. Krieger and T. J. Dougherty. “A Mechanism for Non-Newtonian Flow in Suspensions of Rigid Spheres”. In: *Transactions of The Society of Rheology* 3.1 (1959), pp. 137–152. DOI: 10.1122/1.548848.

Bibliography

- [10] G. B. Jeffery. “The Motion of Ellipsoidal Particles Immersed in a Viscous Fluid”. In: *Proceedings of the Royal Society A: Mathematical, Physical and Engineering Sciences* 102.715 (1922), pp. 161–179. DOI: 10.1098/rspa.1922.0078.
- [11] G. L. Hand. “A theory of dilute suspensions”. In: *Archive for Rational Mechanics and Analysis* 7.1 (1961), pp. 81–86. DOI: 10.1007/BF00250752.
- [12] H. Brenner. “Suspension rheology in the presence of rotary Brownian motion and external couples: elongational flow of dilute suspensions”. In: *Chemical Engineering Science* 27.5 (1972), pp. 1069–1107. DOI: 10.1016/0009-2509(72)80021-6.
- [13] E. J. Hinch and L. G. Leal. “The effect of Brownian motion on the rheological properties of a suspension of non-spherical particles”. In: *Journal of Fluid Mechanics* 52.04 (1972), p. 683. DOI: 10.1017/S002211207200271X.
- [14] G. Lipscomb, M. Denn, D. Hur, and D. Boger. “The flow of fiber suspensions in complex geometries”. In: *Journal of Non-Newtonian Fluid Mechanics* 26.3 (1988), pp. 297–325. DOI: 10.1016/0377-0257(88)80023-5.
- [15] L. D. Landau and E. M. Lifshitz. *Fluid Mechanics*. 2nd ed. Vol. 6. Course of Theoretical Physics. Pergamon Press, 1987. ISBN: 978-0-08-033933-7.
- [16] Batchelor, G. K. *An Introduction to Fluid Dynamics*. Cambridge Mathematical Library. Cambridge University Press, 1985. ISBN: 9780521663960.
- [17] J. Happel and H. Brenner. *Low Reynolds number hydrodynamics*. Kluwer, 1983. ISBN: 90-247-2877-0.
- [18] M. A. Lauffer. “Motion in viscous liquids: Simplified derivations of the Stokes and Einstein equations”. In: *Journal of Chemical Education* 58.3 (1981), pp. 250–256. DOI: 10.1021/ed058p250.
- [19] B. M. Haines and A. L. Mazzucato. “A Proof of Einstein’s Effective Viscosity for a Dilute Suspension of Spheres”. en. In: *SIAM Journal on Mathematical Analysis* 44.3 (2012), pp. 2120–2145. DOI: 10.1137/100810319.
- [20] H. Ammari, P. Garapon, H. Kang, and H. Lee. “Effective viscosity properties of dilute suspensions of arbitrarily shaped particles”. In: *Asymptotic Analysis* 80.3-4 (2012), pp. 189–211. DOI: 10.3233/ASY-2012-1101.
- [21] J. R. Bautista-Quijano, F. Avilés, J. O. Aguilera, and A. Tapia. “Strain sensing capabilities of a piezoresistive MWCNT-polysulfone film”. In: *Sensors and Actuators, A: Physical* 159.2 (2010), pp. 135–140. DOI: 10.1016/j.sna.2010.03.005.

- [22] J. R. Bautista-Quijano, P. Pötschke, H. Brüning, and G. Heinrich. “Strain sensing, electrical and mechanical properties of polycarbonate/multiwall carbon nanotube monofilament fibers fabricated by melt spinning”. In: *Polymer (United Kingdom)* 82 (2016), pp. 181–189. DOI: 10.1016/j.polymer.2015.11.030.
- [23] E. S. Bhagavatheswaran et al. “Construction of an Interconnected Nanostructured Carbon Black Network: Development of Highly Stretchable and Robust Elastomeric Conductors”. In: *Journal of Physical Chemistry C* 119.37 (2015), pp. 21723–21731. DOI: 10.1021/acs.jpcc.5b06629.
- [24] D. Y. Borin, G. V. Stepanov, and S. Odenbach. “Tuning the tensile modulus of magnetorheological elastomers with magnetically hard powder”. In: *Journal of Physics: Conference Series* 412.13th (2013), p. 012040. DOI: 10.1088/1742-6596/412/1/012040.
- [25] C. W. Karl, J. McIntyre, T. Alshuth, and M. Klüppel. “Magneto-rheological elastomers with switchable mechanical properties”. In: *KGK Kautschuk Gummi Kunststoffe* 66.1-2 (2013), pp. 46–53.
- [26] C. Hintze et al. “Soft magnetic Elastomers with controllable Stiffness: Experiments and Modelling”. In: *Kautschuk Gummi Kunststoffe* 67.4 (2014), pp. 53–59.
- [27] F. R. Costa, M. Saphiannikova, U. Wagenknecht, and G. Heinrich. “Layered Double Hydroxide Based Polymer Nanocomposites”. In: *Wax Crystal Control · Nanocomposites · Stimuli-Responsive Polymers*. Advances in Polymer Science October 2007. Springer, 2007, pp. 101–168. DOI: 10.1007/12_2007_123.
- [28] T. A. Osswald and N. Rudolph. *Polymer Rheology*. 1st ed. Hanser Publishers, 2015. ISBN: 978-1-56990-523-4. DOI: 10.3139/9781569905234.
- [29] D. J. Highgate and R. W. Whorlow. “Rheological properties of suspensions of spheres in non-Newtonian media”. In: *Rheologica Acta* 9.4 (1970), pp. 569–576. DOI: 10.1007/BF01985469.
- [30] L. Nicodemo and L. Nicolais. “Viscosity of bead suspensions in polymeric solutions”. In: *Journal of Applied Polymer Science* 18.9 (1974), pp. 2809–2818. DOI: 10.1007/BF01333774.
- [31] A. J. Poslinski, M. E. Ryan, R. K. Gupta, S. G. Seshadri, and F. J. Frechette. “Rheological Behavior of Filled Polymeric Systems I. Yield Stress and Shear-Thinning Effects”. In: *Journal of Rheology* 32.7 (1988), p. 703. DOI: 10.1122/1.549987.

Bibliography

- [32] B. Lee and M. Mear. “Effect of inclusion shape on the stiffness of nonlinear two-phase composites”. In: *Journal of the Mechanics and Physics of Solids* 39.5 (1991), pp. 627–649. DOI: 10.1016/0022-5096(91)90044-0.
- [33] J. Laven and H. N. Stein. “The Einstein coefficient of suspensions in generalized Newtonian liquids”. In: *Journal of Rheology* 35.8 (1991), p. 1523. DOI: 10.1122/1.550245.
- [34] X. Chateau, G. Ovarlez, and K. L. Trung. “Homogenization approach to the behavior of suspensions of noncolloidal particles in yield stress fluids”. In: *Journal of Rheology* 52.2 (2008), p. 489. DOI: 10.1122/1.2838254.
- [35] R. I. Tanner, F. Qi, and K. D. Housiadas. “A differential approach to suspensions with power-law matrices”. In: *Journal of Non-Newtonian Fluid Mechanics* 165.23-24 (2010), pp. 1677–1681. DOI: 10.1016/j.jnnfm.2010.09.005.
- [36] A. G. Gibson and S. Toll. “Mechanics of the squeeze flow of planar fibre suspensions”. In: *Journal of Non-Newtonian Fluid Mechanics* 82.1 (1999), pp. 1–24. DOI: 10.1016/S0377-0257(98)00127-X.
- [37] B. Souloumiac and M. Vincent. “Steady shear viscosity of short fibre suspensions in thermoplastics”. In: *Rheologica Acta* 37.3 (1998), pp. 289–298. DOI: 10.1007/s003970050116.
- [38] G. D’Avino et al. “Rotation of a sphere in a viscoelastic liquid subjected to shear flow. Part I: Simulation results”. In: *Journal of Rheology* 52.6 (2008), p. 1331. DOI: 10.1122/1.2998219.
- [39] Y. J. Choi and M. A. Hulsen. “Alignment of particles in a confined shear flow of a viscoelastic fluid”. In: *Journal of Non-Newtonian Fluid Mechanics* 175-176.0 (2012), pp. 89–103. DOI: 10.1016/j.jnnfm.2012.02.003.
- [40] G. D’Avino, M. A. Hulsen, F. Greco, and P. L. Maffettone. “Bistability and metastability scenario in the dynamics of an ellipsoidal particle in a sheared viscoelastic fluid”. In: *Physical Review E* 89.4 (2014), p. 043006. DOI: 10.1103/PhysRevE.89.043006.
- [41] M. Trofa et al. “Numerical simulations of the competition between the effects of inertia and viscoelasticity on particle migration in Poiseuille flow”. In: *Computers & Fluids* 107 (2015), pp. 214–223. DOI: 10.1016/j.compfluid.2014.11.015.
- [42] G. D’Avino. “Computational rheology of solid suspensions”. PhD Thesis. University of Naples Federico II, 2009.

- [43] O. Harlen, M. Walkley, and S. Yoon. “Two particle interactions in a confined viscoelastic fluid under shear”. In: *Journal of Non-Newtonian Fluid Mechanics* 185-186 (2012), pp. 39–48. DOI: 10.1016/j.jnnfm.2012.07.003.
- [44] G. D’Avino, F. Greco, M. A. Hulsen, and P. L. Maffettone. “Rheology of viscoelastic suspensions of spheres under small and large amplitude oscillatory shear by numerical simulations”. In: *Journal of Rheology* 57.3 (2013), p. 813. DOI: 10.1122/1.4798626.
- [45] M. Kamal and A. Mutel. “Rheological Properties of Suspensions in Newtonian and Non-Newtonian Fluids”. In: *Journal of Polymer Engineering* 5.4 (1985), pp. 293–382. DOI: 10.1515/POLYENG.1985.5.4.293.
- [46] A. B. Metzner. “Rheology of Suspensions in Polymeric Liquids”. In: *Journal of Rheology* 29.6 (1985), p. 739. DOI: 10.1122/1.549808.
- [47] A. Y. Malkin. “Rheology of filled polymers”. In: *Advances in Polymer Science*. Vol. 96. 1990, pp. 69–97. DOI: 10.1007/3-540-52791-5_2.
- [48] H. A. Barnes. “A Review Of The Rheology Of Filled Viscoelastic Systems”. In: *Rheology Reviews* (2003), pp. 1–36.
- [49] Y. Wang, J. Xu, E. Bechtel, and K. K.W. “Melt shear rheology of carbon nanofiber/polyestylene composites”. In: *Rheologica Acta* 45 (2006), pp. 919–941. DOI: 10.1007/s00397-005-0077-8.
- [50] C. Kagarise, K. W. Koelling, Y. Wang, and S. E. Bechtel. “A unified model for polystyrene-nanorod and polystyrene-nanoplatelet melt composites”. In: *Rheologica Acta* 47.9 (2008), pp. 1061–1076. DOI: 10.1007/s00397-008-0307-y.
- [51] R. G. Larson. *The Structure and Rheology of Complex Fluids*. Oxford University Press, 1999, p. 688. ISBN: 978-0195121971.
- [52] C. W. Macosko. *Rheology - Principles, Measurements and Applications*. 1st ed. John Wiley & Sons, 1994. ISBN: 978-0471185758.
- [53] L. Mullins and N. R. Tobin. “Stress softening in rubber vulcanizates. Part I. Use of a strain amplification factor to describe the elastic behavior of filler-reinforced vulcanized rubber”. In: *Journal of Applied Polymer Science* 9.9 (1965), pp. 2993–3009. DOI: 10.1002/app.1965.070090906.
- [54] J. Domurath, M. Saphiannikova, and G. Heinrich. “The concept of hydrodynamic amplification in filled elastomers”. In: *KGK Kautschuk Gummi Kunststoffe* 70.1–2 (2017), pp. 40–43.

Bibliography

- [55] H.-S. Chen and A. Acrivos. “The effective elastic moduli of composite materials containing spherical inclusions at non-dilute concentrations”. In: *International Journal of Solids and Structures* 14.5 (1978), pp. 349–364. DOI: 10.1016/0020-7683(78)90017-3.
- [56] H. M. Laun. “Rheological properties of aqueous polymer dispersions”. In: *Macromolecular Materials and Engineering* 123.1 (1984), pp. 335–359. DOI: 10.1002/apmc.1984.051230115.
- [57] J. Mewis and N. J. Wagner. *Colloidal Suspension Rheology*. Cambridge Series in Chemical Engineering. Cambridge University Press, 2012. ISBN: 9780521515993.
- [58] R. B. Bird, R. C. Armstrong, and O. Hassager. *Dynamics of Polymeric Liquids, Fluid Mechanics*. 2nd ed. Vol. 1. John Wiley & Sons, 1987, p. 672. ISBN: 978-0-471-80245-7.
- [59] P. J. Carreau, D. Kee, and R. Chhabra. *Rheology of Polymeric Systems: Principles and Applications*. New York: Hanser Gardner, 1997. ISBN: 9781569902189.
- [60] R. H. Colby, D. C. Boris, W. E. Krause, and S. Dou. “Shear thinning of unentangled flexible polymer liquids”. In: *Rheologica Acta* 46.5 (2006), pp. 569–575. DOI: 10.1007/s00397-006-0142-y.
- [61] J. Domurath, M. Saphiannikova, G. Ausias, and G. Heinrich. “Modelling of stress and strain amplification effects in filled polymer melts”. In: *Journal of Non-Newtonian Fluid Mechanics* 171-172.0 (2012), pp. 8–16. DOI: 10.1016/j.jnnfm.2012.01.001.
- [62] P. Suquet. “Effective properties of nonlinear composites”. In: *Continuum Micromechanics*. Ed. by P. Suquet. CISM International Centre for Mechanical Sciences. Springer, 1997, pp. 187–264. ISBN: 9783211829028.
- [63] M. Schikowsky. “Theoretische Untersuchungen zum Spannungs-Dehnungs-Verhalten rüßgefüllter Netzwerke”. PhD thesis. Technische Hochschule Leuna-Merseburg, 1988.
- [64] S. Kim and S. J. Karrila. *Microhydrodynamics: Principles and Selected Applications*. 1st ed. Butterworth-Heinemann, 1991. ISBN: 9780750691734.
- [65] J. L. Ericksen. “Transversely isotropic fluids”. In: *Kolloid-Zeitschrift* 173.2 (1960), pp. 117–122. DOI: 10.1007/BF01502416.
- [66] H. Giesekus. “Elasto-viskose Flüssigkeiten, für die in stationären Schichtströmungen sämtliche Normalspannungskomponenten verschieden groß sind”. In: *Rheologica Acta* 2.1 (1962), pp. 50–62. DOI: 10.1007/BF01972555.

- [67] E. J. Hinch and L. G. Leal. “Time-dependent shear flows of a suspension of particles with weak Brownian rotations”. In: *Journal of Fluid Mechanics* 57.04 (1973), p. 753. DOI: 10.1017/S0022112073001990.
- [68] C. Binetruy, F. Chinesta, and R. Keunings. *Flows in Polymers, Reinforced Polymers and Composites*. 2015. ISBN: 978-3-319-16756-5. DOI: 10.1007/978-3-319-16757-2.
- [69] G. K. Batchelor. “Slender-body theory for particles of arbitrary cross-section in Stokes flow”. In: *Journal of Fluid Mechanics* 44.03 (1970), pp. 419–440. DOI: 10.1017/S002211207000191X.
- [70] G. K. Batchelor. “The stress generated in a non-dilute suspension of elongated particles by pure straining motion”. In: *Journal of Fluid Mechanics* 46.04 (1971), p. 813. DOI: 10.1017/S0022112071000879.
- [71] G. Ausias. “Une rhéologie des suspensions : Applications aux composites à matrices thermoplastiques”. Habilitation. Université de Bretagne-Sud, 2007.
- [72] J. Férec. “Nonlinear rheology of non-spherical particle suspensions”. Habilitation. Université de Bretagne-Sud, 2016.
- [73] J. Thomasset, P. J. Carreau, B. Sanschagrín, and G. Ausias. “Rheological properties of long glass fiber filled polypropylene”. In: *Journal of Non-Newtonian Fluid Mechanics* 125.1 (2005), pp. 25–34. DOI: 10.1016/j.jnnfm.2004.09.004.
- [74] J. Férec et al. “Investigation of the rheological properties of short glass fiber-filled polypropylene in extensional flow”. In: *Rheologica Acta* 48 (2009), pp. 59–72. DOI: 10.1007/s00397-008-0309-9.
- [75] C. Geuzaine and J. F. Remacle. “Gmsh: A 3-D finite element mesh generator with built-in pre- and post-processing facilities”. In: *International Journal for Numerical Methods in Engineering* 79.11 (2009), pp. 1309–1331. DOI: 10.1002/nme.2579.
- [76] G. Astarita. “Scale-up problems arising with non-Newtonian fluids”. In: *Journal of Non-Newtonian Fluid Mechanics* 4.4 (1979), pp. 285–298. DOI: 10.1016/0377-0257(79)80001-4.
- [77] M. J. Crochet, A. R. Davies, and K. Walters. *Numerical Simulation of Non-Newtonian Flow*. 1st ed. Elsevier, 1984. ISBN: 0-444-42291-9.
- [78] A. B. Metzner and J. C. Reed. “Flow of non-newtonian fluids—correlation of the laminar, transition, and turbulent-flow regions”. In: *AIChE Journal* 1.4 (1955), pp. 434–440. DOI: 10.1002/aic.690010409.

Bibliography

- [79] K. Madlener, B. Frey, and H. K. Ciezki. “Generalized reynolds number for non-newtonian fluids”. In: *Progress in Propulsion Physics*. Vol. 1. EDP Sciences, 2009, pp. 237–250. ISBN: 978-2-7598-0411-5. DOI: 10.1051/eucass/200901237.
- [80] I. T. Dosunmu and S. N. Shah. “Pressure drop predictions for laminar pipe flow of carreau and modified power law fluids”. In: *Canadian Journal of Chemical Engineering* 93.5 (2015), pp. 929–934. DOI: 10.1002/cjce.22170.
- [81] R. P. Chhabra. “Motion of spheres in power law (viscoelastic) fluids at intermediate Reynolds numbers: a unified approach”. In: *Chemical Engineering and Processing* 28.2 (1990), pp. 89–94. DOI: 10.1016/0255-2701(90)80004-0.
- [82] D. I. Graham and T. E. R. Jones. “Settling and Transport of Spherical-Particles in Power-Law Fluids At Finite Reynolds-Number”. In: *Journal of NonNewtonian Fluid Mechanics* 54 (1994), pp. 465–488. DOI: 10.1016/0377-0257(94)80037-5.
- [83] N. Kishore and R. R. Ramteke. “Slip in flows of power-law liquids past smooth spherical particles”. In: *Acta Mechanica* 226.8 (2015), pp. 2555–2571. DOI: 10.1007/s00707-015-1328-0.
- [84] C.-J. Lin, J. H. Peery, and W. R. Schowalter. “Simple shear flow round a rigid sphere: inertial effects and suspension rheology”. In: *Journal of Fluid Mechanics* 44.1 (1970), pp. 1–17. DOI: 10.1017/S0022112070001659.
- [85] C. Großmann and H. G. Roos. *Numerische Behandlung partieller Differentialgleichungen*. Teubner Studienbücher Mathematik. Vieweg+Teubner Verlag, 2005. ISBN: 9783519220893.
- [86] M. Larson and F. Bengzon. *The finite element method: theory, implementation, and applications*. 1st ed. Vol. 10. Texts in Computational Science and Engineering. Springer Verlag, 2013. ISBN: 978-3-642-33286-9.
- [87] D. Boffi, F. Brezzi, and M. Fortin. *Mixed Finite Element Methods and Applications*. Vol. 44. Springer Series in Computational Mathematics. Berlin, Heidelberg: Springer Berlin Heidelberg, 2013. ISBN: 978-3-642-36518-8. DOI: 10.1007/978-3-642-36519-5.
- [88] A. Logg and G. N. Wells. “DOLFIN: Automated Finite Element Computing”. In: *ACM Transactions on Mathematical Software* 37.2 (2010), pp. 1–28. DOI: 10.1145/1731022.1731030.

- [89] A. Logg, K.-A. Mardal, and G. Wells, eds. *Automated Solution of Differential Equations by the Finite Element Method*. 1st ed. Vol. 84. Lecture Notes in Computational Science and Engineering. Berlin, Heidelberg: Springer Berlin Heidelberg, 2012. ISBN: 978-3-642-23098-1. DOI: 10.1007/978-3-642-23099-8.
- [90] M. S. Alnæs et al. “The FEniCS Project Version 1.5”. In: *Archive of Numerical Software* 3.100 (2015), pp. 9–23. DOI: 10.11588/ans.2015.100.20553.
- [91] *FEniCS Web page*. 2016. URL: <http://fenicsproject.org/>.
- [92] P. R. Amestoy, I. S. Duff, J.-Y. L’Excellent, and J. Koster. “A Fully Asynchronous Multifrontal Solver Using Distributed Dynamic Scheduling”. In: *SIAM Journal on Matrix Analysis and Applications* 23.1 (2001), pp. 15–41. DOI: 10.1137/S0895479899358194.
- [93] *MUMPS Web page*. 2016. URL: <http://mumps.enseeiht.fr/>.
- [94] S. Balay, W. D. Gropp, L. C. McInnes, and B. F. Smith. “Efficient Management of Parallelism in Object Oriented Numerical Software Libraries”. In: *Modern Software Tools in Scientific Computing*. Ed. by E. Arge, A. M. Bruaset, and H. P. Langtangen. Birkhäuser Press, 1997, pp. 163–202.
- [95] S. Balay et al. *PETSc Users Manual*. Tech. rep. ANL-95/11 - Revision 3.6. Argonne National Laboratory, 2015.
- [96] S. Balay et al. *PETSc Web page*. 2016. URL: <http://www.mcs.anl.gov/petsc>.
- [97] H. H. Hu, N. Patankar, and M. Zhu. “Direct Numerical Simulations of Fluid–Solid Systems Using the Arbitrary Lagrangian–Eulerian Technique”. In: *Journal of Computational Physics* 169.2 (2001), pp. 427–462. DOI: 10.1006/jcph.2000.6592.
- [98] G. K. Batchelor. “The stress system in a suspension of force-free particles”. In: *Journal of Fluid Mechanics* 41.03 (1970), pp. 545–570. DOI: 10.1017/S0022112070000745.
- [99] R. Hill. “Elastic properties of reinforced solids: Some theoretical principles”. In: *Journal of the Mechanics and Physics of Solids* 11.5 (1963), pp. 357–372. DOI: 10.1016/0022-5096(63)90036-X.
- [100] Z. Hashin. “Theory of Mechanical Behavior of Heterogeneous Media”. In: *Applied Mechanics Reviews* 17.1 (1964), pp. 1–9.
- [101] S. Torquato. *Random Heterogeneous Materials: Microstructure and Macroscopic Properties*. Springer, 2002. ISBN: 9780387951676.

Bibliography

- [102] G. Milton. *The Theory of Composites*. 1st ed. Vol. 6. Cambridge monographs on applied and computational mathematics. Cambridge University Press, 2002. ISBN: 0-521-78125-6.
- [103] T. Zohdi and P. Wriggers. *An Introduction to Computational Micromechanics*. Lecture Notes in Applied and Computational Mechanics. Springer, 2008. ISBN: 9783540774822.
- [104] M. H. Wagner. “Zur Netzwerktheorie von Polymer-Schmelzen”. In: *Rheologica Acta* 18 (1 1979), pp. 33–50. DOI: 10.1007/BF01515686.
- [105] P. P. Castañeda. “The effective mechanical properties of nonlinear isotropic composites”. In: *Journal of the Mechanics and Physics of Solids* 39.1 (1991), pp. 45–71. DOI: 10.1016/0022-5096(91)90030-R.
- [106] M. Doi and S. F. Edwards. “Dynamics of concentrated polymer systems. Part 2.-Molecular motion under flow”. In: *Journal of the Chemical Society, Faraday Transactions 2: Molecular and Chemical Physics* 74 (1978), pp. 1802–1817. DOI: 10.1039/F29787401802.
- [107] M. E. Gurtin, E. Fried, and L. Anand. *The Mechanics and Thermodynamics of Continua*. 1st ed. Cambridge University Press, 2010. ISBN: 978-0-511-76980-1.

List of Symbols

Latin Symbols

$\mathbf{1}$	unit tensor
a_d	strain amplification factor
a_s	stress amplification factor
\mathbf{a}_2	second order orientation tensor
\mathbf{a}_4	fourth order orientation tensor
a, b, c	semi-principal axes of ellipsoid
A, B, C	rhological coefficients in TIF equation
d	diameter
d_0	applied rate of deformation
d_s	spatial dimension
\mathbf{d}	rate of strain tensor
D	diffusion coefficient
D_r	rotatory diffusivity
$H^1(\Omega)$	Hilbert space
I_p	moment of inertia tensor of a particle
k_B	Boltzmann's constant
K	flow consistency index
K_E^L	Einstein coefficient of Laven and Stein [33]
l	length (of a rod)
L	edge length of RVE cube
L_c	characteristic length
$L^2(\Omega)$	space of square integrable functions
m_p	mass of a particle
n	flow index or (shear) thinning exponent
\mathbf{n}	normal vector
N_a	number of elements along arc
p	pressure
\tilde{p}	test function for pressure
\mathbf{p}	orientation vector

List of Symbols

$\dot{\boldsymbol{p}}$	time derivative of orientation vector \boldsymbol{p}
P	power density
Pe	Peclet number
r	radius
r_a	aspect ratio
Re	Reynolds number
\mathcal{R}	space of real numbers
t	time
T	absolute temperature
\boldsymbol{u}	(fluid) velocity field
$\tilde{\boldsymbol{u}}$	test function for (fluid) velocity field
U	characteristic velocity
\boldsymbol{v}_p	translatory velocity of a particle
$\tilde{\boldsymbol{v}}_p$	test function for translatory velocity of a particle
V	volume
\boldsymbol{w}	vorticity tensor
$\boldsymbol{x} = (x, y, z)^\top = (x_1, x_2, x_3)^\top$	spatial coordinates
X	hydrodynamic amplification factor ($= \eta_r$)
\boldsymbol{X}	center of mass position
Y	shift factor
Z	shift factor
$\mathcal{L}, \mathcal{M}, \mathcal{N}, \mathcal{P}, \mathcal{U}, \mathcal{V}, \mathcal{W}$	functions spaces

Greek Symbols

$\dot{\gamma}$	shear rate / scalar deformation rate
Γ	(part) of the boundary of a domain
$\dot{\epsilon}, \dot{\epsilon}_1, \dot{\epsilon}_2$	strain rates
η	viscosity
η_0	zero shear viscosity
η_r	relative viscosity ($= X$)
η_{sp}	specific viscosity
$[\eta]$	intrinsic viscosity
θ_p	rotation angle of a particle
λ	characteristic time
λ_p	Lagrange multiplier on particle surface
$\tilde{\lambda}_p$	test function for Lagrange multiplier on particle surface

ρ	density
σ	scalar (shear) stress
$\boldsymbol{\sigma}$	stress tensor, without pressure
τ_d, τ_s	relaxation times
$\boldsymbol{\tau}$	stress tensor, including pressure
φ	volume fraction
φ_{\max}	maximum volume fraction
$\boldsymbol{\omega}_p$	angular velocity of a particle
$\tilde{\boldsymbol{\omega}}_p$	test function for angular velocity of a particle
Ω	domain
$\partial\Omega$	boundary of domain Ω

Subscripts

0	applied/macroscale value, except η_0
∞	value in the power law regime
m	matrix
p	particle
RVE	Representative Volume Element (RVE)

Superscripts

(hom)	value of homogeneous equivalent medium
(TIF)	value for transversely isotropic fluid equation (2.50)

Conventions

x	scalar
\mathbf{x}	vector
\mathbf{x}	2nd order tensor, in symbolic notation
$\langle \bullet \rangle$	spatial average of \bullet
$f(\bullet)$	“is a function of” \bullet
\bullet^T	transpose of \bullet
$\text{tr}(\bullet)$	trace of \bullet
$\text{div}(\bullet)$	divergence of \bullet
$\text{grad}(\bullet)$	gradient of \bullet
$\text{curl}(\bullet)$	curl of \bullet

List of Symbols

Abbreviations

ABS	Acrylonitrile butadiene styrene
DFG	Deutsche Forschungsgemeinschaft
FEM	Finite-Element-Method
LDPE	Low-density polyethylene
PA6	Polyamide 6
PC	Polycarbonate
RVE	Representative Volume Element
SSAA	stress and strain amplification approach
TIF	Transversely Isotropic Fluid

List of Figures

1.1.	Relative change in viscosity for a LDPE melt filled with nano clay. . . .	2
1.2.	Flow curves for different polymers at different temperatures.	3
2.1.	Viscosity vs. shear stress for a suspension of polymer spheres in water, from Laun [56].	7
2.2.	Viscosity data of Poslinski et al. [31] for a thermoplastic melt filled with glass spheres.	11
2.3.	Sketch of the shift factors for a generalized Newtonian fluid.	15
2.4.	Contour plot of the function $g(\varphi, n)$ given by (2.42).	17
2.5.	Data of Poslinski et al. [31] shifted according to Barnes [48].	18
2.6.	Sketch of a spheroidal particle.	19
2.7.	Comparison of the rheological coefficient A	23
2.8.	Comparison of the rheological coefficient B	24
2.9.	Comparison of the rheological coefficient C	24
2.10.	Sketch of a rod in a simple shear flow.	26
2.11.	Viscosity as a function of stress, approximation (2.69) vs. exact inverse.	29
3.1.	Sketch of the computational domain.	32
3.2.	Example mesh for an oblate spheroid.	35
3.3.	Sketch of the boundaries for 1/8 of the RVE.	38
3.4.	Sketch of a fluid domain with one immersed particle.	40
3.5.	Sketch of the boundaries for 1/2 of the RVE.	43
3.6.	Schematic sketch of the comparison on power density in the suspension.	45
3.7.	Comparison of the intrinsic viscosity for a Newtonian fluid using the volume average and the stresslet.	46
3.8.	Normal vectors at a circle, 2d mesh.	47
3.9.	Example meshes for different values of N_a used to check the convergence of volume average and stresslet.	49
4.1.	Mesh used for the simulation for the particle with radius $r = 0.05$	52
4.2.	Dependence of η_{sp}/φ on the Carreau number and the particle radius.	53
4.3.	Dependence of $[\eta]$ on the Carreau number $\dot{\gamma}_0\lambda$ for different thinning exponents.	54
4.4.	Sketch of the different regions in the Carreau model (2.17) and their corresponding intrinsic viscosities after homogenization.	55

List of Figures

4.5.	Dependence of $[\eta]$ on the thinning exponent n at high values of the scalar deformation rate.	56
4.6.	Definition of relaxation time in the Carreau model, $\lambda = \dot{\gamma}_{\text{crit}}^{-1}$	59
4.7.	Dependence of the intrinsic viscosity on the Carreau number, simulation vs. model.	60
4.8.	Dependence of the relative critical deformation rate on the thinning exponent.	61
4.9.	Application of (4.18) to the data of Poslinski et al. [31].	64
5.1.	Sketches of the four selected configurations.	70
5.2.	Prolate particle mesh for elongation.	72
5.3.	Oblate particle mesh for shear	73
5.4.	Intrinsic viscosity for different particle volumes, prolate.	74
5.5.	Intrinsic viscosity for different particle volumes, oblate.	75
5.6.	Intrinsic viscosity as function of the particle aspect ratio for configuration (c1).	76
5.7.	Intrinsic viscosity as function of the particle aspect ratio for configuration (c2).	76
5.8.	Intrinsic viscosity as function of the particle aspect ratio for configuration (c3).	77
5.9.	Intrinsic viscosity as function of the particle aspect ratio for configuration (c5).	77
5.10.	Values for the rheological coefficient C_∞	78
5.11.	Values for the rheological coefficient B_∞	78
5.12.	Values for the rheological coefficient A_∞ for the configuration (c1).	79
5.13.	Values for the rheological coefficient A_∞ for the configuration (c2).	79
5.14.	Comparison of the coefficients $A_\infty^{(c1)}$ and $A_\infty^{(c2)}$	80
5.15.	Comparison of intrinsic viscosity in simple shear (c5) and in planar elongation (c3).	81
5.16.	Comparison of the z -component of the angular velocity of particles with different aspect ratios in a simple shear flow.	82
5.17.	Comparison of the numerical results for C_∞ with the model proposed in (5.14c), curves for $x_C = 1.8$	84
5.18.	Comparison of the numerical results for B_∞ with the model proposed in (5.14b), curves for $x_B = 1.8$	85
5.19.	Comparison of the numerical results for $A_\infty^{(c1)}$ with the model proposed in (5.14a), curves for $x_A^{(c1)} = 2.4$	85
5.20.	Comparison of the numerical results for $A_\infty^{(c2)}$ with the model proposed in (5.14a), curves for $x_A^{(c2)} = 1.8$	86
5.21.	Comparison of $[\eta]$ for spherical particles for the four different configurations.	87
5.22.	Comparison of the model for $[\eta]_\infty$ given by (4.10) with the results for the different configurations.	88

List of Tables

2.1. Shift factors extracted from the data of Poslinski et al. [31] by fitting to the Carreau model.	17
2.2. Rheological coefficients A , B and C for the TIF equation.	23
4.1. Radii and the corresponding computed volume fractions of the particles.	51
5.1. Unique configurations in uniaxial and planar elongation.	69
5.2. Unique configurations in simple shear.	69

Curriculum Vitæ

Personal Information

Name Jan Domurath
Date of birth 18 June 1985

Education

- 2005 BSZ e.o. plauen, *Plauen, Germany*.
Abitur
- 2005 – 2012 Technische Universität Dresden, *Dresden, Germany*.
studies of mechanical engineering
specializations: lightweight constructions and polymer technologies
degree: Diplom-Ingenieur (Dipl.-Ing.)
- since 2012 Technische Universität Dresden, *Dresden, Germany* and
Université de Bretagne-Sud, *Lorient, France*.
PhD-Student (Cotutelle de thèse)
- 2014 ECEMP International Graduate School
Technische Universität Dresden, *Dresden, Germany*.

List of Publications

Journal Papers

- [J1] M. Liebscher, J. Domurath, B. Krause, M. Saphiannikova, G. Heinrich, and P. Pötschke. “Electrical and melt rheological characterization of PC and co-continuous PC/SAN blends filled with CNTs: Relationship between melt mixing parameters, filler dispersion and filler aspect ratio”. In: *Journal of Polymer Science Part B: Polymer Physics* 56.1 (2018), pp. 79–88. DOI: 10.1002/polb.24515.
- [J2] J. Domurath, M. Saphiannikova, and G. Heinrich. “The concept of hydrodynamic amplification in filled elastomers”. In: *KGK Kautschuk Gummi Kunststoffe* 70.1–2 (2017), pp. 40–43.
- [J3] J. Domurath, M. Saphiannikova, J. Férec, G. Ausias, and G. Heinrich. “Stress and strain amplification in a dilute suspension of spherical particles based on a Bird-Carreau model”. In: *Journal of Non-Newtonian Fluid Mechanics* 221.0 (2015), pp. 95–102. DOI: 10.1016/j.jnnfm.2015.04.002.
- [J4] J. Domurath, M. Saphiannikova, and G. Heinrich. “Non-Linear Viscoelasticity of Filled Polymer Melts: Stress and Strain Amplification Approach”. In: *Macromolecular Symposia* 338.1 (2014), pp. 54–61. DOI: 10.1002/masy.201100118.
- [J5] J. Domurath, M. Saphiannikova, G. Ausias, and G. Heinrich. “Modelling of stress and strain amplification effects in filled polymer melts”. In: *Journal of Non-Newtonian Fluid Mechanics* 171-172.0 (2012), pp. 8–16. DOI: 10.1016/j.jnnfm.2012.01.001.

Proceedings

- [P1] K. Schneider, L. Zybell, J. Domurath, G. Heinrich, S. V. Roth, A. Rothkirch, and W. Ohm. “Investigation of time dependence of dissipation and strain induced crystallization in natural rubber under cyclic and impact loading”. In: *Constitutive Models for Rubber X: Proceedings of the European Conference on Constitutive Models for Rubbers X*. (Munich, Germany, Aug. 28–31, 2017). 2017, pp. 173–177. ISBN: 978-1-138-03001-5. DOI: 10.1201/97811315223278-30.
- [P2] L. Zybell, J. Domurath, and K. Schneider. “Thermomechanics of strain-induced crystallization in natural rubber under cyclic loading”. In: *PAMM* (submitted) (2017).

List of Publications

- [P3] J. Domurath. “Stress and strain amplification in a dilute suspension of spherical particles in a generalized Newtonian fluid”. In: *5th Workshop of the ECEMP International Graduate School*. Ed. by W. A. Hufenbach and M. Gude. Radebeul, Germany: Technische Universität Dresden, 2014, pp. 57–74.

Other publications

- [O1] J. Domurath, M. Saphiannikova, and G. Heinrich. “Understanding of reinforcement in polymer networks and melts”. In: *Kautschuk Gummi Kunststoffe* 67 (2014), p. 17.

Talks at international conferences

- [T1] J. Domurath, M. Saphiannikova, G. Ausias, J. Férec, and G. Heinrich. “Viscosity amplification in dilute suspensions of rods in a Carreau matrix fluid”. In: PPS Europe Africa Conference. (Dresden, Germany, June 26–29, 2017).
- [T2] J. Domurath, M. Saphiannikova, G. Ausias, J. Férec, and G. Heinrich. “Viscosity amplification in dilute suspensions of non-spherical particles in a Carreau matrix fluid”. In: Annual European Rheology Conference (AERC2017). (Copenhagen, Denmark, Apr. 3–6, 2017).
- [T3] L. Zybell, J. Domurath, and K. Schneider. “Thermomechanics of strain-induced crystallization in carbon black filled natural rubber under cyclic loading”. In: 88th Annual Meeting of the International Association of Applied Mathematics and Mechanics. (Weimar, Germany, Mar. 6–10, 2017).
- [T4] J. Domurath, M. Saphiannikova, J. Férec, G. Ausias, and G. Heinrich. “Viscosity Amplification In Dilute Suspensions Of Non-Spherical Particles In A Non-Newtonian Matrix Fluid”. In: 32nd International Conference of the Polymer Processing Society (PPS-32). (Lyon, France, July 25–29, 2016).
- [T5] J. Domurath, M. Saphiannikova, J. Férec, G. Ausias, and G. Heinrich. “Viscosity amplification in dilute suspensions of spherical particles with a non-Newtonian matrix fluid”. In: 49ème congrès annuel du Groupe Français de Rhéologie. (Grenoble, France, Sept. 27–29, 2014).
- [T6] J. Domurath and M. Saphiannikova. “Approaches to hydrodynamic reinforcement in polymer melts and networks”. In: 14th Dresden Polymer Discussion. (Meißen, Germany, May 25–28, 2014).
- [T7] S. Westermann, W. Pyckhout-Hintzen, J. Domurath, M. Meyer, M. Saphiannikova, G. Heinrich, and D. Richter. “Matrix chain deformation in reinforced networks - a SANS approach”. In: 14th Dresden Polymer Discussion. (Meißen, Germany, May 25–28, 2014).

- [T8] J. Domurath, M. Saphiannikova, J. Férec, G. Ausias, and G. Heinrich. “Viscosity amplification in dilute suspensions of spherical particles with a non-Newtonian matrix fluid”. In: 9th Annual European Rheology Conference (AERC2014). (Karlsruhe, Germany, Apr. 8–11, 2014).
- [T9] J. Domurath, M. Saphiannikova, T. Horst, and G. Heinrich. “Modelling of strain amplification effects in filled elastomers”. In: Rubber Reinforcement by Fillers, Fibres and Textiles. (London, United Kingdom, Dec. 18–19, 2012).
- [T10] J. Domurath, M. Saphiannikova, and G. Heinrich. “Modelling of stress and strain amplification effects in filled polymer melts”. In: 7th Annual European Rheology Conference. (Suzdal, Russia, May 10–14, 2011).
- [T11] J. Domurath, M. Saphiannikova, and G. Heinrich. “Modelling of stress and strain amplification effects in filled polymer melts”. In: DPG Spring Meeting. (Dresden, Germany, Mar. 13–18, 2011).
- [T12] J. Domurath, M. Saphiannikova, and G. Heinrich. “Viscosity amplification in dilute suspensions of non-spherical particles in a non-Newtonian matrix fluid”. In: 6th Annual European Rheology Conference. (Göteborg, Sweden, Apr. 7–9, 2010).

Other talks

- [OT1] J. Domurath. “Rheologische Beschreibung gefüllter Polymere”. In: Vorlesungsreihe „Werkstoffe der Zukunft“, Hof University of Applied Sciences. (Hof, Germany, Jan. 14, 2016).
- [OT2] J. Domurath. “Estimation of mechanical properties of suspensions with non-Newtonian matrices: analytical and numerical approaches”. In: Institute of Scientific Computing, TU Dresden. (Dresden, Germany, Aug. 13, 2015).

Poster

- [PO1] J. Domurath, M. Saphiannikova, G. Ausias, J. Férec, and G. Heinrich. “Viscosity amplification in dilute suspensions of non-spherical particles in a Carreau matrix fluid”. In: 2nd Berlin Dresden Prague Würzburg Workshop on “Mathematics of Continuum Mechanics”. (Dresden, Germany, Dec. 5, 2016).
- [PO2] J. Domurath, M. Saphiannikova, J. Férec, G. Ausias, and G. Heinrich. “Rheological behaviour of dilute suspensions of non-spherical particles in a non-Newtonian matrix fluid”. In: 10th Annual European Rheology Conference (AERC2015). (Nantes, France, Apr. 14–17, 2015).

List of Publications

- [PO3] J. Domurath, M. Saphiannikova, T. Horst, and G. Heinrich. “Strain amplification effects in filled elastomers”. In: 14th Dresden Polymer Discussion. (Meißen, Germany, May 25–28, 2014).
- [PO4] J. Domurath, M. Saphiannikova, and G. Heinrich. “Nonlinear viscoelasticity of filled polymer melts: Stress and strain amplification approach”. In: 9th EUROFILLERS International Conference. (Dresden, Germany, Aug. 21–25, 2011).
- [PO5] J. Domurath, M. Saphiannikova, and G. Heinrich. “Effects of strain and stress amplification in filled polymer melts”. In: DPG Spring Meeting. (Regensburg, Germany, Mar. 21–26, 2010).